Boiling Heat Transfer with Nanofluids
An Experimental Study

by

Chiara Lucia Tregnago

to obtain the degree of Master of Science in Energy, Flow and Process Technology
at the Delft University of Technology,
to be defended publicly on Friday September 30, 2022 at 14:00 hours.

Student number: 5393531
Project duration: December, 2021 – September, 2022
Thesis committee: Prof. Dr. Ir. R. Delfos,   TU Delft, supervisor
                              Prof. Dr. Ir. K. Hooman,   TU Delft
                              Prof. Dr. Ir. J.W.R. Peeters,   TU Delft
                              Prof. Dr. Ir. R. Pecnik,   TU Delft
                              Ir. S. Fateh,   Synano

An electronic version of this thesis is available at `http://repository.tudelft.nl/`.

Abstract

Recent advancements in the field of nanotechnology have proven to offer viable alternatives for energy production, transport and storage. As far as thermal energy is concerned, nanofluids have emerged as a novel method to enhance heat transfer. Indeed, nanofluids exhibit superior thermal capabilities, which may be able to meet the requirement of high heat dissipation rate in limited space advanced by various high-tech industries.

In particular, boiling heat transfer is an efficient heat removal mechanism that may be further improved by using nanofluids. Indeed, it has been reported that nanoparticles play a crucial role in affecting the parameters which have major impact on the boiling process (i.e. thermophysical properties of the fluid, heating surface morphology, near-surface hydrodynamics). Being boiling very sensitive to surface characteristics, the latter factors have been found to have a significant influence on the boiling heat transfer coefficient. Hence, the aim of the present research is to elucidate the physical mechanisms underlying pool boiling of nanofluids.

Based on this framework, a pool boiling test facility has been designed and validated, thus enabling to conduct a comparative study on boiling of a pure fluid (water) and a water-alumina $0.1 \% \, wt$ nanofluid. The pool boiling experiments were performed on six aluminium samples, which were characterized by SEM (scanning electron microscopy) and WLI (white light interferometry) before and after boiling in order to highlight the change in surface topography.

The research efforts were targeted at correlating the trend of the boiling curves and the surface parameters of the corresponding sample. Nonetheless, due to the limited dataset and the inconsistencies in the behaviour of the tested nanofluid, further investigation is required to assess the potential of nanofluids as more efficient heat transfer media.

Contents

List of Figures

List of Tables

Nomenclature

Acronyms

CHF   Critical Heat Flux

HTC   Heat Transfer Coefficient

ONB   Onset of Nucleate Boiling

Greek symbols

α	Thermal diffusivity	[m^2/s]
δ	Boundary layer thickness	[m]
λ	Wavelenght	[m]
μ	Dynamic viscosity	[Pa.s]
ν	Kinematic viscosity	[m$^2/s$]
ρ	Density	[kg/m^3]
ρ_l	Density of liquid phase	[kg/m^3]
ρ_v	Density of vapour phase	[kg/m^3]
σ	Surface Tension	[kg/s^2]
τ	Wall shear stress	[Pa]
θ	Contact angle	[°]

Roman symbols

ΔT	Wall superheat	[K]
$\dot{m}$	Mass flow rate	[kg/m^3]
D	Diameter	[m]
D_b	Bubble departure diameter	[m]
f_b	Bubble departure frequency	[1/s]
g	Acceleration due to gravity	[m/s^2]
h	Heat transfer coefficient	[W/(m^2 $°C$]
h_{fg}	Enthalpy of vaporization	[J/kg]
k	Thermal conductivity	[W/(m K)]
m	Mass	[kg]
P	Pressure	[Pa]
Q	Volume flow rate	[m$^3/s$]
q	Heat flux	[W/m^2]

r	Radius	[m]
r_c	Mouth radius of a surface cavity	[m]
t	Time	[s]
T_∞	Bulk temperature of fluid	[K]
T_w	Wall temperature	[K]
T_{sat}	Saturation temperature	[K]
V	Volume	[m^3]
v	Velocity	[m/s]
z	Axial distance	[m]

Acknowledgements

The two-years long journey at TU Delft has been an exceptional enriching experience, culminating with this thesis. During the past nine months, I have been questioning myself and the direction of my future choices, I have changed my attitude towards obstacles and challenges. I used to be scared of the unknown and the possibility of failure, now I have reached a new level of awareness, being able to see arduous times as opportunities. This would not have been possible without the unceasing support of all who have accompanied me throughout this growth path.

I would like to express my deep gratitude to my supervisor Dr. R. Delfos for having constantly encouraged me while dealing with the struggle of conducting an experimental project. I remember his words during one of our first meetings, which I consider as some of the most valuable lessons: "there is no too complex task" and "your time is the most precious resource". Under his guidance, I have been able to appreciate how small sequential steps lead to the solution of what seemed initially an intricate issue and I have experienced firsthand that engineering research requires inevitably trial and error. I am grateful to him for always being open to discussion, for fostering my reasoning and critical thinking.

I would like to thank the team at Synano for the wealth of knowledge and experience acquired over the duration of this graduation project. Not only I had the chance to prove myself working in the engineering field which mostly arouses my curiosity, I was also actively involved in the research activity of the company. The satisfaction of seeing how my contribution reflects into practical application is invaluable. There have been countless moments when I felt lost as the direction of my project was not predefined, but the urge of finding my own solution ultimately served to develop my independence. I am grateful to my colleagues who have assisted me in this strenuous process, for their patience and emotional support.

I want to extend my sincere thanks to the 3mE staff, in particular to Bart, Jasper, and Damian, whose technical skills and practical help were essential to implement my ideas and finally get the setup to work properly.

Moreover, I would like to acknowledge the help received from the technicians at the Kavli Nanolab and the Applied Science faculty: thank you Lodi and Sietse for your dedication while training me on new experimental techniques.

Infinite thanks to the unconditional love of my family and closest friends: I am humbled to have you by my side and I dedicate my achievements to you. Special thanks to my dad Sandro for being my constant source of inspiration and my mum Paola for believing in me even when I felt defeated and insecure. My heartfelt gratitude to both the international group in Delft and the loyal "squad" back in Vicenza. Thank you all for sharing with me joyful and stressful moments, what an emotional rollercoaster it has been!

1

Introduction

1.1. Background and Motivation

Energy efficiency is undoubtedly one of the most compelling challenges in the 21st century, due to the ever-growing energy demand and the limited availability of fossil fuel-derived energy sources. Indeed, the European Union 2030 climate and energy framework, which includes the key objectives for the period from 2021 to 2030, has set a target of 32.5% improvement in energy efficiency as a milestone for a sustainable growth and carbon-neutral economy by 2050 [18]. Although constant advancements in existing technologies will continue to be vital to the energy transition, implementation of revolutionary technology will play a major role. In such a context, nanotechnology has emerged in recent years as a groundbreaking field of science. Nanotechnology refers to the manipulation of matter at nano-scale (between 1 and 100 nm) to produce engineered materials, structures and devices. At this scale, the constituent particles of a certain material exhibit unique physical, mechanical and chemical properties, opening up unexplored possibilities of energy production, transport and storage [88].

As far as thermal energy is concerned, a novel method for improving heat transfer is the use of nanofluids. The term *nanofluid* was introduced in 1995 by Choi and Eastman [15] to define a new class of heat transfer media consisting of nano-sized particles (lenght scale 1-100 nm) suspended in a base fluid. These colloidal suspensions have been synthesised using various nanoparticles' materials and shapes, as illustrated in Figures 1.1, 1.2, 1.3. Therefore, nanofluids are classified based on the type of nanomaterial, ranging from pure metal (copper, iron, gold, silver), to metal oxide (alumina, copper oxide, silica, titania, zirconia), and non-metal (carbon nanotubes/nanowires, graphene sheets, diamond) [4]. As base fluids, water, ethylene or propilene gylocol, different oils and refrigerants are used. The presence of nanoparticles results in superior thermophysical properties, which find fruitful application to thermal management systems.

3
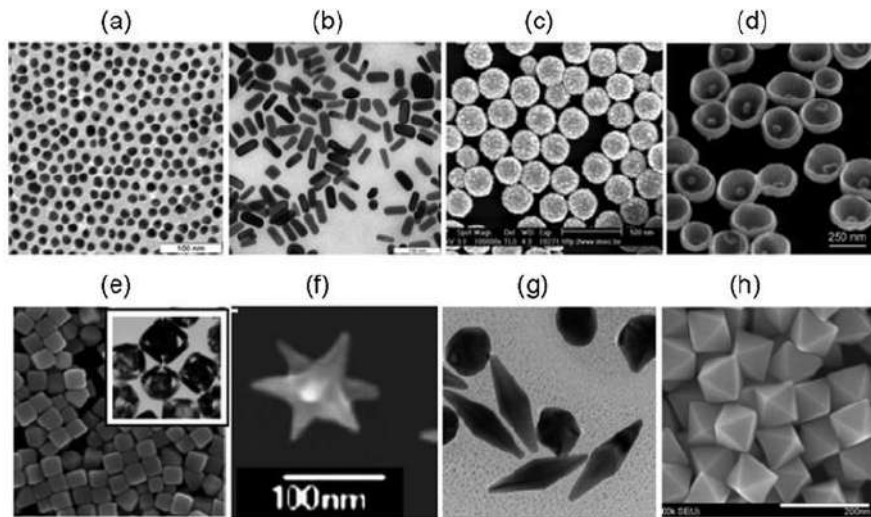
Figure 1.1: Different gold nanoparticles [55]
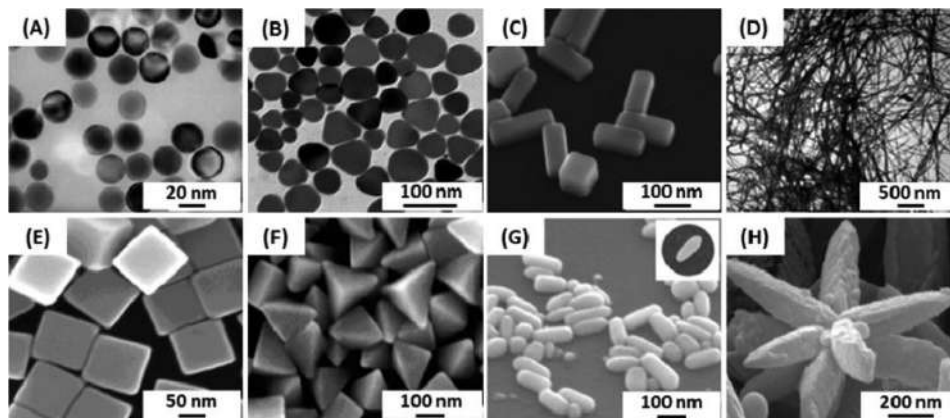
Figure 1.2: Different silver nanoparticles [79]

Synano is a start-up company established in 2017 within the YES!Delft incubator. So far, the company has been focusing on R&D activity, with the mission of developing *nanocoolants* to meet the demand of high thermal dissipation rate faced by various sectors (power electronics, data centres, refrigeration, electric transportation, aviation). Indeed, high-tech industries are experiencing a constant increase in power output accompanied by a strong trend for components' miniaturization. As a consequence, efficient cooling solutions are of primary importance to ensure optimal operating conditions along with safety and reliability.

Synano envisions itself as a provider of nanofluids with superior heat transfer capabilities and is participating in European consortia seeking for state-of-the-art technologies. In particular, Synano is currently a member of "BRAINE", within the scope of "ECSEL Research and Innovation Action (RIA)-Call 2019", and "ADENEAS", within the scope of "MG-2020-singleStage-INEA". In the former project, consortium members are working towards the ultimate goal of developing high-performing Edge microdata centers with embedded Artificial Intelligence. Synano's task is to provide purposely engineered nanofluids to improve the cooling efficiency in thermosyphons. This will enable microdata center to reach the target of 100 W/node [29]. The second project, Advanced Data and power Electrical NEtwork Architectures and Systems (ADENEAS), aims at the development of a power and data distribution network which is scalable to all aircraft sizes and the integration of this network with the cooling system. Indeed, the increased electrification in aviation implies higher heat dissipation requirements [28]. Therefore, Synano is contributing to this mission by synthesising nanofluids which are able to increase the critical heat flux in two-phase cooling systems. Indeed, in order to achieve high dissipation rates, heat exchangers make use of boiling heat transfer. This represents an excellent mechanism for heat removal as the

phase change process yields high heat fluxes, up to two orders of magnitude larger than liquid convection heat transfer. The efficiency characterizing the boiling mechanism derives from the liquid being able to convectively transport heat away from the heater surface, and utilize it in generating vapour that removes significant amount of heat from the liquid and provides a driving force for the localized liquid motion [107].
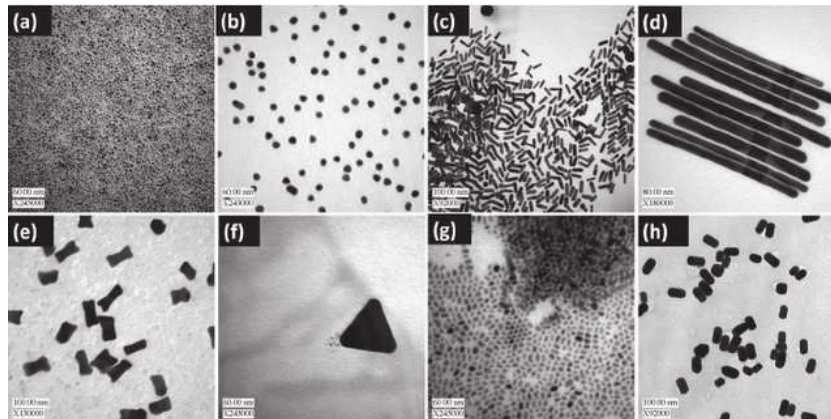
Figure 1.3: Various types and shapes of nanoparticles [33]

In view of the previous considerations, further research on the physical mechanisms underlying the enhancement in boiling heat transfer using nanofluids is of utmost interest, both from a fundamental and industrial perspective. Therefore, the present project aims at investigating experimentally the thermal performance of nanofluids with particular focus on their application to two-phase heat transfer systems.

1.2. Research questions

The ultimate goal of this project is to provide a critical assessment of the potential improvement in terms of energy efficiency that the use of nanofluids in cooling systems may lead to. Hence, a literature study has been conducted to address the following research questions and sub-questions:

- What are the physical mechanisms governing boiling heat transfer using nanofluids?

  - What are the relevant parameters affecting boiling heat transfer and how are they affected by the presence of nanoparticles?

  - How are the nanoparticles' characteristics mutually related?

- How does the thermal performance of nanofluids compare to that of pure fluids?

  - What is the change in heat transfer coefficient and critical heat flux?

  - What are the physical mechanisms underlying the improvement/degradation in the above mentioned parameters?

- What are the design requirements for a pool boiling setup which should enable a comprehensive experimental analysis?

  - What are the quantities of interest?

  - What are the additional measurements to be performed?

  - What are the requirements in terms of accuracy and repeatability?

1.3. Thesis objectives

On the basis of the literature study, the following thesis objectives have been identified:

1. Design and set up the pool boiling test facility.

2. Perform benchmark tests to validate the experimental apparatus.

3. Conduct comparative analysis on the behaviour of pure fluids and nanofluids under pool boiling conditions.

4. Evaluate the overall performance of nanofluids and draw conclusions on their potential applicability to two-phase cooling systems.

1.4. Layout of the thesis report

This thesis consists of six chapters. The outline of contents in each of them is listed below:

1. **Introduction:** A brief overview of the project background is given. The need for a more in-depth study on enhancement of pool boiling heat transfer is presented in the light of its implications on fundamental research and industrial applications.

2. **Boiling with pure fluids:** Core principles of boiling heat transfer, including governing physical mechanisms and the effect of system parameters, are introduced as theoretical framework for further analysis on the role of nanoparticles.

3. **Boiling with nanofluids:** Thermal properties and boiling heat transfer mechanism of nanofluids are reviewed, highlighting the advantages as well as critical issues associated to their application to pool boiling. The influence of nanoparticles on pool boiling is analysed from both a conceptual and practical perspective, with the support of theoretical models and available experimental data.

4. **Experimental work:** The research method to conduct the experimental analysis is described. From the requirements for the pool boiling test facility, the preliminary design of the setup to be used in the present project is illustrated.

5. **Results and analysis:** The results of the pool boiling experiments with water and the water-alumina $0.1 \% wt$ nanofluid are presented. In particular, the trend of the pool boiling curves and the surface characteristics are analysed. Finally, a correlation between the heat transfer coefficient and the roughness parameters is proposed.

6. **Conclusions and recommendations:** A summary of the main findings is given. Moreover, limitations of the present work and scope for future research are discussed.

2

Boiling with pure fluids

2.1. Fundamentals

Boiling is the heat transfer process that involves the phase change from liquid to vapour, hence vapour bubbles start forming at the heating surface and in the adjacent liquid layer. Boiling is further subdivided in two main categories based on the relative motion between the bulk fluid and the heating surface: pool boiling and flow boiling. Pool boiling is defined as the boiling of a stagnant liquid over a submerged heated surface. If the bulk fluid temperature is below the saturation temperature of the fluid, the process is called subcooled pool boiling, whereas if the liquid is at its boiling point the process is termed saturated pool boiling. Flow boiling occurs under forced flow conditions and it is distinguished between internal and external flow, respectively. The former indicates the boiling of a flowing stream over an unconfined surface, while in the latter case flow boiling takes place inside a channel.

2.2. The pool boiling curve

Pool boiling is characterized by different regimes as shown in Figure 2.1, which is the conventional representation of heat flux q versus wall superheat ΔT (difference between the temperature of the heating surface and the saturation temperature of the fluid at a given pressure) on a logarithmic scale. This plot, known as the boiling curve, resulted from the experimental work of previous researchers, namely Leidenfrost (1756), Lang (1888), McAdams (1941), Nukiyama (1934), Faber and Scorah (1948) [116]. The path followed by the boiling fluid through the different regimes depends on whether heat flux or surface temperature is the independent variable. Normally when boiling experiments are performed, the power of the heater is the controlled variable, therefore a more detailed description will be given for this case.
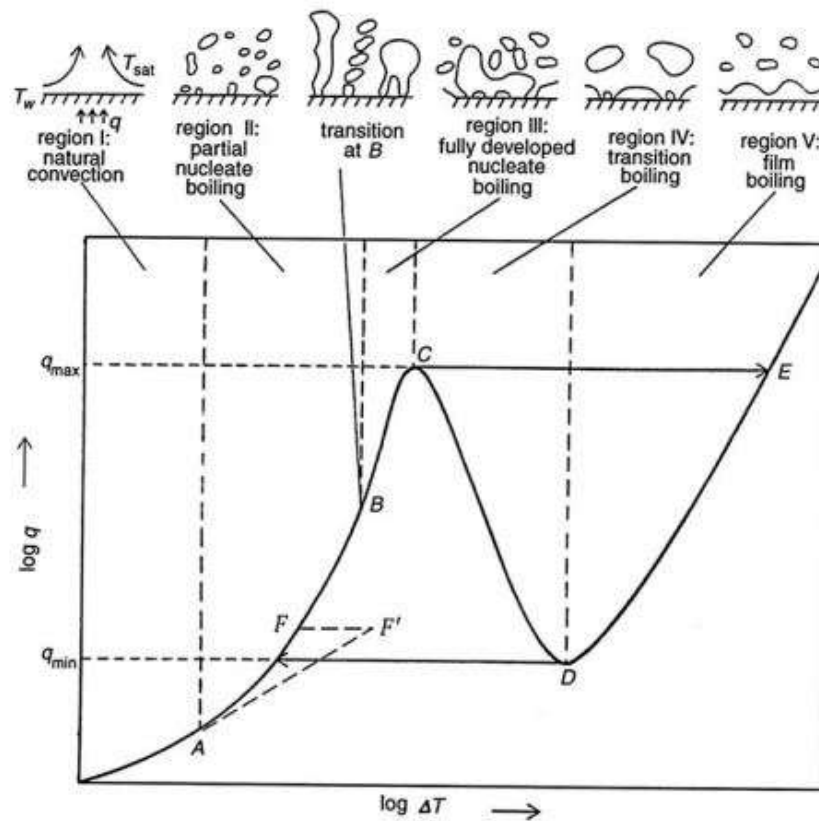
Figure 2.1: Pool boiling regimes [67]

Before reaching point A, when the heat input rate to the surface is gradually increased, the wall superheat is low enough that no bubbles nucleate on the surface and the liquid in proximity of the surface is locally heated creating a thermal boundary layer. These conditions are encountered in the region I of the boiling curve, where natural convection is the dominant mechanism of both fluid motion and heat transfer. Point A represents the onset of nucleate boiling (ONB), which is the beginning of bubbles' nucleation in correspondence of irregularities on the heating surface, such as cavities or scratches, which are defined as active nucleation sites. Surface defects act as preferential locations for the generation of bubbles for two reasons: the first one is that such cavities increase the contact area between the liquid and the heating surface thus facilitating the phase change of the trapped fluid; the second one is that surface cracks may contain preexisting gas nuclei so bubbles tend to form at these sites by heterogeneous nucleation [1].

After the onset of nucleate boiling, the slope of the curve increases significantly due to improved heat removal resulting from three mechanisms: bubble agitation, thermal boundary layer stripping, and evaporation [17]. First, the growth and detachment of bubbles from the heated surface induces a liquid motion, which in turn creates forced convection conditions. Thus, heat is transported in the superheated liquid as sensible heat. Then, the hydrodynamic drag force associated to the departure of vapour bubbles disturbs periodically the thermal boundary layer created by transient heat conduction in the vicinity of the wall. Furthermore, vapour bubbles are generated by vaporization of the super-heated liquid and by microlayer evaporation in the thin film trapped below the bubbles. Hence, heat transfer occurs in the form of latent heat. All these mechanisms act synergistically (Figure 2.2) and are responsible for the increase in heat transfer in the nucleate pool boiling regime.
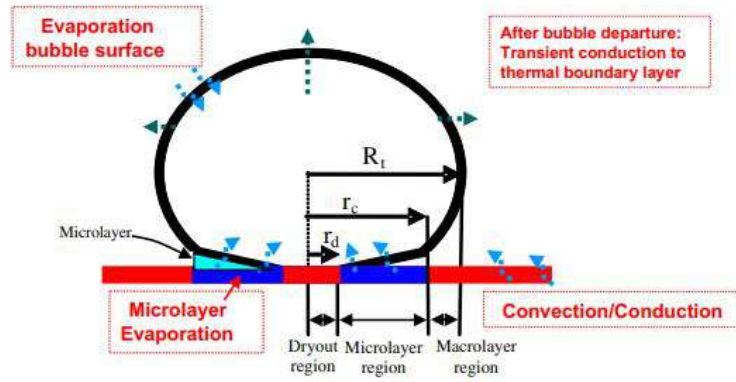
Figure 2.2: Combined heat transfer mechanisms in the nucleate pool boiling regime [34]

Additionally, improved boiling heat transfer may result from the Marangoni effect, which causes a flow from regions with lower surface tension to regions with higher surface tension. Indeed, temperature gradients in the liquid phase create surface tension gradients (i.e. in general, liquids exhibit decreasing surface tension with increasing temperature). This phenomenon, depicted in Figure 2.3 for a departing vapour bubble, becomes more pronounced in the case of subcooled pool boiling [94].
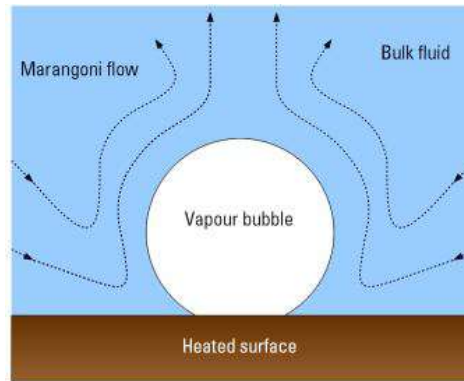
Figure 2.3: Marangoni effect [112]

At ONB, an increase in heat flux is accompanied by a decrease in wall superheat due to the activation of a large number of nucleation sites. This phenomenon, known as *kickback*, is not observed when the heat flux is gradually reduced (i.e. moving from the right to the left side of the boiling curve), meaning that the boiling curve is characterized by so-called temperature overshoot hysteresis [5], as shown by the line FF' in Figure 2.1.

Furthermore, while in the partial nucleate boiling regime (region II) only isolated bubbles are formed on the heating surface, when the heat flux is further increased, vapour bubbles coalesce in vertical direction creating vapour columns or in horizontal direction leading to the growth of mushroom-type bubbles. These larger bubbles are able to transport more latent heat away from the surface and increase the convective heat transfer by stirring the liquid near the surface, resulting in augmented heat flux. This can be seen in the boiling curve, which becomes steeper between points B and C (fully developed boiling region). The heat transfer in this region is mostly described by the Rohsenow correlation [103], which reads as follows:

$$q = \mu_f h_{fg} \left[\frac{g \left(\rho_f - \rho_g \right)}{\sigma} \right]^{1/2} \left[\frac{c_{pf} \left(T_w - T_{sat} \right)}{C_{sf} h_{fg} \mathrm{Pr}_f^n} \right]^3 \tag{2.1}$$

where C_{sf} is an empirical proportionality constant dependent on the heater material and the surface-fluid combination; the fluid Prandtl number exponent n is also derived experimentally.

The heat flux in the fully developed nucleate boiling regime cannot be increased indefinitely. In fact, there is a limit above which the amount of vapour at the heating surface is so large that it prevents the liquid from flowing to the surface. This corresponds to the maximum in the boiling curve, indicated by point C, which marks the critical heat flux (CHF). The high number of bubbles leads to the formation of a vapour blanket on the surface, which in turn is effectively insulated. As a consequence, in heat flux-controlled systems a rapid excursion in the surface temperature is observed, as indicated by the line CE in Figure 2.1. If the temperature at point E exceeds the melting temperature of the material, it will cause *burnout* of the heater.

After occurrence of CHF, depending on whether heat input rate or wall temperature is controlled, the surface experiences either film boiling (region V) or transition boiling (region IV), respectively. Transition boiling is an unstable process as the surface is alternately covered with a vapour blanket and a liquid layer, causing oscillating surface temperatures [116]. Indeed, intermittent wetting of the surface occurs and large patches of vapour are released from the surface [17]. If the power input to the heater is maintained, the surface temperature rises to point D while the heat flux decreases reaching a minimum q_{min}, called the Leidenfrost point. Subsequently, during film boiling a stable vapour film is present on the heating surface and regularly spaced bubbles depart from the surface, which is no longer in contact with the liquid phase. Therefore, the dominant heat transfer mechanisms become conduction and radiation, whose contribution is more significant at higher wall superheat.

As mentioned above, the boiling curve is characterized by hysteresis. Therefore, different process paths are observed for increasing and decreasing applied heat flux, as indicated by the rightward and leftward arrows in Figure 2.4. It should be noticed that the dashed part of the curve (i.e. the transition boiling regime) is bypassed when the heat flux is the controlled variable, meaning that the system must operate below the CHF to avoid a sudden temperature jump which may lead to failure of the heating element.
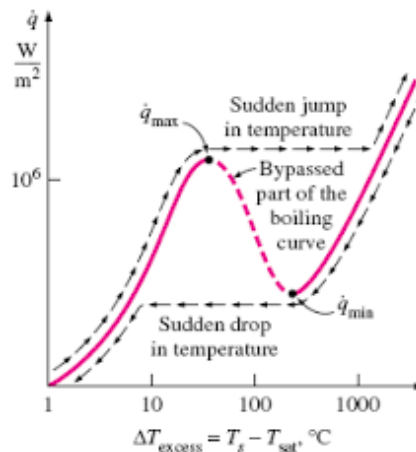
Figure 2.4: Boiling curve hysteresis [36]

2.3. Critical heat flux

The expression for the CHF was first derived by Kutateladze [69] by dimensional analysis:

$$q_{CHF} = C \cdot \rho_v \cdot h_{fg} \cdot \left(\frac{\sigma g \left(\rho_l - \rho_v \right)}{\rho_v^2} \right)^{1/4} \tag{2.2}$$

where the constant C was determined empirically and set to be equal to 0.16 for flat plates.

In order to explain the mechanism leading to the departure from nucleate boiling, Zuber [133] developed a hydrodynamic theory of maximum heat flux, which occurs at the onset of a hydrodynamic instability. Since the bubble population increases with heat flux, its critical value may be attained when vapour bubbles obstruct the path of the incoming liquid. Therefore, Zuber's analysis for CHF prediction

was based on the idea that liquid-vapour interfaces become unstable according to the criterion of a Helmholtz instability. This phenomenon refers to the breakup of two overlying fluid layers in relative motion (Figure 2.5). Indeed, when two immiscible fluids flow relative to each other along an interface, there is a maximum relative velocity above which an infinitesimal disturbance of the interface will grow with time, causing the flow to become unstable.
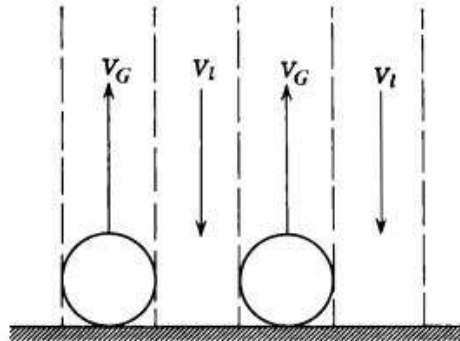
Figure 2.5: Vapour-liquid counterflow in pool poiling [116]

Moreover, Zuber included in his analysis another hydrodynamic aspect of the boiling crisis, the incipience of stable film boiling, and he derived a criterion for stable film boiling from the Taylor instability theory. This states that the stability of an interface of wave form between two fluids of different densities depends on the balance between the surface tension energy and the sum of the kinetic and potential energy of the wave. In order for a fluid underneath a layer of a higher density fluid to meet the stability condition, it must hold that the surface tension energy is greater than the sum of the kinetic and potential energy. To satisfy this requirement, the wavelenght must be smaller than a certain critical wavelenght:

$$\lambda_0 < \lambda_c = 2\pi \sqrt{\frac{\sigma}{g\left(\rho_f - \rho_g\right)}} \tag{2.3}$$

In a pool boiling system, the wavelenght may be interpreted as the distance between nucleation sites or as the departure bubble size. As illustrated in Figure 2.6, Zuber assumed that vapour jets leaving the heating surface have average diameter equal to half of the Taylor wavelength and the spacing between them is equal to one Taylor wavelenght λ_T, with $\lambda_c < \lambda_T < \lambda_d = \sqrt{3}\lambda_c$. Finally, he obtained equation 2.2 with $C = \frac{\pi}{24}$.

Later studies by Lienhard et al. [76] have extended the model proposed by Zuber to finite surfaces, such as small plates and cylinders, by adding a multiplying constant K to equation 2.2. This constant is expressed as a function of a dimensionless characteristic length L':

$$L' = 2\pi\sqrt{3}\frac{L}{\lambda_d} \tag{2.4}$$
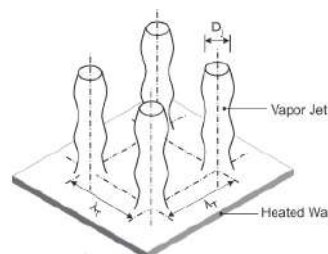
Figure 2.6: Vapour jet configuration for pool boiling on a horizontal flat-plate heater, as postulated by Zuber [73]

The aforementioned CHF models based on instability concepts have been classified as *far-surface models*. However, subsequent experiments by Gaertner [31] and Van Ouwerkerk [119] using high-

speed photography highlighted the relevance of vapour-liquid structures and dry areas (spots) on the boiling surface for the CHF. These observations paved the way to the so-called *near-surface models*, according to which the CHF is triggered by the complete dryout of the macrolayer on the boiling surface before the departure of large vapour mushroom bubbles [43].

Further high-speed optical and infrared imaging analysis of pool boiling [23] have led to the conclusion that the boiling crisis phenomenon may be explained in terms of competition between liquid rewetting of the dry spot, due to gravitational and capillary forces, and enhanced liquid evaporation, due to increased surface temperature. It was demonstrated that the thermal behaviour of the heated substrate is substantially different when the applied heat flux is close to the critical value. Figure 2.7a shows that at low input heat flux a single vapour bubble forms and departs from the surface. The hot spot formed underneath is colder than the surrounding fluid as it is cooled by evaporation of the liquid microlayer and then by lateral diffusion of heat at the contact line. Contrarily when the heat flux approaches the CHF (Figure 2.7b), the surface temperature at the center of the dry spot decreases slightly but it starts increasing immediately after. This temperature rise is then partially compensated by the rewetting action of the liquid surrounding the hot spot. However, when the supplied heat flux equals the CHF, the dry spot becomes irreversible due to the fact that the liquid microlayer dries up before fresh liquid may reach the surface.
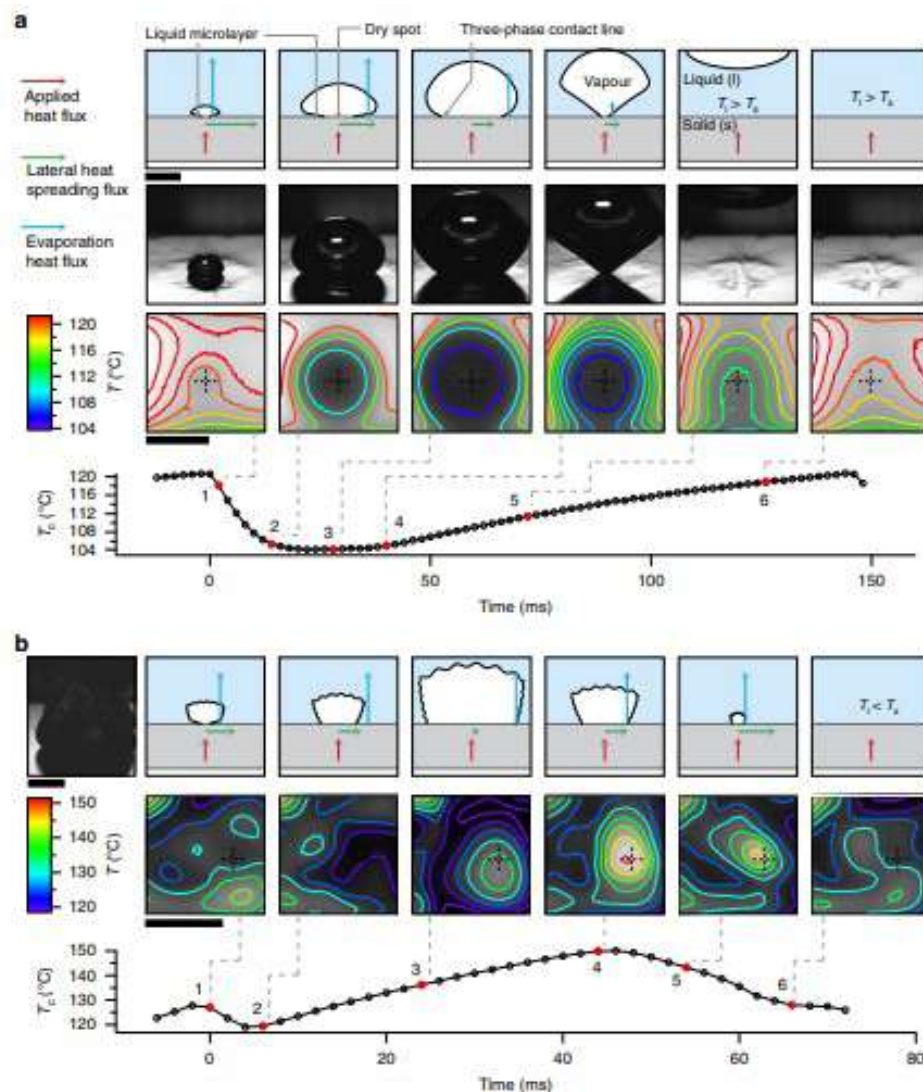
Figure 2.7: Different behavior of hot spots at low (a) and high (b) applied heat flux [23]

2.4. Bubble dynamics

Since heat transfer enhancement resulting from liquid to vapour phase change is intrinsically related to nucleation and growth of vapour bubbles, bubble dynamics play a crucial role in boiling heat transfer. Bubble dynamics includes the different phases representing the life-cycle of a bubble, namely nucleation, initial growth, intermediate growth, asymptotic growth, departure. A waiting period occurs after the departure of a single bubble and before the next one is formed (Figure 2.8), as the liquid needs to replenish the space vacated by the bubble and the thermal boundary layer in proximity of the heating surface is restored as a consequence. It should be noted that this waiting period between two consecutive nucleation events is defined only in the lower heat flux range, which is characterized by discrete bubbles formation.

Nucleation in a pure liquid, referred as homogeneous nucleation, requires the liquid to be superheated. Moreover, a vapour nucleus turns into a useful seed for subsequent bubble growth provided that it exceeds the size corresponding to the thermodynamic equilibrium of the liquid. Combining the Laplace equation at the vapour-liquid interface and the Clausius-Clapeyron relation yields the equilibrium bubble size R:

$$R = \left(\frac{2\sigma}{h_{fg}\rho_G} \right) \left(\frac{T_{\text{sat}}}{T_G - T_{\text{sat}}} \right) \tag{2.5}$$

Heterogeneous nucleation, which occurs at preferential location on the heating surface (such as cavities and scratches), will be further discussed in Section 2.5.1.

Initial growth from the nucleation size is controlled by inertia and surface tension effects. At first bubble growth is slow but as the bubble size increases, the surface tension is reduced so the growth rate increases. During the intermediate stage, bubble growth is accelerated due to increasing contribution of the heat transfer process, while inertia effects become less significant. In the asymptotic stage, the heat transfer rate for the surrounding liquid determines the bubble growth rate.
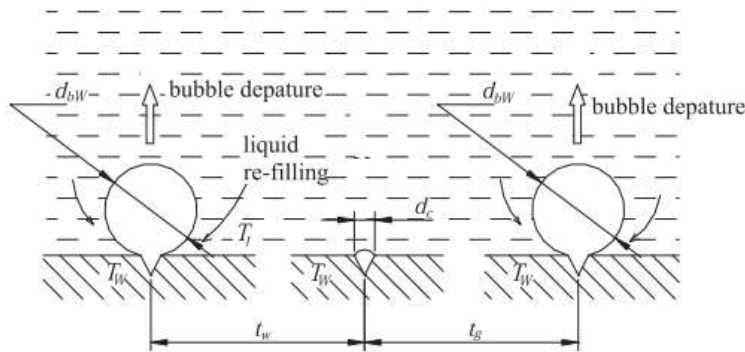
Figure 2.8: Life-cycle of a bubble [72]

2.4.1. Bubble growth rate

Earliest studies on modeling the bubble growth were based on the assumption that such a process results from the evaporation of the superheated liquid surrounding a vapour bubble. Hence, flow dynamics and heat transfer are coupled, as postulated by Plesset and Zwick [98], who developed the first theory for the growth of spherical vapour bubbles in a sea of superheated liquid. However, bubbles departing from a heated surface change shape continuously during their growth and only the microlayer surrounding the bubble is superheated. In order to account for these effects, Mikic at al. [83] proposed an expression of bubble growth rate as a function of the waiting period t_w:

$$\frac{\mathrm{d}D^*}{\mathrm{d}t^*} = 2\left[t^* + 1 - \theta \left(\frac{t^*}{t^* + t_w^*} \right) \right]^{1/2} - t^{*1/2} \tag{2.6}$$

where

$$D^* = \left(\frac{b\rho_v \Delta T h_{fg}}{\rho_l T_{sat}}\right)^{1/2}\left(\frac{\pi D}{12\alpha_l Ja^2}\right)$$

$$t^* = \left(\frac{b\rho_v \Delta T h_{fg}}{\rho_l T_{sat}}\right)\left(\frac{\pi t}{12\alpha_l Ja^2}\right) \tag{2.7}$$

$$\theta = \frac{T_w - T_l}{\Delta T}, \text{ and } Ja = \frac{\rho_l c_{pl}\Delta T}{\rho_v h_{fg}}$$

In the above equations, T_l denotes the liquid bulk temperature and b is a geometric parameter with the value of $2/3$ and $\pi/7$ for a perfect spherical bubble and bubble attached to the heater surface, respectively.

2.4.2. Bubble departure diameter

Bubble size at departure may be derived from a dynamic force balance on the bubble, considering surface tension, buoyancy, liquid inertia due to bubble growth, viscous forces, and forces due to the liquid convection around the bubble [116]. In particular, surface tension acts along the contact line and tends to retain the bubble in place. The buoyancy force for an upward-facing heating surface is the driving mechanism for bubble detachment. The inertial force is the limiting factor in initial bubble growth as it determines the rate at which the vapour can displace the surrounding liquid. Additionally, the bubble departure diameter is affected by the wall superheat, contact angle and thermophysical properties of the fluid and vapour phases [35]. Since the shape of a vapour bubble evolves during the growth process, the bubble departure diameter is defined as an equivalent diameter, i.e. diameter of a spherical bubble with the same volume of the actual bubble.

Hatton and Hall [45] conducted a detailed study on bubble departure and expressed the net force balance as follows:

Buoyancy force $= ($ drag force $+$ liquid inertia $+$ vapor inertia$)$

$- ($ surface tension $-$ excess pressure $)$

Moreover, they concluded that for small surface cavities the bubble departure diameter depends mainly on buoyancy and liquid inertia, while for larger cavity sizes buoyancy and surface tension are the dominant forces. Regarding the latter case, the first correlation was given by Fritz [110] as follows:

$$D_d = 0.0208\,\theta\sqrt{\frac{\sigma}{g(\rho_l - \rho_v)}} \tag{2.8}$$

However, since the above equation takes into account surface tension and buoyancy only, it is not able to predict the bubble departure diameter with sufficient accuracy, especially at high pressures. Subsequently, Cole and Rohsenow [16] derived more accurate correlations based on their experimental results:

$$D_d = 1.5 \times 10^{-4}\sqrt{\frac{\sigma}{g(\rho_l - \rho_v)}}Ja^{*5/4} \text{ for water} \tag{2.9}$$

$$D_d = 4.65 \times 10^{-4}\sqrt{\frac{\sigma}{g(\rho_l - \rho_v)}}Ja^{*5/4} \text{ for other liquids} \tag{2.10}$$

where

$$Ja^* = \frac{\rho_l c_{pl} T_{sat}}{\rho_v h_{fg}} \tag{2.11}$$

At high heat flux, when the effect of inertia becomes significant, the following correlation was proposed by Gorenflo et al. [38] :

$$D_d = c_1 \left(\frac{Ja^4\alpha_l^4}{g}\right)^{1/3} \left(1 + \left(1 + \frac{2\pi}{3Ja}\right)^{1/2}\right)^{4/3} \tag{2.12}$$

2.4.3. Bubble departure frequency

According to Griffith [39], the inertia of the liquid promotes bubble detachment as fresh liquid flows behind the departing bubble, comes into contact with the surface and helps carrying the bubble away. Hence, a time interval t_d is required for bubble departure and a waiting period t_w is a needed for growth of the next bubble from the same nucleation site. Bubble departure frequency f_b is then defined as follows:

$$f_b = \frac{1}{t_w + t_d} \tag{2.13}$$

As the heat flux is increased, more nucleation sites become active and both t_d and t_w are reduced. The rapid growth of a bubble is also responsible for increased inertial effect on the vapour bubble, thus the bubble departure size decreases. Peebles and Garber [93] proposed the following correlation for f_b:

$$f_b = \frac{1}{D_b}\left(1.18\left(\frac{t_g}{t_g + t_w}\right)\left[\frac{\sigma g\,(\rho_l - \rho_v)}{\rho_l^2}\right]^{1/4}\right) \tag{2.14}$$

where t_g indicates the growth time.

If the heat flux is high enough that $t_w \ll t_d$, the bubble generation rate reaches its maximum as the vertical distance between successive bubbles approaches to zero. Hence, the following simplified relation holds:

$$v_b = D_b f_b \tag{2.15}$$

where v_b indicates bubble velocity. Based on experimental data, Ivey [48] showed that equation 2.15 is approximately correct at high heat fluxes and large bubble sizes. However, he also pointed out that a single relation between f_b and D_b does not exist for the entire size range. In fact, depending on D_b and and applied heat flux, experimental results of different fluids were found to fall into three different regions (hydrodynamic, thermodynamic, and transition region), which are characterized by different f_b - D_b correlations.
In the first region buoyancy and drag force are dominant; in the thermodynamic region the frequency of bubble formation is governed by thermodynamic conditions during growth; in the transition region buoyancy, drag, and surface tension forces are all of the same order of magnitude. For the hydrodynamic region the following equation was obtained:

$$D_b^{1/2} f_b = c g^{1/2} \tag{2.16}$$

where the constant c ranges from 0.9 to 1.2 depending on the fluid. According to Ivey, equation 2.16 holds for moderate to high heat fluxes and medium to large bubbles.
In the thermodynamic region, which is encountered in the case of small to medium size bubbles at very low heat flux, the following expression was found:

$$D_b^2 f_b = \text{constant} \tag{2.17}$$

For the intermediate region, the following correlation was proposed:

$$(D_b)^{3/4} f_b = 0.44 g^{1/2} \tag{2.18}$$

2.4.4. Nucleation site density

Nucleation site density N_a, which is defined as the ratio of the number of active nucleation site to the boiling surface area, is a key parameter for boiling heat transfer as the the amount of heat transported from the heated surface depends on how many nucleation sites are active. Since it is difficult to measure accurately the actual nucleation site density by visualization and counting techniques, several models have been developed to predict N_a. Benjamin and Balakrishnan [10] proposed an expression for N_a including the effect of the wall superheat, surface and fluid properties:

$$N_a = 218.8 \frac{1}{\gamma} \Pr^3 R_{nd}^{-0.4} \Delta T^3 \tag{2.19}$$

$$R_{nd} = 14.5 - 4.5 \left(\frac{R_a P}{\sigma} \right) + 0.4 \left(\frac{R_a P}{\sigma} \right)^2 \tag{2.20}$$

where R_{nd} is the non-dimensional surface roughness, R_a the average surface roughness, P is the system pressure, and γ is the surface-liquid interaction parameter, defined as follows:

$$\gamma = \sqrt{\frac{k_s \rho_s c_{P_s}}{k_l \rho_l c_{P_l}}} \tag{2.21}$$

Moreover, it must be noted that wettability also affects the activation of surface cavities. In order to take this effect into account, Wang and Dhir [123] suggested N_a to be proportional to $1 - cos\theta$, where θ indicates the contact angle.

2.5. Effect of system variables

As outlined in Section 2.1, being characterized by high heat removal rate, nucleate pool boiling is the most favorable operating regime for heat transfer applications (i.e. shell-and-tube evaporators and immersion cooling of electronic components). Nonetheless, it is a complex process as it is influenced by numerous system variables. Since these factors are inter-linked with each other, comprehensive theoretical description of the boiling process gets complicated. Earlier works showed that the main parameters affecting the boiling heat transfer coefficient (HTC) are heat flux, saturation pressure, and thermophysical properties of the working fluid. Subsequent studies drew the attention to the role of surface characteristics, such as surface roughness, surface contamination, wettability (quantified by the contact angle), microstructure (including shapes, dimensions and density of pores, which are considered to be vapour bubbles nucleation sites), dimensions, material, and orientation in space [97].

2.5.1. Effect of surface microgeometry

In order to quantify surface microgeometry, surface roughness parameters, namely average R_a, root-mean-square R_q, mean-total R_z surface roughness, are used.

Nucleate boiling is very sensitive to surface topography as active nucleation sites distribution along with size and shape of the cavities have a direct impact on the nucleation and growth of vapour bubbles. Therefore, in order to clarify the effect of roughness parameters on boiling heat transfer, first the principles of nucleation at a heated surface must be understood. Figure 2.9 shows nucleation cavities on a surface and static or equilibrium contact angle ϕ, which is defined as the angle that a liquid-vapour interface makes with a solid surface and it is measured from the solid substrate to the interface through the liquid. A large angle ϕ may be more prone to trap gas inside the cavity by a capillary effect and thus favour nucleation [116].
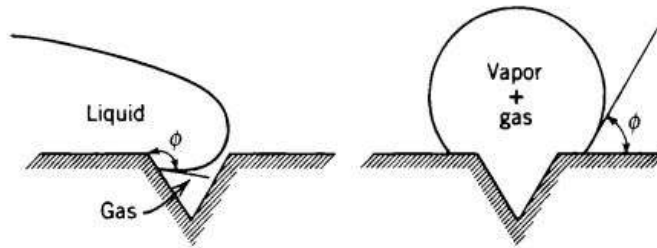
Figure 2.9: Nucleation from cavities [116]

Hsu and Graham [46] developed a model of the ebullition cycle in nucleate boiling based on their experimental analysis of the same. Using Schlieren and shawdograph imaging, they were able to record the boiling process and thus describe it analytically. They observed that surface cavities, which are potential sites for bubbles nuclei, become active provided that a superheated thermal boundary layer is established in proximity of the surface. Then bubbles undergo a rapid growth causing the boundary layer to be disturbed and displaced by one bubble diameter away from the nucleation site. Therefore, there is a definite time interval required for the liquid adjacent to the surface to reach again the superheated conditions allowing the recovery of the thermal boundary layer. After this waiting period, the nucleate boiling cycle recurs. Assuming a linear thermal boundary layer thickness δ, in which the heat transfer mechanism is transient conduction, the associated temperature profile may be derived. Furthermore, in order to meet the condition for bubble growth, the temperature in the boundary layer must be at least equal to the temperature of the bubble nucleus T_b so that an inward heat flow through the bubble interface occurs. As shown in Figure 2.10, there is a specific range of cavity size for which the bubble temperature is lower than the liquid temperature at the bubble cap, corresponding to the range in which the bubble embryo will grow to make a cavity into an active site [116]. Thus the active cavity size range may be derived by solving the following equations:

$$\frac{T_b - T_\infty}{T_n - T_\infty} = \frac{\delta - C_1 r}{\delta} \tag{2.22}$$

$$T_b - T_{\text{sat}} = \frac{2\sigma T_{\text{sat}}}{C_2 r_c H_{fg} \rho_G} \tag{2.23}$$
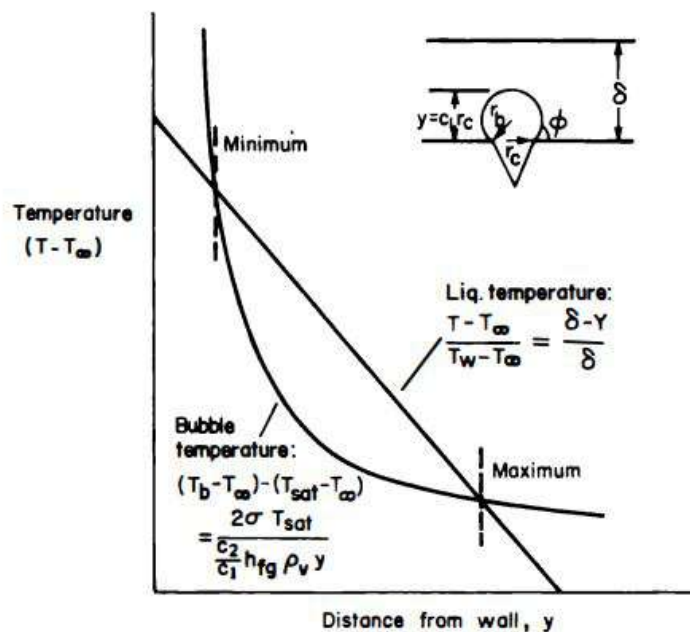
Figure 2.10: Criterion for activation of nucleation sites according to Hsu and Graham [116]

Hence, the model proposed by Hsu allows to estimate the relevant size range for surface cavities to be considered as active nucleation sites. As a consequence, surface roughness may have a significant effect on the HTC only when roughness changes are such that new active nucleation sites are created. Thus, if large cavities result from surface roughness variation, then this change has no impact on the HTC [7]. Conversely, for the roughness range produced by typical surface finishing process ($R_a = 0.05 - 0.4 \ \mu m$), such as mirror finishing and lapping, small changes in surface roughness may cause an appreciable variation in the number of potential active nucleation sites [100]. Similarly, experimental results obtained by Benjamin and Balakrishnan [9] demonstrated that different surfaces treated with various emery papers grades (giving a roughness range of $R_a = 0.07 - 1.17 \ \mu m$) leaded to a noticeable change in the HTC of the tested fluids (water, CCl_4, acetone, and n-pentane).
Similarly, experiments conducted by Kim et al. [60] on pool boiling of water on aluminium surfaces, showed that as the R_a parameter is increased, the boiling curve shifts progressively to the left (Figure 2.11).
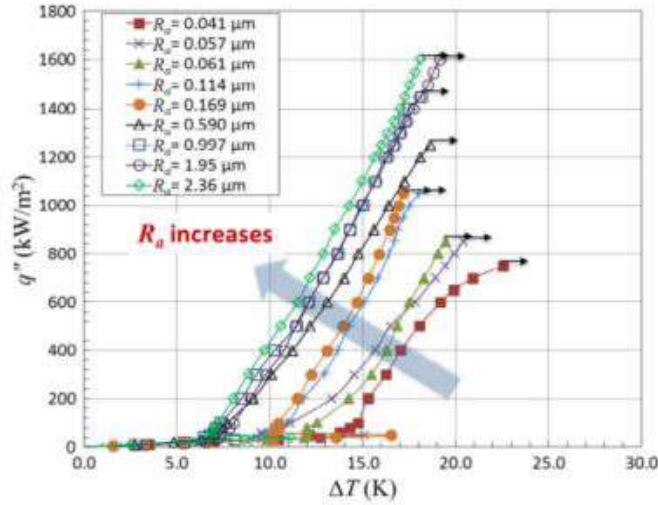
Figure 2.11: Effect of R_a on the boiling curve of water [60]

Moreover, continuous advancements in micro- and nano-fabrication technologies have enabled the manufacturing of structured surfaces, which include micropillars [62, 132, 25], microchannels [49], micromeshes [71, 92], reentrant cavities [21], nanotubes [68] and nanowires [14]. Different combinations of these micro/nano-scale features have been explored in order to enhance the HTC and CHF simultaneously [102, 57]. In particular, being the bubble nucleation size in the microscale range, microstructured surfaces have been found to increase the nucleation site density, resulting in higher HTC. On the other hand, nanostructures do not affect the number of nucleation sites but they are able to improve the boiling performance due to their larger specific surface area and they act as efficient wicking surfaces facilitating liquid rewetting.

2.5.2. Effect of heater size

It is generally understood that boiling in Earth gravity is buoyancy dominated and independent of the heating surface size provided that the heater dimensions are above a critical value [61]. In particular, the heater size L_h (indicating the width or the diameter in the case of heating plates or wires, respectively) must be larger than the capillary length L_c:

$$L_c = \sqrt{\frac{\sigma}{g(\rho_l - \rho_v)}} \tag{2.24}$$

Indeed, if $L_h < L_c$, the maximum bubble size is comparable to the heater size thus the boiling curve is specific to the heater dimensions. Therefore, $L_h >> L_c$ must be satisfied to neglect the size effect due to the heater.

2.5.3. Effect of surface orientation and geometry

A change in surface orientation has a direct impact on the heat transfer process as a result of the modified bubble dynamics. Indeed, when the inclination of the heating surface with respect to the horizontal position is increased, vapour bubbles tend to slide along the wall before departing from it. Bubble sliding (seen in Figure 2.12a) is responsible for cyclic disruption and reformation of the thermal layer adjacent to the surface, resulting in enhanced heat transfer by transient conduction from the wall, as reported by Sateesh et al. [109]. These results are in good agreement with the previous experimental work by Nishikawa et al. [52], who studied nucleate boiling on flat plates at different inclination angles. In particular, it was found that higher inclination angles lead to increased heat transfer, as shown in Figure 2.12b.

(a) Bubble sliding mechanism [109]

(b) Experimental data [52]
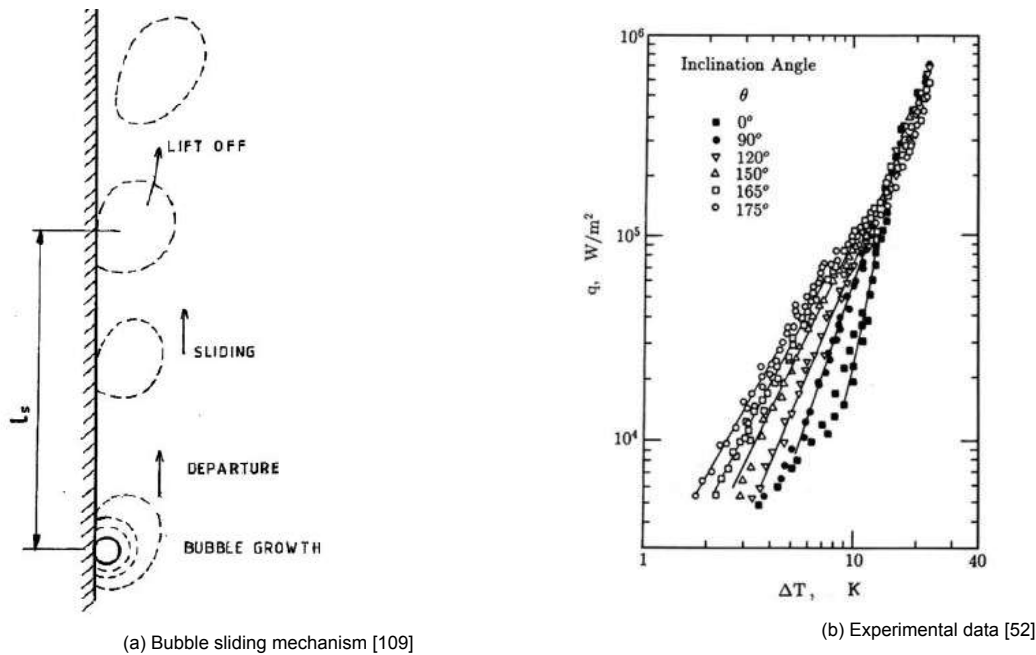
Figure 2.12: Effect of surface orientation on boiling heat transfer

2.5.4. Effect of surface wettability

The static or equilibrium contact angle is an indicator of the wettability characterizing a solid substrate. The contact angle θ results from the balance of the interfacial tensions, namely the solid-liquid tension γ_{sl}, the solid-vapour tension γ_{sv} and the liquid-vapour tension γ_{lv} at the three-phase contact line (Figure 2.13. The limiting cases of perfect wetting and absolute non-wetting surfaces are encountered when $\theta = 0°C$ and $\theta = 180°C$, respectively. In the intermediate range, a good wetting corresponds to low contact angle ($\theta < 90°$), while bad wetting to high contact angle ($\theta > 90°$).
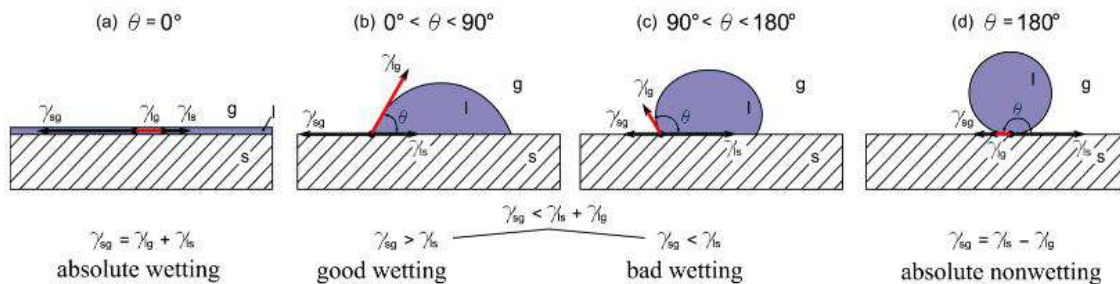
Figure 2.13: Dependence of surface wettability on the static contact angle θ [99]

Surface wettability plays a significant role in influencing the activation of nucleation sites and thus the boiling performance. Indeed, a surface with poor wettability is associated with a low energy barrier for liquid-vapour phase change [89, 63], hence bubble formation is promoted. This leads to increased nucleation density and earlier occurrence of ONB. However, in the high heat flux range, too many active nucleation sites might accelerate coalescence between closely packed vapour bubbles, resulting in a lower CHF than a hydrophilic surface [113]. Conversely, on a surface with high wettability efficient re-wetting by the liquid phase hinders the growth of large vapour bubbles and delays the occurrence of the boiling crisis. The role of surface wettability in the pool boiling process was investigated in detail by Kim et al. [59], who studied experimentally the dynamics of the liquid microlayer and dry spots on surfaces with four different wettabilities (the contact angles measured on the substrates were 65°, 0°, 36°, 88°). The sequential frames given by high-speed imaging revealed that boiling parameters on the Teflon-coated surface, which is relatively hydrophobic, deviate from those of hydrophilic surfaces, whose behavior is qualitatively similar. In particular, it was found that the contact angle near the triple contact line during the bubble growth is about 90° for the Teflon-coated surface whereas it is approximately 0° for the other surfaces, meaning that in the former case no liquid microlayer exist underneath a vapour bubble.
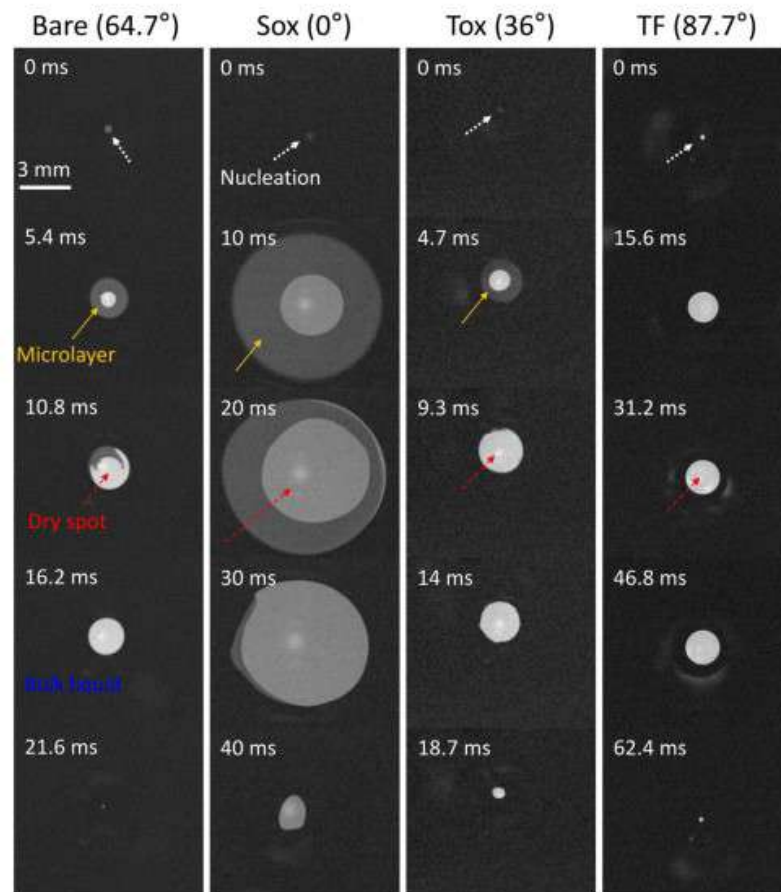
Figure 2.14: Dynamics of dry spot and liquid microlayer under single vapour bubbles on surfaces with different wettabilities [59]

Liaw and Dhir [74] studied extensively the effect of static contact angle variation on vertical surfaces, concluding that with an increase in wettability, the boiling curve is shifted to the right, meaning that the nucleate boiling process becomes less efficient (Figure 2.15).
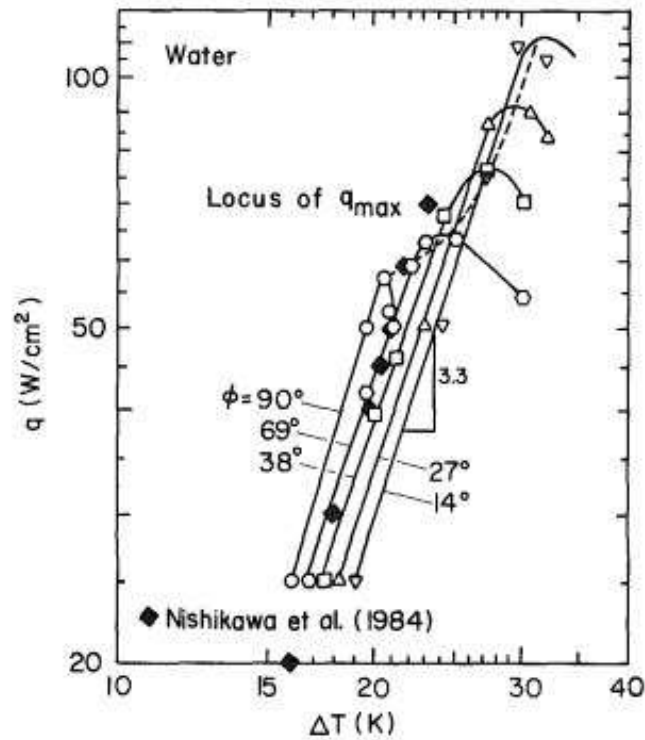
Figure 2.15: Effect of contact angle on boiling heat transfer [74]

2.5.5. Effect of surface contamination

Surface degradation may result from physical modification and chemical reactions occurring at the heating surface. In particular, the presence of foreign material may reduce the number of active nucleation sites and change the surface wettability. Furthermore, if oxygen is contained in the heat transfer fluid, aging of the surface may occur. Hence, the metal ions combine with oxygen to form metal oxides that precipitate around the mouth of the surface cavities or at the base of vapour bubbles, where high heat and mass transfer gradients exist [67]. The resulting effect is similar to that of improved wettability, which deteriorates boiling heat transfer.

<div style="text-align: right; font-size: 3em;">3</div>

Boiling with nanofluids

3.1. Introduction

The original idea that led to the development of nanofluids was to improve the thermal conductivity of traditional heat transfer media by adding nano-sized solid particles, which are characterized by up to three order of magnitude higher thermal conductivity (Figure 3.1). Since the pioneering work of Choi [15], numerous studies have followed, suggesting that the addition of nanoparticles to base fluids has more complex implications than the change in mean thermophysical properties of the suspension. In fact, at nanoscale particles exhibit a distinct behavior as compared to the bulk material and as a consequence interactions between particles, liquid phase and heating surface are modified [126]. This has a significant impact on boiling heat transfer, which is not solely dependent on the bulk properties of the working fluid, but it is also very sensitive to surface characteristics and bubble dynamics, which are altered by the presence of nanoparticles.
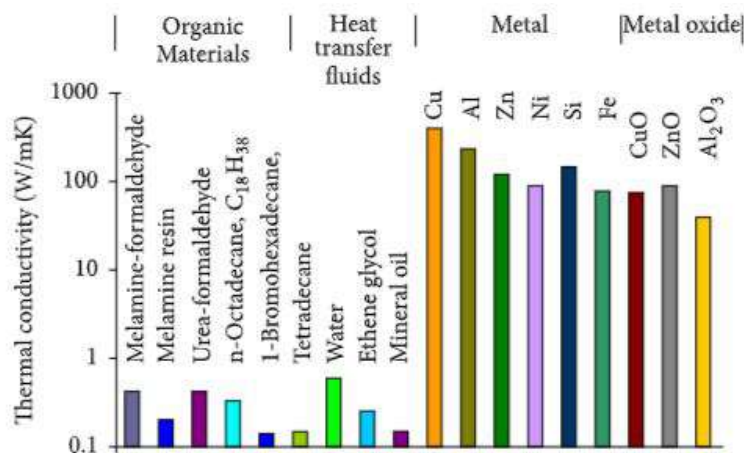
Figure 3.1: Thermal conductivity comparison of common materials [128]

3.2. Thermal conductivity enhancement

Since nanofluids consist of tiny solid particles dispersed in a liquid phase, traditional macroscopic models of heat transport in composite materials fail in predicting the experimentally observed enhancement in the thermal conductivity of nanofluids. Indeed, classical theories of the effective thermal conductivity

of composites and mixtures were based on the continuum assumption and postulated heat transfer to be diffusive both in the liquid and solid phase. Prediction of the effective thermal conductivity of suspensions by the Maxwell [81] and Hamilton-Crosser [42] models is based only on the volume concentration and shape of nanoparticles. Bruggeman's effective medium theory [12], which is applicable to a wider range of concentrations, has a similar nature. Taking into account solely the two aforementioned factors, conventional approaches are inadequate to explain the peculiar heat conduction properties of nanofluids and the anomalous increase in their thermal conductivity as reported by experimental studies [2].

Further developments of the classical models included the effect of particles distribution [122] and interactions [131]. Moreover, a significant contribution to the analysis of the peculiar heat conduction characteristics of nanofluids was given by the study of Keblinski et al. [54]. Their work showed that the key factors characterizing the thermal properties of nanofluids are ballistic rather than diffusive and they explored the role of particles mobility and solid/liquid interfaces, in contrast with the fundamental assumption of traditional approaches, which consider the particles to be motionless [81, 91]. However, at nano-scale, particles become subject to Brownian motion, which is the movement of particles due to random collisions with the molecules of the surrounding liquid. Due to Brownian motion, nanoparticles behave as "stirrers" that induce microconvection currents in the fluid and thus increase the effective thermal conductivity [50]. Secondly, heat conduction is augmented by the effect of nanoparticle clustering. Indeed, nanoparticles suspended in the liquid are not isolated but they tend to interact and aggregate with each other [124]. Even though such clusters may eventually pose stability issues, if they are small enough to remain suspended in the liquid phase they facilitate heat transfer via conduction as they are oriented in the direction of the heat flux [125].

Moreover, liquids tend to assume a more ordered structure near a solid surface, creating a layer of atomic thickness ($\sim 1\ nm$) at the interface with the nanoparticles [27]. Since crystalline solids are characterized by lattice arrangements of atoms, the liquid nanolayer is more ordered than the bulk fluid by interface effect. Therefore, assuming that the thermal conductance is mostly the same as that of nanoparticles [50], the effective thermal conductivity is enhanced.

Furthermore, in crystalline solids heat conduction takes place by propagating lattice vibrations, i.e. by phonon transport. Phonons propagate randomly and are scattered by each other or by defects. However, if the mean free path of a phonon, which may be calculated with Debye theory, is greater than the average dimensions of the nanoparticles, ballistic rather than diffusive phonon transport is likely to take place across the nanoparticle surface through the fluid reaching a nearby particle. As a result, an increase in thermal conductivity is expected [54]. Nonetheless, the mean free path in the liquid phase is shorter than in the solid phase, thus such an effect may be effective provided that the distance between nanoparticles is in the order of the liquid nanolayer.

Thermophoresis is referred as the movement of nanoparticles under a temperature gradient. Similarly and in combination with Brownian motion, localized convectional currents arise, which may contribute to increase the thermal conductance in nanofluids [11].

Lastly, as the suspended nanoparticles carry heat with them it has been hypothesized that near-field radiation may be a cause for increased thermal conductivity. However, radiation effect is smaller than heat conduction through a medium, thus its effect is considered to be negligible [124].
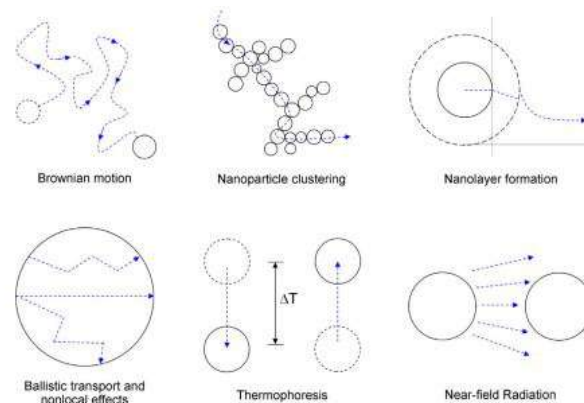
Figure 3.2: Mechanisms of heat conduction in nanofluids [11]

3.3. Nanoparticles deposition

Experimental investigations [64, 121, 117, 70] have proved that deposition of a porous nanoparticles layer occurs under pool boiling conditions with nanofluids. Indeed, similarly as described in Section 2.1, microlayer evaporation is the physical mechanism leading to the formation of vapour bubbles. Additionally, in the case of nanofluids, the region where the evaporation of the thin superheated liquid film has occurred experiences an increase in the concentration of nanoparticles and a decrease in the distance between them (Figure 3.3). Hence, the increased possibility of collisions and agglomeration finally leads to deposition of nanoparticles [117].
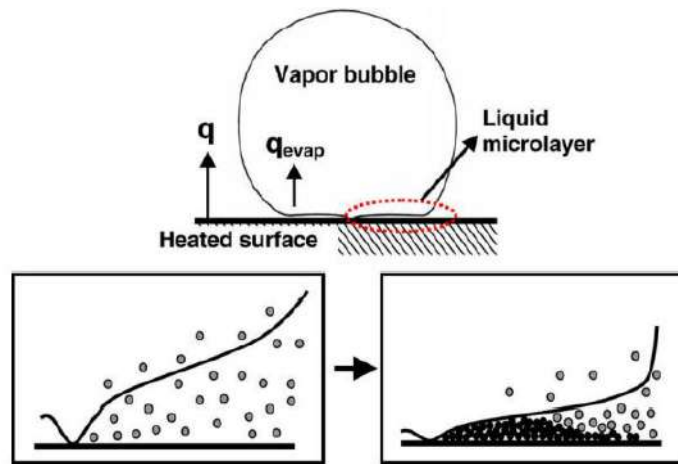
Figure 3.3: Deposition of nanoparticles at the heating surface as a result of microlayer evaporation [70]

Thus, the heating surface is effectively covered by a coating layer, whose thickness and structure evolve during the boiling process [78, 70, 44]. Therefore, deposited nanoparticles may lead to significant changes in surface roughness, wettability, active nucleation site density, and near-surface hydrodynamics. As a result, heat transfer parameters (HTC and CHF) may exhibit a transient behaviour as the characteristics of the porous layer vary with time [70, 95]. The structure of the nanolayer is closely related to the concentration and characteristics of nanoparticles, surface temperature, evaporation rate, and heat flux [117]. In particular, at low concentrations the deposited layer is very thin, hence heat transfer parameters are affected by the presence of nanoparticles as far as effective thermal conductivity of the working fluid is concerned. On the other hand, at higher nanoparticle concentrations, the deposition thickness becomes large enough that it acts as an additional resistance to heat transfer, causing deterioration of the boiling performance. Therefore, in order to optimize the efficiency of boiling heat transfer with nanofluids, it is of primary importance to determine the limit value of nanoparticles concentration which gives the maximum critical heat flux and heat transfer coefficient (Figure 3.4). Furthermore, given the unsteady nature of the deposition layer, the exposure to a certain heat flux for a given time determines the growth of a thicker layer at that heat flux level, thus affecting the boiling performance as the heat flux is increased in the next steps. Therefore, such experimental conditions are of primary importance in the assessment of the performance of different nanofluids and their behaviour with respect to that predicted by theoretical models [32].
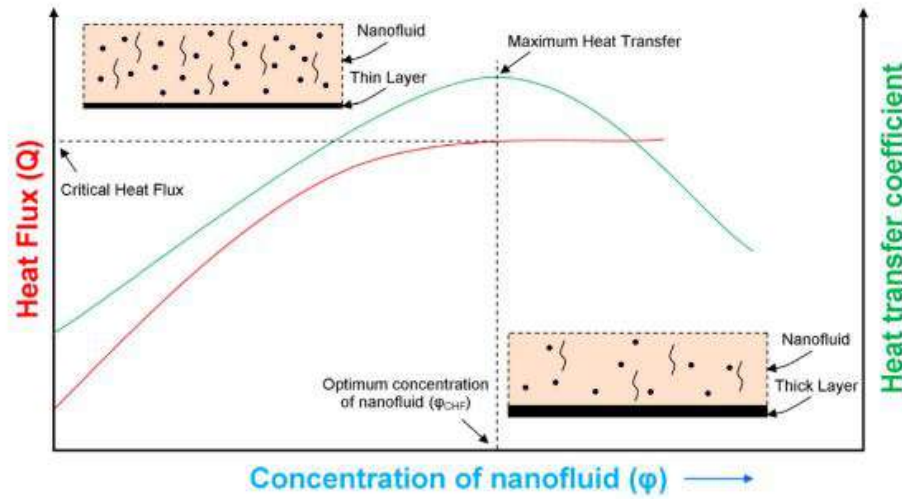
Figure 3.4: Effect of deposition thickness on boiling heat transfer [11]

3.4. Macroscopic view: Modification of the heating surface

As discussed in the previous section, surface modification by nanoparticles was found to be an inherent characteristic of pool boiling with nanofluids. Modified surface topography is reflected in a change in active nucleation site density. This effect may be quantified by means of the surface-particle interaction parameter ψ, which was defined by Narayan et al. [90] as the ratio of average surface roughness R_a to average particle size D_p:

$$\psi = \frac{R_a}{D_p} \tag{3.1}$$

When $\psi > 1$, it signifies that the nanoparticles are much smaller than the cavities at the heating surface so each nucleation site is split into multiple ones, resulting in an overall increase in active nucleation sites. Vice versa, when ψ approaches unity, the sizes of nanoparticles and surface cavities are in the same order of magnitude, thus nanoparticles fill the nucleation sites reducing the nucleation site density.

It must be noted that as surface characteristics are modified by nanoparticle deposition each time after boiling, hence understanding how to control and predict the deposition pattern is crucial to allow reliable boiling applications.

Another aspect associated with the alteration of the heating surface features is the change in wettability and thereby capillary wicking [64, 58]. When boiling nanofluids, wettability enhancement occurs due to the formation of the porous nanolayer. The reason for this behaviour may be explained by the Wenzel's equation, which reads as follow:

$$\cos\theta^* = r\frac{\gamma_{\text{SV}} - \gamma_{\text{SL}}}{\gamma_{\text{LV}}} = r\cos\theta \tag{3.2}$$

In equation 3.2, θ^* represent the apparent contact angle on the deposition layer, θ indicates the static contact angle on the original surface, $\gamma_{\text{SV}} - \gamma_{\text{SL}}$ is the adhesion tension, γ_{LV} is the surface tension, r is a roughness factor defined as the ratio of the effective contact area to the smooth contact area. Since the deposition of nanoparticles increases both the adhesion tension and the effective surface area [64], the apparent contact angle is considerably decreased, resulting in improved wettability of the nanoparticle-fouled surface. As effective contact area increases, the capillarity of the surface is enhanced [108, 3, 51]. This causes the contact line to move in the lateral direction so that a capillary liquid flow occurs as

shown in Figure 3.5. Moreover, capillary wicking during boiling provides fresh liquid supply to the dry region beneath the vapour bubbles, delaying the irreversible growth of hot spots, which are responsible for the boiling crisis [114]. Therefore, re-wetting of the surface due to the combined effect of decreased contact angle and capillary wicking has a beneficial effect on the boiling performance, leading to higher CHF.
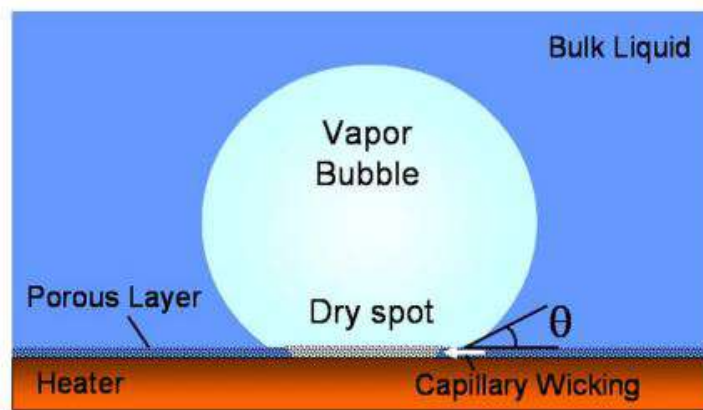
Figure 3.5: Capillary wicking on a porous layer [58]

3.5. Mechanisms of CHF enhancement

As outlined in the previous section, nanoparticle deposition modifies surface characteristics and thus affects CHF. Different theories have been proposed as potential mechanisms for CHF amelioration upon nanoparticle deposition, namely bubble interaction, hydrodinamic instability, hot/dry spot, macrolayer dry-out, and interfacial lift-off.

Among these, the earliest theory was the bubble interaction model proposed by Rohsenow and Griffith [104], who indicated bubble interference as the trigger mechanism for CHF occurrence. Indeed, this model describes initially isolated spherical bubbles that start to coalesce radially at high wall superheats causing the surface to be covered by vapour. Therefore, the radial coalescence of isolated bubbles was deemed to be the trigger mechanism for CHF. However, later experimental studies showed by high-speed imaging that bubble coalescence starts well prior to CHF so the bubble interaction theory was shelved.

The hydrodynamic model developed by Zuber [133] has become well-established over the years as it was the first mechanistic model enabling to predict CHF. However, more recent studies have pointed out the limitations of Zuber theory, according to which the nature of the boiling crisis has to be sought in the macroscopic hydrodynamics. Indeed, experimental evidence [114], showed the scales separation in pool boiling (Figure 3.6). This suggested that two hydrodynamic scales exist: an external and an internal one, with the latter being the microhydrodynamics of liquid microlayer on the heater surface [24]. Since surface properties play a crucial role in pool boiling and they are closely related the microhydrodyanmics, it follows that the physics of the evaporating microlayer must be taken into account when aiming to develop a comprehensive model of the boiling crisis.
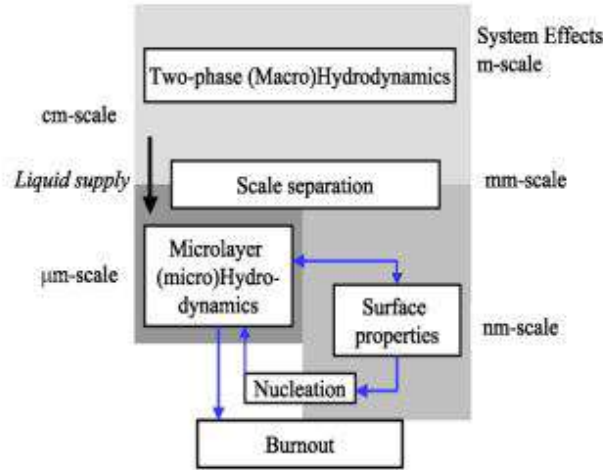
Figure 3.6: Scales separation in pool boiling [24]

Based upon these considerations, Theofanus and Dinh [115] included the microhydrodynamics of the three-phases contact line in the hot/dry spot theory. First, using a high-speed high-resolution infrared camera, they were able to visualize thermal patterns on the heating surface. Cold spots were identified is correspondence of active nucleation sites, as high heat removal takes place underneath growing vapour bubbles. When the surface heat flux is progressively increased, hot spots develop within cold spots upon local disruption of the liquid micro-layer and eventually they become irreversible dry spots at CHF provoking the boiling crisis. Hence, they postulated that the critical condition at burnout is reached when the evaporation recoil force, which causes the liquid meniscus to recede, balances the surface tension force, which drives the meniscus to advance and rewet the hot spot. Based on these force equilibrium, they derived the following expression for the CHF:

$$q_{CHF} = \kappa^{-1/2} \rho_v h_{fg} \left[\frac{\sigma \left(\rho_l - \rho_v \right) g}{\rho_v^2} \right]^{1/4} \tag{3.3}$$

It should be noted that Equation 3.3 has the same form of 2.2 except for the parameter κ, which accounts for surface effects and meniscus flow dynamics. Indeed, κ is the proportionality constant that relates the radius of curvature of the liquid meniscus $\mathcal{R}$ to the capillary length L_c:

$$\mathcal{R} = \kappa \sqrt{\frac{\sigma}{g \left(\rho_l - \rho_g \right)}} = \kappa L_c \tag{3.4}$$

Therefore, the model proposed by Theofanus and Dinh revisits the traditional approach based on macro-hydrodynamics arguments introducing micro-hydrodynamic effects of the liquid meniscus. Moreover, the hot/dry spot theory was found to be in good agreement with experimental data on pool boiling of water-based alumina, zirconia and silica nanofluids tested by Kim et al. [64]. First, they estimated the average radius of curvature of the liquid meniscus $\mathcal{R}$ as follows [40]:

$$\mathfrak{R} = \frac{\sqrt{\frac{\sigma}{g(\rho_l - \rho_v)}}}{\sqrt{1 - \frac{\sin \theta}{2} - \frac{\pi/2 - \theta}{2 \cos \theta}}} \tag{3.5}$$

Then, combining Equations 3.4 and 3.5, they obtained the following expression for κ:

$$\kappa = \left(1 - \frac{\sin \theta}{2} - \frac{\pi/2 - \theta}{2 \cos \theta} \right)^{-1/2} \tag{3.6}$$

Finally, the obtained value for κ gave an accurate estimate of the CHF enhancement obtained from the experimental measurements using nanofluids.

An alternative hydrodynamic model was proposed by Haramura and Katto [43], considering large mushroom-type bubbles which results from coalesced individual bubbles at neighbouring nucleation sites. They assumed that these bubbles are separated from the heating surface by a liquid macro-layer, which was defined as the volume of liquid trapped between the vapour bubbles under the plane of coalescence (Figure 3.7). Fresh liquid is supplied to the heating surface only when the mushroom bubbles depart from the surface, then the macrolayer is formed again and new vapour bubbles begin to grow above it. The time period between inception and departure of mushroom bubbles is called the hovering period [106]. Haramura and Katto postulated that the boiling crisis results from the consumption of the macrolayer by evaporation. Therefore, CHF occurs when the time required for macrolayer evaporation is less than the hovering period. Assuming that the vapour bubbles have the same size and are distributed uniformly over the surface, the equivalent thickness of the macrolayer δ_{e} was estimated to be:

$$\delta_{\mathrm{e}} = r_{\mathrm{b}} \left[\cos \theta - \frac{\pi}{12} \left(3 \cos \theta - \cos^3 \theta \right) \right] \tag{3.7}$$

The time for macrolayer dry-out τ_{d} was derived from the energy balance at the surface, giving:

$$\tau_{\mathrm{d}} = \frac{\delta_{\mathrm{e}} \rho_1 h_{\mathrm{fg}}}{q_{CHF}} \tag{3.8}$$

Therefore, according to the macrolayer model, a decrease in the contact angle θ, results in increased τ_{d}, which in turn delays the departure from nucleate boiling. Again Kim et al. [64] compared their experimental results with the CHF predicted by the macrolayer dry-out theory. It was concluded that even though the macrolayer dry-out theory is less accurate than the dry spot model, the former approach still highlights a strong relation between CHF enhancement and increase in surface wettability due to nanoparticle deposition.
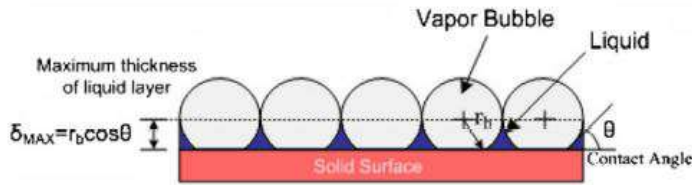
Figure 3.7: Macrolayer concept [106]

3.6. Microscopic view: Bubble dynamics

3.6.1. Bubble parameters

Analytical models for bubble parameters in the case of nanofluid nucleate boiling have not been developed yet. Indeed, little experimental data is available regarding space and time resolved boiling parameters using nanofluids. Significant contribution in this direction was given by Gerardi [35], who provided a systematic method of investigating pool boiling of both pure fluids and nanofluids based on high-speed video and infrared termography. Hence, he was able to measure directly bubble departure diameter and frequency, growth and time, nucleation site density. Then, experimental data was compared with theoretical correlations and used as input for three heat transfer coefficient models (RPI partitioning model, microlayer partitioning model and boundary layer turbulence model, which wil be further discussed in Section 3.7).

The experimental measurements of D_b for pure water and water-based silica and diamond nanofluids were found to be in good agreement with Kolev model [66], according to which D_b increases with wall superheat up to a certain point where the trend reverses due to the interaction between neighbouring bubbles causing early departure. Moreover, little difference was found in the measured D_b between water and nanofluids, while the measured f_b and N_a for nanofluids were considerably lower than water

at a given superheat. It was suggested that the reduction in the static contact angle upon nanofluids boiling creates a larger energy barrier for nucleation, which in turns decreases f_b and N_a. This was deemed to be the reason for lower boiling heat transfer coefficient of the tested nanofluids. Table 3.1 summarizes the observed trends in bubble parameters for water and the tested nanofluids.

	D_b	f_b	N_a	t_g	t_w
Nanofluids	High	Low	Low	High	High
Water	Low	High	High	Low	Low

Table 3.1: Bubble parameters comparison between water and nanofluids, reproduced from [35]

Subsequently, bubble dynamics of pool boiling of nanofluids has been investigated experimentally by other researchers. Hamda and Hamed [41] conducted a comparative study on the behavior of water-based alumina nanofluid with respect to pure water. When the nanofluid was boiled, it was observed that for the same heating area more nucleation sites were active, the bubbles were more spherical and $\sim 60\%$ smaller than in the case of pure water. Moreover, shorter bubble growth time was measured in the case of the tested nanofluid. As a consequence, the high departure frequency promoted surface rewetting, resulting in enhanced heat transfer.

Karimzadehkhouei et al. [53] analysed the effect of adding TiO_2 nanoparticles to water at varying mass fractions and applied heat fluxes. As illustrated in Figure 3.8, boiling of pure water is characterized by isolated bubbles, which then rise upwards and coalesce at increasing heat flux. Conversely, in the case of the nanofluids more nucleation sites are present, leading to the formation of vapour bubbles of smaller size and more regular shape. Bubble density increases with nanoparticle mass fraction, however this behaviour becomes less noticeable at the highest nanoparticle concentration due to the reduced transparency of the nanofluid.
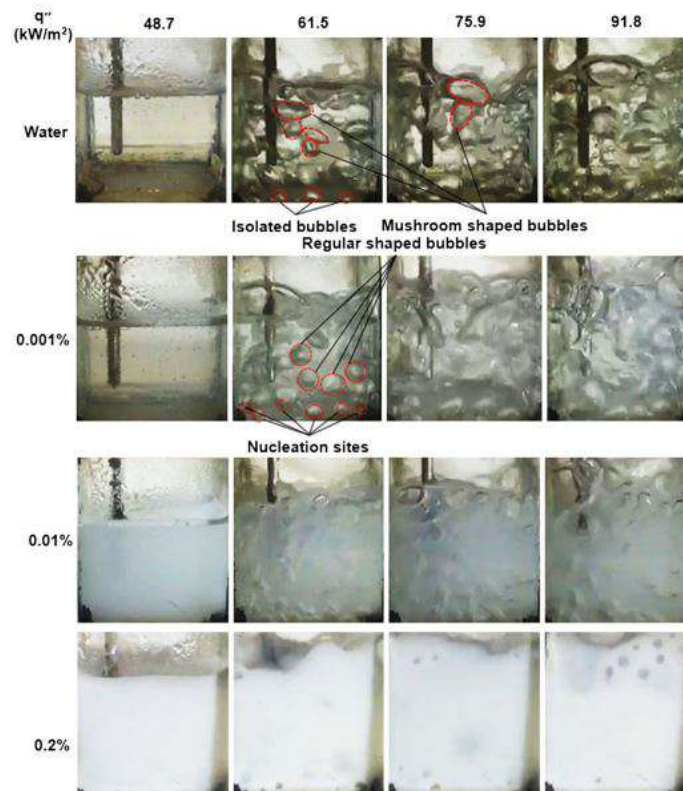
Figure 3.8: Visualization of pool boiling of water and water-TiO_2 nanofluid at different mass fractions and heat fluxes [53]

3.6.2. A model for nucleation site density with nanofluids

Ganapathy and Sajith [32] modified equation 2.20 introducing two parameters, namely the surface-particle interaction parameter ψ and the wettability parameter λ, in order to account for the effects induced by nanoparticles on surface roughness and wettability, respectively. Equation 3.1 gives the expression for ψ, while λ is defined as follows:

$$\lambda = \frac{1 - \cos\theta}{1 - \cos\theta^*} \tag{3.9}$$

where θ is the contact angle on the nanoparticle-deposited surface and θ^* is the contact angle on the original surface. Therefore, $\lambda = 1$ when fouling of the heating surface does not occur, $\lambda > 1$ when the fouled surface is characterized by lower wettability than the corresponding clean surface, otherwise $\lambda < 1$. Then, the final expression for N_a for nanofluid boiling is given by:

$$N_{a,nf} = 218.8 \frac{1}{\gamma} \Pr^3 \left(R_{nd,nf}\right)^{-0.4} \Delta T^3 \tag{3.10}$$

$$R_{nd,nf} = R_{nd} \cdot \lambda^a \cdot \psi^b \quad (a = 3, b = -0.5) \tag{3.11}$$

3.7. Nucleate pool boiling heat transfer models

An analytical approach to model pool boiling heat transfer with ordinary fluids was proposed by Benjamin and Balakrishnan [9]. Based on their work, Ganapathy and Sajith [32] have introduced modifications to extend the same model to pool boiling of nanofluids. In the original model it was assumed that the total heat removed by the boiling fluid is given by the sum of three contributions, namely the latent heat supplied by evaporation of the microlayer underneath a bubble (q_{me}), the heat required to recreate the thermal boundary layer by transient conduction (q_{tc}), and the heat transferred to the liquid region uninfluenced by the bubble cycle by turbulent natural convection (q_{nc}). The first term q_{me} represents the heat required to form the vapour bubbles and it is associated with the bubble growth time t_g expressed as function of bubble departure diameter $D_{b,d}$:

$$q_{me} = \frac{\gamma\phi\sqrt{\pi}}{10} B^2 Ar^{0.27} Ja \left(\alpha_l\right)^{3/2} \sqrt{t_g} \rho_l h_{fg} N_a \tag{3.12}$$

$$t_g = \left(\frac{D_{b,d}}{BAr^{0.135}\sqrt{Ja \cdot \alpha_l}}\right)^2 \tag{3.13}$$

$$D_{b,d} = 0.25 \sqrt{\left(\frac{\sigma}{g\left(\rho_l - \rho_v\right)}\right) \times \left[1 + \left(\frac{Ja}{\Pr_l}\right)^2 \left(\frac{1}{Ar}\right)\right]} \tag{3.14}$$

In the previous expressions γ is the surface-liquid interaction parameter whose definition is given by equation 2.21; ϕ is the ratio of the instantaneous bubble diameter to the instantaneous diameter of the dry area and it is considered to be a constant after the initiation of bubble growth ($\phi = 0.2$); B is a correlating factor having value of 1.55 for liquids with high density and high boiling point while the reciprocal of 1.55 is taken for low density and low boiling point liquids. N_a, Ja, Ar are the nucleation site density, Jakob number, and Archimedes number given by equation 2.19, 3.15, 3.16, respectively.

$$Ja = \frac{c_{p\,l}\rho_l\left(T_w - T_{sat}\right)}{h_{fg}\rho_g} \tag{3.15}$$

$$Ar = \left(\frac{g}{v_l^2}\right)\left(\frac{\sigma}{\rho_l g}\right)^{1.5} \tag{3.16}$$

The second term q_{tc} corresponds to the heating of the restored thermal boundary layer during the waiting period t_w, when cold liquid replenishes the volume previously occupied by the departed vapour

bubbles. The waiting time was estimated to be three times the growth time [120]. The process of thermal boundary layer reformation is modeled as transient conduction to a semi-infinite medium with temperature change $\Delta T = T_w - T_{sat}$:

$$q_{tc} = \frac{2k_l}{\sqrt{\pi \alpha_l t_w}} \left(N_a A_i \right) \Delta T \tag{3.17}$$

where A_i is the area of bubble influence. Indeed, after bubble departure, part of the superheated thermal boundary layer is carried within the wake of the bubble and this portion was found to be equal to four times the projected area of the bubble at departure [46]:

$$A_i = 4\frac{\pi D_{b,d}^2}{4} = \pi D_{b,d}^2 \tag{3.18}$$

Lastly, turbulent natural convection takes place in the area fraction A_{nc} which remains uninfluenced by the vapour bubbles:

$$A_{nc} = 1 - A_i N_a = 1 - \pi D_{b,d}^2 N_a \tag{3.19}$$

$$q_{nc} = \left(0.14\frac{k_l}{L}(Gr \cdot \mathrm{Pr})^{1/3} \right) \cdot A_{nc} \cdot \Delta T \tag{3.20}$$

where McAdams' correlation [82] was used to model the turbulent heat transfer coefficient and Gr is the Grashof number.

Finally, the total heat flux follows from a time-averaged sum of the previously described components:

$$q_{tot} = \frac{q_{me}t_g + q_{tc}t_w}{t_g + t_w} + q_{nc} \tag{3.21}$$

3.8. Relevant experimental findings

The following section contains an overview of experimental results regarding pool boiling performance using nanofluids. The observed trends in the HTC and CHF are discussed in view of their dependency on the various factors presented in the previous sections.

Up to now, experimental data reported by different researchers vary widely due to the differences in the experimental conditions, among which type of nanoparticles and base fluid, size and concentration of nanoparticles, nanofluid preparation method, heater geometry and heating surface characteristics, duration of the boiling process. In particular, the literature study was focused on water-based nanofluids since the same type of nanofluids will be analysed in the present thesis project.

One of the first studies on pool boiling with nanofluids was conducted by You et al.[130], who investigated boiling heat transfer using water-alumina nanofluid on a flat plate heater. They varied the concentration of Al_2O_3 particles from 0 $g/$ to 0.05 g/L and they observed that while the heat transfer coefficient was not significantly affected by adding such a small amount of nanoparticles, the CHF increased dramatically ($\sim 200\,\%$) when compared to the case of pure water (Figure 3.9). Moreover, Figure 3.10 shows that the relative enhancement of CHF due to the presence of nanoparticles increases with nanoparticle concentration up to 0.01 g/L and then it stays constant. Since the concentration leading to such a striking increase in CHF was very small compared to the required concentration to observe a significant change in the thermal conductivity, it was concluded that the effect of nanoparticles on mean thermophysical properties is not sufficient to explain the improved boiling performance of the tested nanofluids.
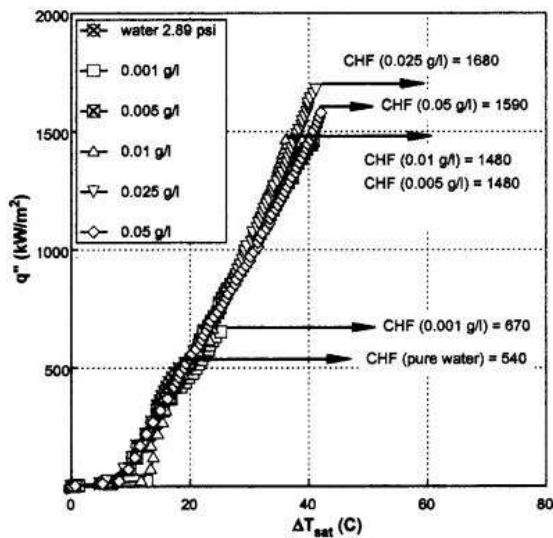
Figure 3.9: Boiling curve [130]
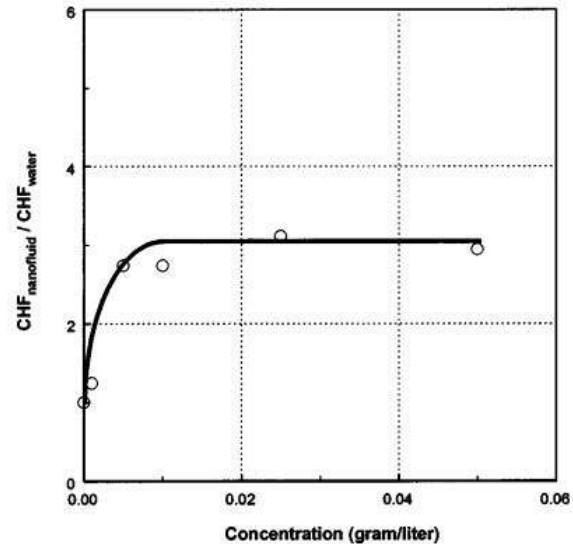
Figure 3.10: Relative enhancement of CHF [130]

Similarly, Kwark et al. [70] found that the CHF of different water-based nanofluids increased up to a critical nanoparticle concentration. Indeed, it was argued that CHF enhancement was the result of improved surface wettability and porosity, which could be increased by nanoparticle deposition only up to a certain limit. In fact, further nanoparticle deposition would lead to additional thermal resistance at the heating surface, having a detrimental impact on the boiling heat transfer coefficient. Therefore, it was found that an optimal concentration of 0.025 g/L yielded maximum CHF enhancement with no significant degradation in boiling heat transfer. Moreover, the optimal nanofluid concentration was independent of the nanoparticle type (diamond, Al_2O_3, CuO nanoparticles were tested).

In addition to this, the transient behaviour of the boiling process was investigated. By supplying constant heat flux during boiling experiments, it was observed that the wall superheat increased with time, thus indicating a progressive deterioration in heat transfer under continuous boiling conditions. Hence, it was suggested that the growth of the nanolayer with time was responsible for the reported trend. Conversely, CHF enhancement was independent on the duration of the boiling tests, confirming the hypothesis that the CHF enhancement of water-based nanofluids resulted from improved surface wettability.

The unsteady nature of nanofluid boiling was also studied by Ganapathy and Sajith [32]. Their experimental data proved that the progressive deterioration in boiling heat transfer observed in the case of water-alumina nanofluid was not present during the boiling of pure water. Moreover, boiling the basefluid on the nanoparticle-deposited heating surface was proposed as a solution to overcome the time-dependent heat transfer performance of the nanofluid while maintaining the favorable surface properties resulting from nanoparticles deposition. Indeed, the boiling performance of pure water on the nanoparticle-coated surface was found to be improved by 67%. Additionally, this process occurred at steady state, thus nano-structured surfaces were suggested as optimum for practical applications of pool boiling heat transfer.

A three-fold increase in CHF was also reported by Milanova and Kumar [84], who investigated the pool boiling process of silica nanofluids at 0.5% vol on a Nichrome heating wire. Various boiling conditions were tested (different particle sizes, concentrations, and pH of the solution). It was found that the smallest particle size (10 nm) yields the best CHF performance at high or low pH. Under such conditions, the maximum deposition was encountered on the heating wire, suggesting that the porosity due to silica deposition and oxidation of the Nichrome material play a key role in the enhancement of CHF.

However, experimental studies on pool boiling of water-alumina nanofluids performed by Das et al. [20] showed deterioration of boiling heat transfer with increasing particle concentration (range from 0.1% vol to 4% vol). Decrease in surface roughness due to the deposition of nanoparticles on the heating surface was deemed to be responsible for degradation in boiling phenomenon.

Bang and Chang [6] also conducted pool boiling experiments using water-alumina nanofluids on smooth surfaces at high particle concentration ($4 - 15\% \, wt$). Although the surface roughness was found to be increased by the deposition of nanoparticles, the boiling heat transfer coefficient was decreased because of the thermal resistance due to surface fouling.

The experimental analysis conducted by Yang and Liu [129] demonstrated that pool boiling heat transfer of nanofluids is governed by both the thermophysical properties of the working fluid and the surface characteristics. Indeed, they compared the behavior of a traditional water-silica nanofluid and a water-based functionalized nanofluid (i.e. silanes were grafted to SiO_2 nanoparticles to improve the long-term stability of the suspension). Indeed, while nanoparticle deposition occurs upon boiling of traditional nanofluids, such an effect is not observed when boiling functionalized nanofluids. Hence, it was possible to study separately the impact of thermophysical properties related to the intrinsic characteristics of the nanofluid and the surface characteristics on HTC and CHF. As far as the functionalized nanofluid is concerned, it was found that the boiling curve is shifted leftward with respect to pure water and the enhancement in HTC increases with nanoparticle concentration. Moreover, no substantial changes were observed in the CHF of the functionalized nanofluid compared to that of pure water. This suggests that HTC amelioration is due to bulk thermophysical properties variation resulting from the presence of suspended nanoparticles, while the absence of the deposition layer is responsible for unaltered CHF. Then, the traditional nanofluid was tested under the same experimental conditions and a completely different scenario was observed. Indeed, the HTC was found to be deteriorated and the CHF increased within $30.7\% - 38.5\%$. Indeed in the case of a traditional nanofluid, the HTC is affected by both thermophysical and surface properties, the latter of which having a predominant effect. The decrease in contact angle and suface roughness have a detrimental impact on boiling heat transfer, whereas the enhancement in wettability and porosity of the surface lead to higher CHF. Additionally, a boiling experiment of pure water on the traditional nanofluid-deposited surface was performed in order to assess the sole effect of the deposition layer. Figure 3.11 collects all the experimental data for pure water on the original and nanoparticle-fouled surface, traditional nanofluid on nanoparticle-depostied surface, and functionalized nanofluid. It must be noted that the CHF of water on the traditional nanofluid-boiled surface increases greatly compared to that of water on the clean surface, while the CHF on the nanoparticle-coated surface shows no significant change with the working fluid. This confirms that thermophysical properties variation has a weak effect on CHF, which is mainly affected by surface characteristics. Furthermore, since surface properties for pure water and functionalized nanofluid are essentially the same, the enhanced HTC of the latter results from the modified thermophysical properties.
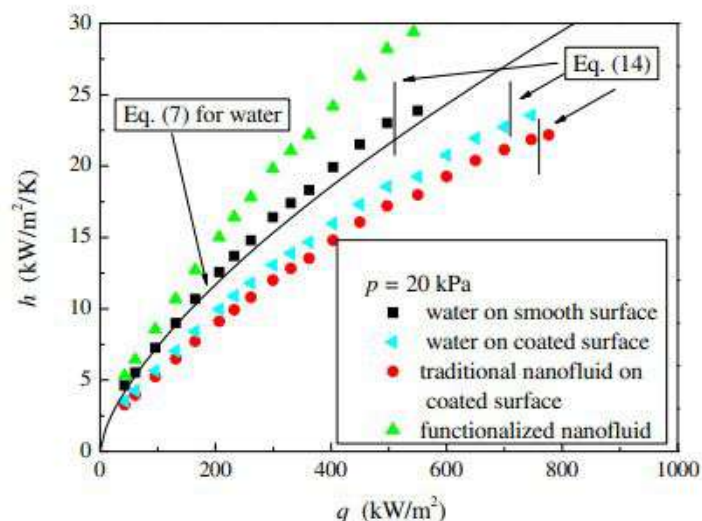
Figure 3.11: Effect of nanoparticle deposition on boiling heat transfer [129]
(The labels in the graph refer to equations used in the reference paper)

4
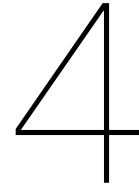
Experimental work

4.1. Methodology

The experimental work performed during this thesis project aimed at conducting multiple pool boiling tests using both a pure fluid (water) and a nanofluid (water-alumina $0.1\% \ wt$) to determine their heat transfer performance. In particular, obtaining the required data to plot the boiling curves was the primary objective enabling to quantify and compare the boiling heat transfer coefficient.

For each boiling surface, two tests were performed, first with water and then with the nanofluid. The surface topography was analysed by scanning electron microscopy (SEM) and white light interferometry (WLI) before and after boiling in order to gain insights on the effect of nanoparticles (i.e. deposition pattern and change in surface roughness parameters). The ultimate goal was to correlate the measured trend in heat transfer with surface properties in order to provide explanatory description of the behaviour of the nanofluid.

4.2. Requirements for the pool boiling setup

The design requirements for the test facility are as follows:

- The boiling surface should be removable in order to enable surface analysis after boiling. Moreover, the possibility to easily replace the surface allows to assess the effect of different surface conditions (i.e. material and microgeometry).

- The boiling vessel should be suitable for boiling of both pure fluids and nanofluids. In this respect, visual access to the boiling surface is crucial to observe the bubble dynamics.

- A condenser must be placed on the top of the fluid container to recirculate the vapour so that constant nanoparticle concentration may be assumed throughout the duration of the boiling experiment.

- Appropriate sealing between the boiling surface and the fluid container must be added to prevent any leakage from the boiling cell.

- Optimum contact between all the parts must be ensured by a proper clamping mechanism.

- The heating section and the test surface should be surrounded by insulation in order to minimize radial heat losses.

- The heat flux should be input to the boiling surface via a controllable power supply. Indeed, the current and the voltage must be adjusted in discrete steps to increase the heat flux gradually.

- The setup must include thermocouples at suitable locations to measure the working fluid bulk temperature and derive the boiling surface temperature.

- A data acquisition system must be connected to the boiling facility to collect the temperature readings.

Figure 4.1 shows the design concept of the pool boiling experimental equipment.
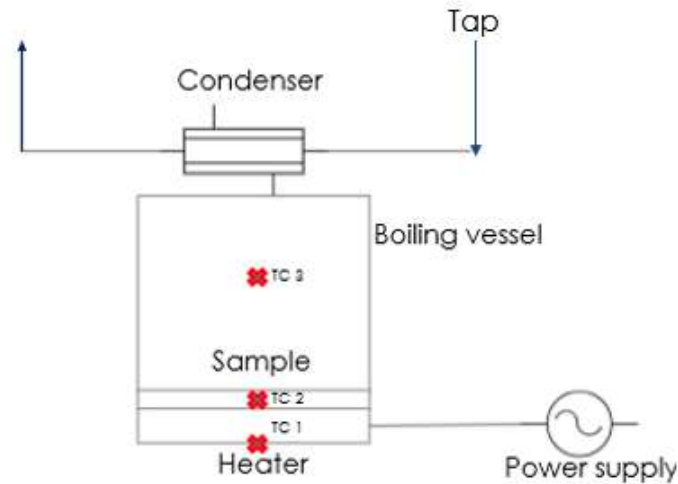
Figure 4.1: Schematic of the pool boiling apparatus

4.3. Experimental apparatus

In view of the previous considerations, the pool boiling test facility has been designed to include the following components:

- The boiling surface corresponds to the upper surface of an aluminium sample (aluminium 7075) having a Ø50 mm base and a Ø35 mm top surface, respectively. Moreover, the sample is machined so that it has a 1.5 mm groove, where an O-ring will be placed for sealing purposes.

- The boiling cell consists of a Ø35 mm borosilicate glass tube, which is sealed to the sample 1.5 mm below the boiling surface.

- Above the sample base a 7 mm thick PTFE sheet is placed to minimize heat losses to the surroundings. The PTFE plate includes six through holes where M4 bolts are placed to ensure proper contact between all the parts. Moreover, the downward force applied by the bolts counteracts the thermal stresses arising due to the heat supplied from the bottom, thus avoiding the bending of any component.

- Below the sample, a Ø50 mm resistive heating element (BACH Resistor Ceramics GmbH) is placed. The heater has a Ø1 mm through hole in the center, allowing for a thermocouple to pass through it.

- A T-type thermocouple (TC Direct) is immersed in the boiling fluid to measure its bulk temperature. An identical thermocouple is placed $\Delta = 4$ mm below the boiling surface. Thus, the surface temperature is given by the Fourier's law assuming that one-dimensional conduction occurs through the aluminium sample:

$$T_s = T_{tc} - q_s \frac{\Delta}{k_{Al}} \tag{4.1}$$

where T_{tc} is the temperature reading of the thermocouple, q_s is the input heat flux, and k_{Al} is the thermal conductivity of the material.

- Both the thermocouples are connected to an amplifier (Adafruit MAX31856 with cold junction compensation), which enables the signals to be read and displayed in Arduino. In particular, the compensation feature included in the amplifier prevents from misreadings due to changes in the reference temperature of the cold junction. Indeed, the functioning principle of a thermocouple is based on the Seebeck effect, which occurs when the two ends of a thermocouple are at different temperatures, resulting in electricity flowing from the hot to the cold junction. Thereby, an electromotive force is established and the potential difference is proportional to the temperature difference between the two ends. The governing equation reads as follows:

$$E_{emf} = S(T_{hot} - T_{cold}) \tag{4.2}$$

where E_{emf} is the voltage output given by the thermocouple, S is a material-dependent constant known as Seebeck coefficient, T_{hot} and T_{cold} are the temperature of the hot and cold junction, respectively.

Therefore, T_{cold} must be known in order to compute T_{hot}. This may be achieved by maintaining the cold junction in an isothermal ice bath, however cold junction compensation is a more practical method. An electronic circuit may be used to adjust the output voltage of the thermocouple to account for the voltage created by the cold junction which is not at $0°C$.

- The bottom part of the boiling facility is a vermiculite plate, which has the thermomechanical function of pressing the heater against the aluminium sample so that the applied heat flux is distributed homogeneously on the boiling surface. This material was selected due to its exceptional temperature resistance (up to $1000°C$) and thermal insulation properties ($k = 0.1 \ W/(m \ K)$).

- The heater is connected to a power supply (PSI 9200-15T, EA Elektro-Automatik GmbH), whose maximum output power, voltage and current are $P_{max} = 1000 \ W$, $U_{max} = 200 \ V$, and $I_{max} = 15 \ A$ respectively.

- The upper part of the boiling cell includes the cooling section, whose design is described in more detail in the next section.

The preliminary model of the pool boiling cell is depicted in Figure 4.2 and Figure 4.3 shows the complete experimental setup.

The technical drawings of the purchased components and the exploded view of the assembly are included in Appendix B.
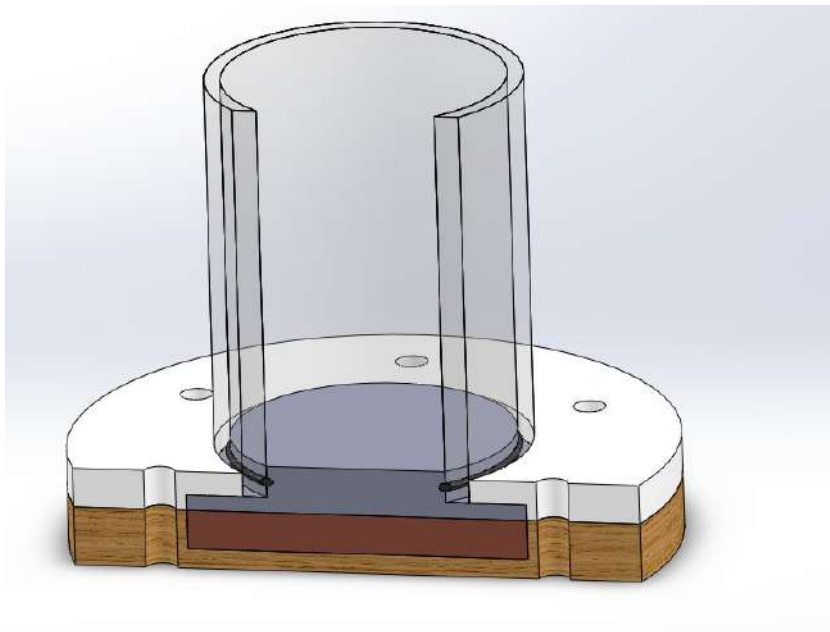
Figure 4.2: Preliminary model of the boiling cell (cooling section not shown)
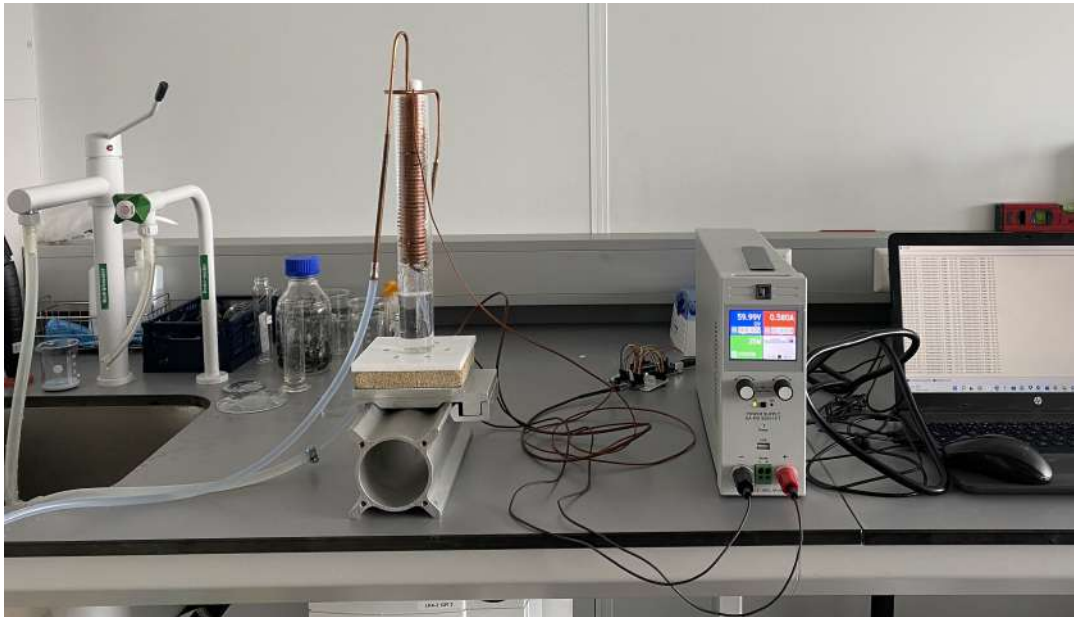
Figure 4.3: Experimental setup

4.3.1. Cooling section design

As cooling section, a cold finger was used. This is a compact version of a condenser consisting of a chamber where a cooling medium flows. As a consequence, the external walls of the cold finger are cooled, allowing for condensation of vapour when it reaches the localized cold surface. Indeed, vapour is generated when the tested fluid is boiled over the heated surface and it must be condensed back in order to prevent complete evaporation of the liquid. Therefore, a cold finger was chosen as a condensing device to be placed inside the boiling cell above the liquid level. The heat transfer mechanism by which vapour condenses on a vertical cooled wall and liquid drains off the surface under the action of gravity is referred to as *film condensation* [85]. In this condensation mode a thin liquid film wets the wall and as it flows down by gravity its thickness increases (Figure 4.4). If the condensate flow rate is small, the film surface may be considered to be smooth and the flow laminar.
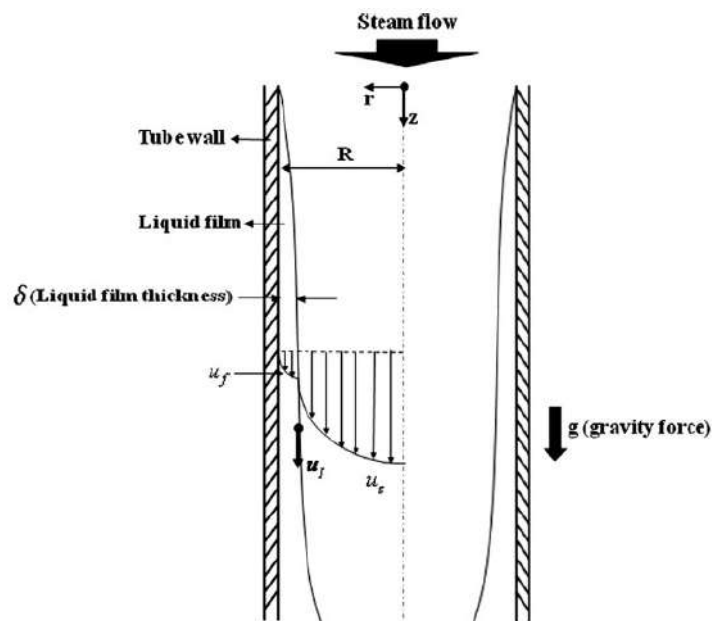
Figure 4.4: Film condensation in a vertical tube, reproduced from [56]

In the present setup a cold finger was made using a copper tube (2.8 mm i.d. 4 mm o.d.), thus obtaining a coil of internal diameter $D = 2.5\ cm$ and length $L = 20\ cm$. The inner part of the cold finger was closed from the top with a plastic foam to minimize vapour escape.

(a)   (b)

Figure 4.5: (a) Cold finger (b) Rolled plastic foam sheet to prevent vapour losses

In order to estimate the heat removed by condensation and the required flow rate through the cold finger, the correlations given by Mills [22] for film condensation were applied.
First, the liquid phase properties must be evaluated at the reference temperature T_r:

$$T_r = T_w + \alpha \left(T_{\text{sat}} - T_w \right) \tag{4.3}$$

where $\alpha = 0.33$ for water. Considering the case of water condensing at atmospheric pressure on a cold finger whose walls are at ambient temperature, the reference temperature was found to be: $T_r = 320\ K$. Then, the fluid properties are as follows: $\rho_l = 990\ kg/m^3$, $k_l = 0.64\ W/(m\ K)$, $\mu_l = 5.8 \times 10^{-4}\ Pa\ s$, $c_{p,l} = 4.18 \times 10^3\ J/(kg\ K)$, $h_{fg} = 2.39 \times 10^6\ J/kg$.

According to the Nusselt film condensation theory, the film thickness is given by the following equation:

$$\delta_{Nu} = \left[\frac{4\mu_l k_l z \left(T_{sat} - T_w \right)}{g h_{fg} \rho_l \left(\rho_l - \rho_g \right)} \right]^{1/4} \tag{4.4}$$

where z is the axial coordinate, as shown in Figure 4.4.
Then, the local heat transfer coefficient may be calculated as follows:

$$h(z) = \frac{k_l}{\delta(z)} \tag{4.5}$$

Integrating equation 4.5, the average heat transfer coefficient may be derived:

$$h = \frac{1}{L} \int_0^L h(z) dz = \frac{8^{\frac{1}{2}}}{3} \left[\frac{\rho_l \left(\rho_l - \rho_g \right) g h_{fg} k_l^3}{\mu_l (T_{sat} - T_w) L} \right]^{\frac{1}{4}} \tag{4.6}$$

In fact, the vapour becomes subcooled when it condenses on a cold wall. Therefore, Rohsenow [105] proposed a correction to the latent heat of vaporization to account for this effect:

$$h_{fg}' = h_{fg} + 0.68 c_{p,l} \left(T_{sat} - T_w \right) \tag{4.7}$$

Using equations 4.7 and 4.6, the average heat transfer coefficient is estimated to be $h = 4868\ \frac{W}{m^2\ {}^\circ C}$. Then, rearranging equation 4.5:

$$\delta_L = \frac{k_l}{h} = 1.3 \times 10^{-4} \ m = 0.13 \ mm \tag{4.8}$$

Moreover, temperature sensors were inserted into the inlet and outlet tube of the cold finger to calculate its cooling duty during the boiling experiments. Thus, by measuring the cooling water flow rate and the temperature difference across the cold finger, the condensation power is derived as follows:

$$\dot{Q}_c = \dot{m}_w \ c_{p \ w} (T_{w \ out} - T_{w \ in}) \tag{4.9}$$

Then, the difference between the power supplied by the heater and the power removed by the condenser gives an estimate of the heat lost by the system to the surroundings. These calculations are discussed in more detail in Section 5.5.

4.4. Experimental uncertainties

The measurement uncertainties for the present study were calculated using the method for single-sample experiments proposed by Kline and McClintock [65] and further developed by Moffat [87]. A more in-depth uncertainty analysis may be found in Appendix C.

4.5. Numerical simulations

A primary goal of the present setup is to ensure uniform surface heat flux with minimal radial heat losses. In order to evaluate the effect of the dimensions of the test sample on the heat flux distribution, a 2D simulation was performed using the software ANSYS Fluent 2019 R3. In particular, the objective was to study the pattern of isotherms and heat flux lines at different the sample thicknesses (t_1 and t_2 in Figure 4.6) and then select the optimal design solution for the sample. The only fixed dimensions were the top and bottom surface diameters (Ø35 mm and Ø50 mm respectively) and the total sample thickness, which was taken to be maximum 8 mm due to constraints dictated by the experimental apparatus (AFM and SEM). Considering the most extreme operating conditions (i.e. heater set at maximum power of 500 W), the maximum applied heat flux was calculated. Therefore, the boundary condition at the bottom surface is a constant heat flux of $q_s = 8.8 \times 10^6 \ W/m^2$. Moreover, at the top surface, where boiling takes place, a constant temperature of $T_s = 100°C$ was imposed as boundary condition and the sides, which are in contact with the insulation, were modelled as adiabatic. Quadrilateral face meshing was applied to the geometry to obtain orthogonal cells. As visualizing the temperature distribution along the side walls was a main goal, the mesh was refined at those locations by means of the edge sizing method.

Figure 4.6: 2D geometry for the numerical model

Figure 4.7 displays the temperature contours for different thicknesses: t_1 and t_2 were varied from 3 mm to 6 mm and from 5 mm to 2 mm, respectively. It should be noted that a sample with small t_1 is characterized by localized heating at the sides, where the temperature reaches 194°C, while the central body experiences a much smaller temperature gradient. By gradually increasing t_1, it can be seen that only the corners in correspondence of the bottom surface are at the maximum temperature,

whereas the temperature decreases progressively from the sides towards the centerline.

Table 4.1 shows the temperatures at the lowest corner $T_{l,c}$, mid corner $T_{m,c}$ and at the center of the base $T_{c,b}$ for the various geometries. Furthermore, $\Delta T_s/\Delta x_s$ indicates the temperature gradient between the bottom and the mid corner, while $\Delta T_c/\Delta x_c$ denotes the temperature gradient along the centerline. Finally, the last column R contains the ratio between the two gradients (i.e. the fraction of heat which is conducted to the sides).

It may be concluded that the last configuration correspond to the case when the heat flux is more uniformly distributed as localized heating at the bottom corners is less pronounced and shape of the temperature contours shows that the temperature gradient across the central part of the sample is more moderate. Indeed, this is confirmed by the fact that $\Delta T_c/\Delta x_c$ reaches a minimum in this case. However, a sample with $t_2 = 2\ mm$ would not be feasible as it would not allow for machining of a groove, which is essential to place the O-ring. For this purpose, t_2 should be at least $4\ mm$. In particular, a sample with $t_1 = 4\ mm$ and $t_2 = 4\ mm$ would be the optimal solution, being characterized by the smallest values of $\Delta T_s/\Delta x_s$ and R. This signifies that in this configuration the amount of applied heat flux which is conducted to the sides with respect to the heat which is conducted along the central body of the sample reaches a minimum.

(a) $t_1 = 3\ mm\ t_2 = 5\ mm$

(b) $t_1 = 4\ mm\ t_2 = 4\ mm$

(c) $t_1 = 5\ mm\ t_2 = 3\ mm$

(d) $t_1 = 6\ mm\ t_2 = 2\ mm$
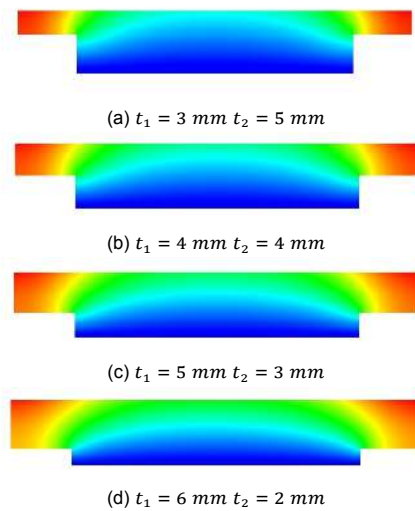
Figure 4.7: Isotherms at different t_1 and t_2

Thickness	$T_{l,c}$ [°C]	$T_{m,c}$ [°C]	$T_{c,b}$ [°C]	$\Delta T_s/\Delta x_s$ [°C/mm]	$\Delta T_c/\Delta x_c$ [°C/mm]	R
t_1=3 mm t_2=5 mm	194	188	132	2.00	4.00	0.50
t_1=4 mm t_2=4 mm	179	172	130	1.75	3.75	0.47
t_1=5 mm t_2=3 mm	169	160	129	1.80	3.63	0.49
t_1=6 mm t_2=2 mm	156	145	127	1.83	3.38	0.54

Table 4.1: Thermal analysis of the aluminium sample varying t_1 and t_2

Moreover, taking the optimal $t_1 = 6\ mm$ as a fixed variable, the effect of increasing t_2 was studied. It was found that a thicker sample would have localized hot zones in the lateral parts as the distance between the top surface, which is at the lowest temperature, and the heated base is increased (Figure 4.8). Indeed, the further the top surface at imposed temperature is located, the lesser it influences the temperature distribution across a thicker sample.

(a) $t_1 = 6 \, mm \; t_2 = 2 \, mm$

(b) $t_1 = 6 \, mm \; t_2 = 3 \, mm$

(c) $t_1 = 6 \, mm \; t_2 = 4 \, mm$
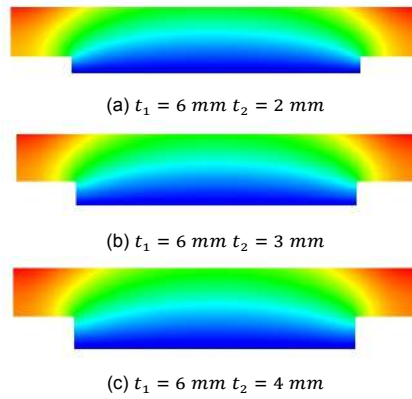
Figure 4.8: Effect of varying t_2

In view of the previous considerations, the chosen dimensions for the aluminium samples were $t_1 = 4 \, mm$ and $t_2 = 4 \, mm$.

4.6. Nanofluid preparation

In the present study a water-alumina $0.1\% \, wt$ nanofluid was tested. It was synthesised using alumina boehmite (DISPAL 14N80) produced by Sasol. The trademark DISPAL refers to the high dispersibility and purity of these powders, which are specifically intended for colloidal applications. The boehmites are versatile as they can be dispersed in both polar and non-polar media up to $40\% \, wt$ concentration. As a final step, the nanofluid was sonicated for 30 minutes before each boiling test to ensure its stability.

4.7. Nanofluid characterization

The Zetasizer Nano instrument (Malvern) was used to measure the particle size distribution and Zeta potential ζ. The former is calculated by applying the dynamic light scattering technique (DLS), which measures the Brownian motion of nanoparticles by illuminating them with a laser beam and analysing the resulting intensity fluctuations in the scattered light. The latter is a quantitative measure of the stability of a nanofluid, which is a key requirement for nanofluids to be defined as colloidal suspensions. Indeed, if agglomeration or sedimentation occur the homogeneity of the suspension is lost, thereby altering uniformity of the properties of the nanofluid.

Figure 4.9 shows the alumina nanoparticles size distribution given by the Zetasizer. The instrument yielded an average diameter of $D_p = 115 \, nm$, which is in good agreement with the specifications provided by the supplier (average nanoparticle size of $120 \, nm$).
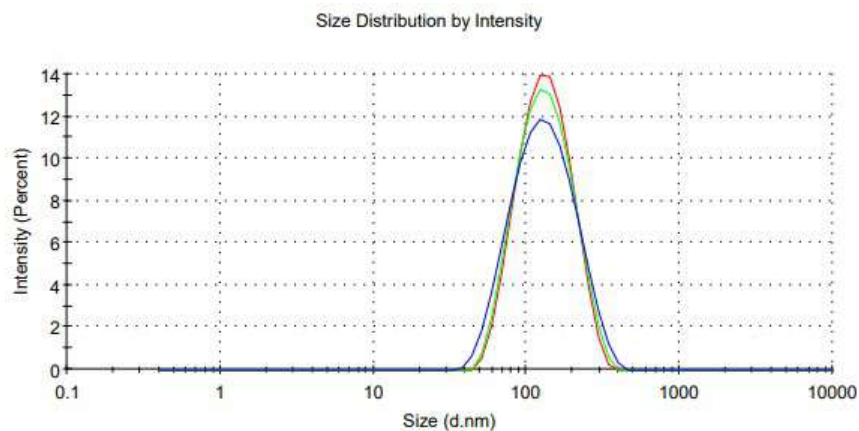
Figure 4.9: Alumina nanoparticles size distribution in water-based $0.1\% \, wt$ nanofluid

According to the Zeta potential theory [118], large absolute values of ζ signify that the particles in suspension tend to repel each other so flocculation is prevented. Colloids are normally considered to be stable if $|\zeta| > 30mV$. Figure 4.10 shows the Zeta potential distribution of the alumina-based nanofluid used in the present study. The Zeta potential was found to be $\zeta = 46\ mV$, thus confirming the stability of the nanofluid.
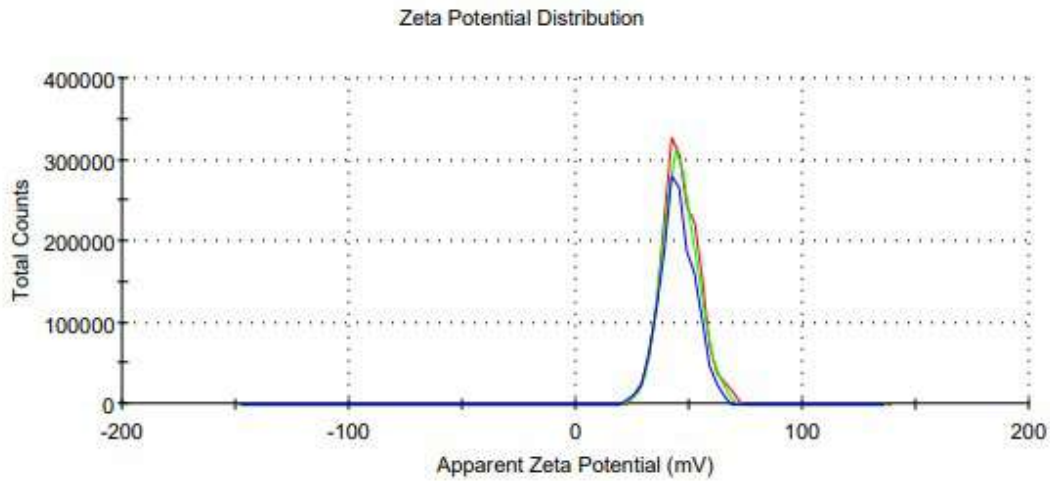
Figure 4.10: Zeta potential of water-based $0.1\%\ wt$ nanofluid

Further details concerning the fundamental principles of the DLS technique and the Zeta potential analysis may be found in Appendix A.

5

Results and analysis

5.1. Validation of the boiling setup

First, a benchmark test was performed with pure water in order to assess the reliability of the pool boiling apparatus. During the experiments, the power was regulated increasing the voltage by $10\ V$ at each step. Temperature readings were collected every second and at thermal equilibrium temperature variations were of the order of $0.1\ °C$. Steady state was maintained for 10 minutes before increasing the power to the next level.

Moreover, vapour escape was prevented by closing the inner part of the cold finger from the top with a rolled plastic foam sheet. This allowed to operate at atmospheric pressure while minimizing the amount of fluid lost by evaporation, as only a small gap between the condenser and the glass walls was left. To confirm this assumption, the liquid level was monitored during the experiments and the variations at the end of the boiling run were in the range of $2-4$ %.

5.1.1. Comparison with pool boiling models

The pool boiling curves obtained experimentally for increasing and decreasing imposed heat flux were compared with the pool boiling curves given by three different models, namely the Rohsenow correlation, the Mostinski correlation, and the Gorenflo correlation (Figure 5.1). Indeed, three types of methods have emerged in the literature for predicting pool boiling heat transfer: based on physical properties or reduced pressure of the working medium, and fluid-specific.

As outlined in Chapter 2, the Rohsenow equation (equation 2.1) includes several thermophysical properties and empirical constants, hence it belongs to the first category. In particular, the values of the constants C_{sf} and n depend on the fluid-surface coupling as well as the surface material and finishing. For water on an aluminium oxidized surface [96], $C_{sf} = 0.011$ and $n = 1.26$ (errors in ΔT of about 25 % are expected to be found [75]).

In the Mostinski correlation the nucleate boiling heat transfer coefficient is given as function of the critical pressure p_c and reduced pressure p_r of the working fluid at its boiling temperature:

$$h_{\mathrm{M}} = 0.00417 q^{0.7} p_{\mathrm{c}}^{0.69} F_{\mathrm{PF,M}} \tag{5.1}$$

where

$$F_{\mathrm{PF,M}} = 1.8 p_{\mathrm{r}}^{0.17} + 4 p_{\mathrm{r}}^{1.2} + 10 p_{\mathrm{r}}^{10} \tag{5.2}$$

Gorenflo developed a fluid-specific, reduced pressure-based correlation, which also takes into account the effect of surface roughness, denoted as R_p. Furthermore, the Gorenflo correlation uses a

reference heat transfer coefficient h_0, which is calculated at the following conditions: reduced pressure $p_{r0} = 0.1$, heat transfer coeffcient $q_0 = 20000 \ W/m^2$, surface roughness $R_{p0} = 0.4 \ \mu m$. In the case of water, $h_0 = 5600 \ W/(m^2 \ {}^\circ C)$, as reported by the VDI Heat Atlas [37]. Finally, the boiling heat transfer coefficient of water is given by:

$$h_G = h_0 F_{\text{PF,G}} \left(\frac{q}{q_0} \right)^{nf} \left(\frac{R_{\text{p}}}{R_{\text{p0}}} \right)^{0.133} \tag{5.3}$$

where

$$F_{\text{PF,G}} = 1.73 p_{\text{r}}^{0.27} + \left(61 + \frac{0.68}{1 - p_{\text{r}}} \right) p_{\text{r}}^2 \tag{5.4}$$

and

$$nf = 0.9 - 0.3 p_{\text{r}}^{0.15} \tag{5.5}$$

As shown in Figure 5.1, the experimental data points differ from the trend predicted by the aforementioned models by more than the expected 25%. Indeed, the average deviations between the experimental data and the three models (Rohsenow, Mostinski and Gorenflo) are 41%, 27%, and 22% respectively. However, at higher wall superheats (i.e. considering the last four points in the plot) errors as large as 71%, 48%, and 28% are found. The Gorenflo correlation, which is fluid-specific and includes the effect of surface roughness, is the closest to the experimental results but still overpredicts the slope of the boiling curve.
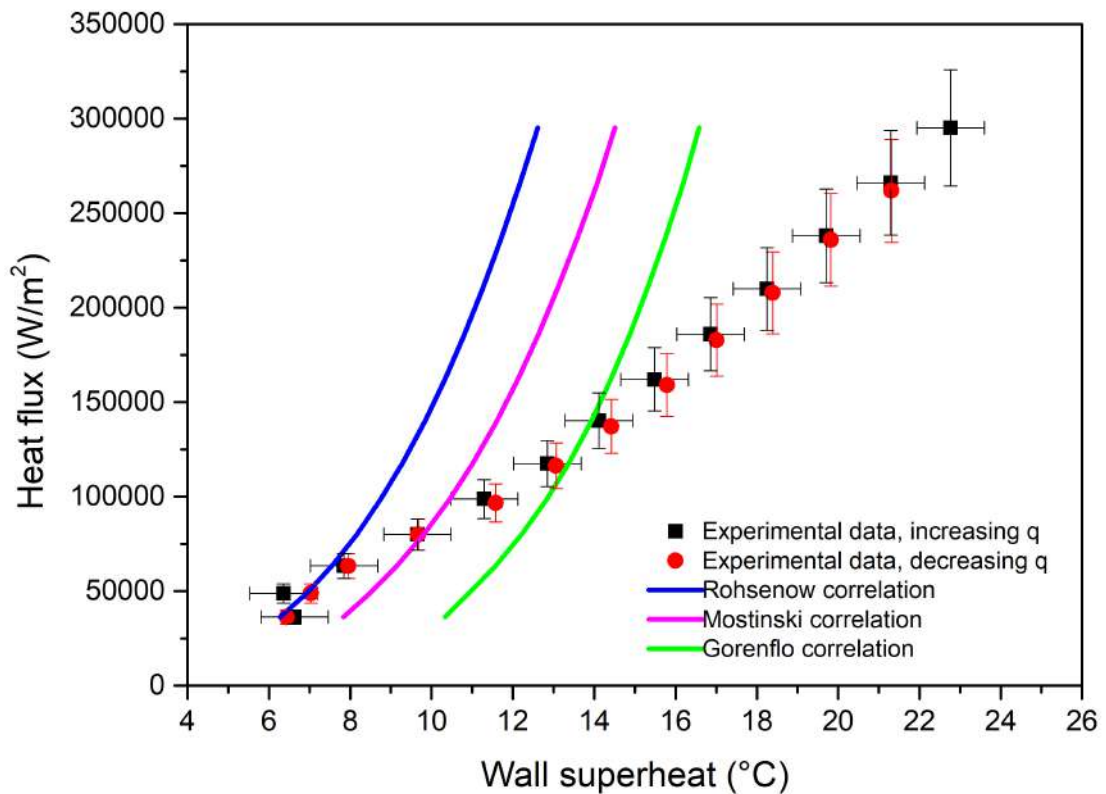
Figure 5.1: Pool boiling curve: experimental vs theoretical correlations

5.1.2. Comparison with reference experimental work

As a next step, the experimental work by Karimzadehkhouei at al.[53] was taken as reference to validate the results of the present research. Indeed, the aforementioned study reported the pool boiling curve of water at atmospheric pressure on an aluminium surface, using a similar setup and method to perform the experiments. As illustrated in Figure 5.2, a good agreement between their experimental results and the current ones was found (note that the heat flux range tested by Karimzadehkhouei at al.[53] was limited from $48.7\ kW/m^2$ to $134.9\ kW/m^2$).
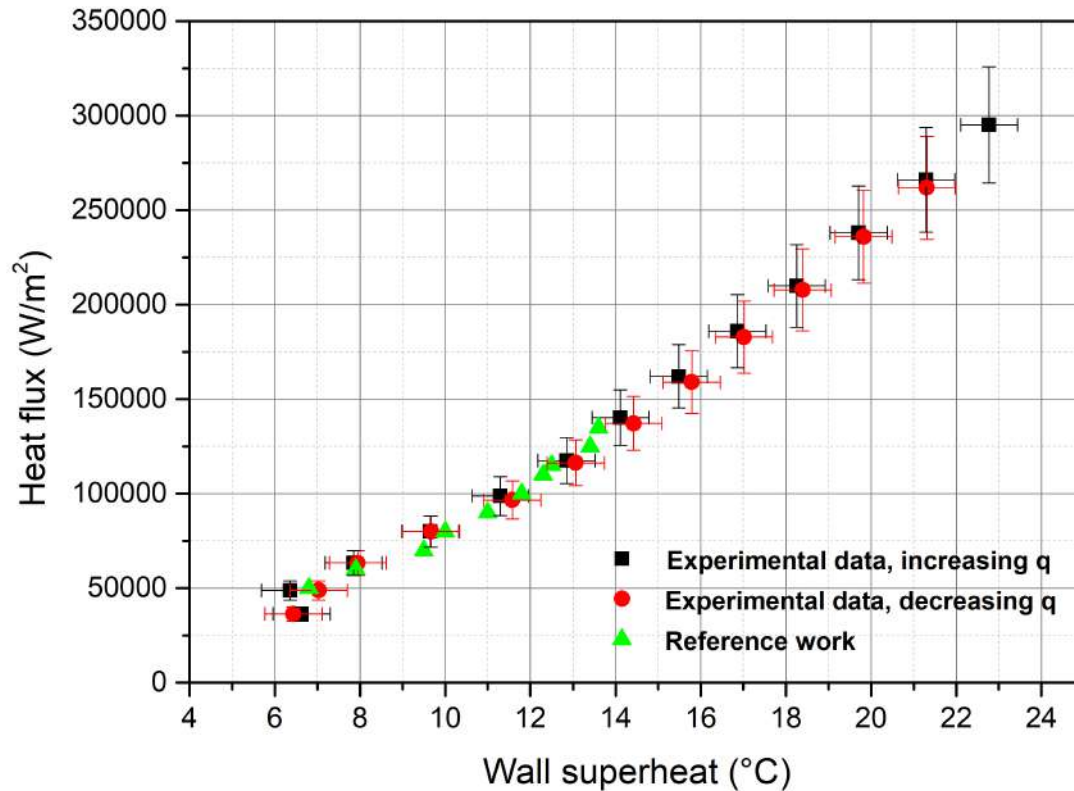
Figure 5.2: Pool boiling curve: experimental vs reference work [53]

5.2. Hysteresis effects

Pool boiling experiments were performed for both ascending and descending imposed heat flux in order to assess any hysteresis effect. As mentioned in Chapter 2, the pool boiling curve is typically characterized by the so-called *nucleation hysteresis* or *temperature overshoot* (TOS), which occurs at boiling incipience. Indeed, when the boiling curve transitions from natural convection to nucleate boiling, the first vapour bubbles are generated at just a few spots on the surface, where there is only a small amount of residual non-condensable gas. As a consequence, according to the thermodynamic nucleation theory, the superheat required for the first embryonic bubbles to grow is large (this is represented by the first black data point in Figure 5.3). After the departure of these bubbles, more vapour is trapped in the surface cavities (this is the so-called *vapour gathering* [86]) hence the wall superheat for further bubble generation decreases, as shown by the second black data point in Figure 5.3, which is shifted to the left.

Moreover, boiling hysteresis in the developed region may be observed when the boiling curve follows different trajectories for increasing and decreasing heat fluxes. The type of hysteresis in which the boiling curve for decreasing heat flux is shifted leftwards, thus yielding improved heat transfer performance, is referred to as II-kind hysteresis [101]. In this type of hysteresis, when the heat flux is reduced before reaching the CHF, the nucleation sites remain active enabling the applied heat flux to be dissipated at lower wall superheats, as shown by the red data points in Figure 5.3.

It should be noted that the phenomena of temperature overshoot and II-kind hysteresis were present in all the boiling tests. In particular, Figure 5.3 refers to the boiling of water on sample 5, in which case the temperature overshoot was found to be about $2\,°C$.
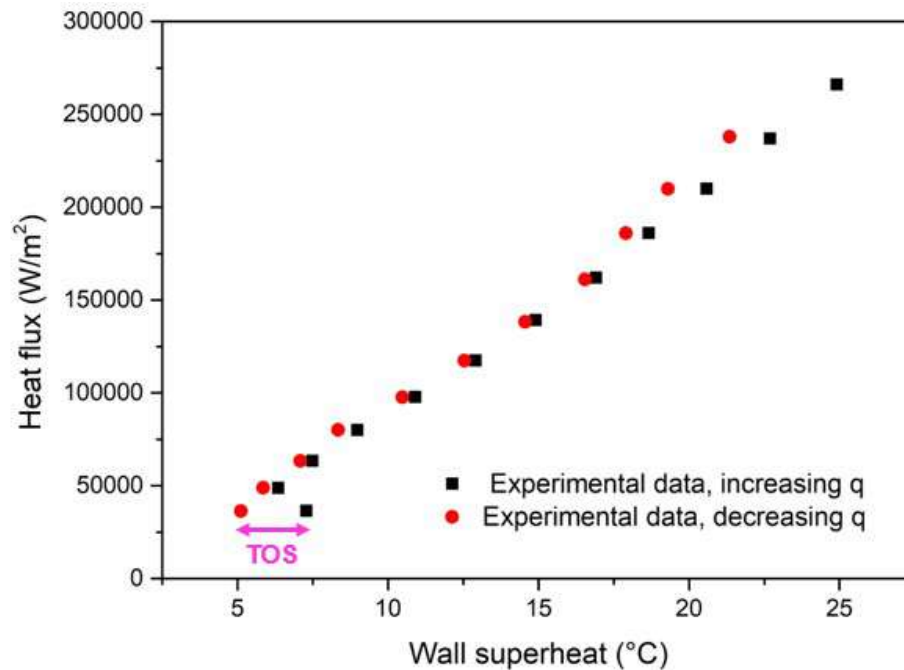
Figure 5.3: Nucleation hysteresis in pool boiling of water

5.3. Experimental procedure

The boiling experiments and related characterization of the tested surfaces aimed at investigating the differences caused by the presence of nanoparticles with respect to the base fluid. Six aluminium samples were used in the present study in order to examine the reproducibility of the results.

The following steps were taken on each sample to conduct the comparative analysis between pool boiling of water and water-alumina $0.1\,\%\,wt$ nanofluid:

   – Analysis of the base surface prior to boiling using SEM and WLI;

   – Boiling of water (6 h);

   – Boiling of the nanofluid (6 h);

   – Analysis of the nanoparticles deposited surface after boiling using SEM and WLI.

In particular, the workflow during each boiling run was as follow:

• The working fluid was preheated in a separate beaker on a plate heater;

- The aluminium sample was cleaned with acetone and dried in air;

- The O-ring was inserted into the groove;

- The boiling cell was assembled, starting from the bottom: insertion of the thermocouple, placement of the heater and the aluminium sample into the vermiculite plate (Figure 5.4a);

- The Teflon insulation was positioned on top of the sample and the bolts were tightened, after having verified that proper contact between the parts was achieved (Figure 5.4b);

- The glass tube was pressed from the top to ensure good sealing by means of the O-ring;

- The cold finger was placed inside the glass tube;

- The working fluid was poured inside the boiling cell;

- The cold finger was closed from the top with a plastic foam sheet (Figure 5.4c);

- At the end of the experiment, the liquid was poured out and the condenser was removed;

- The setup was disassembled;

- The excess liquid was dabbed with a tissue from the sample surface without scratching it;

- Finally, the sample was prepared for further analysis (SEM and WLI).

(a)

(b)

(c)
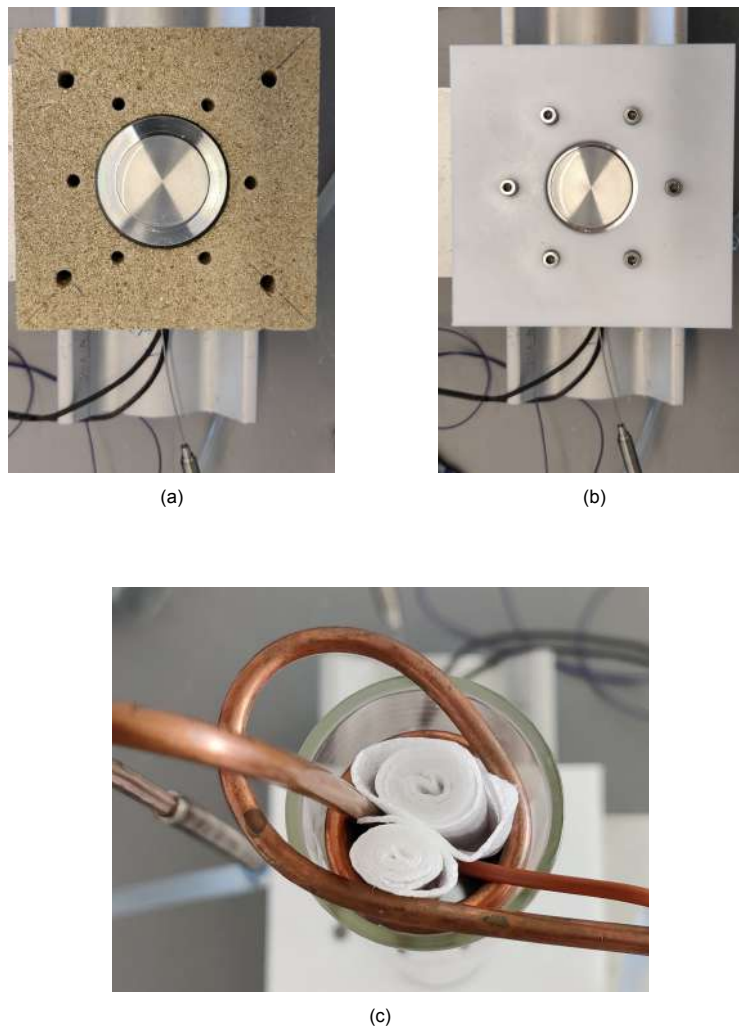
Figure 5.4: Details of the assembly procedure: (a) insertion of the heater and the sample into the vermiculite plate; (b) placement of the Teflon insulation and tightening of the bolts; (c) closing the cold finger from the top.

<div align="center">(a)   (b)</div>
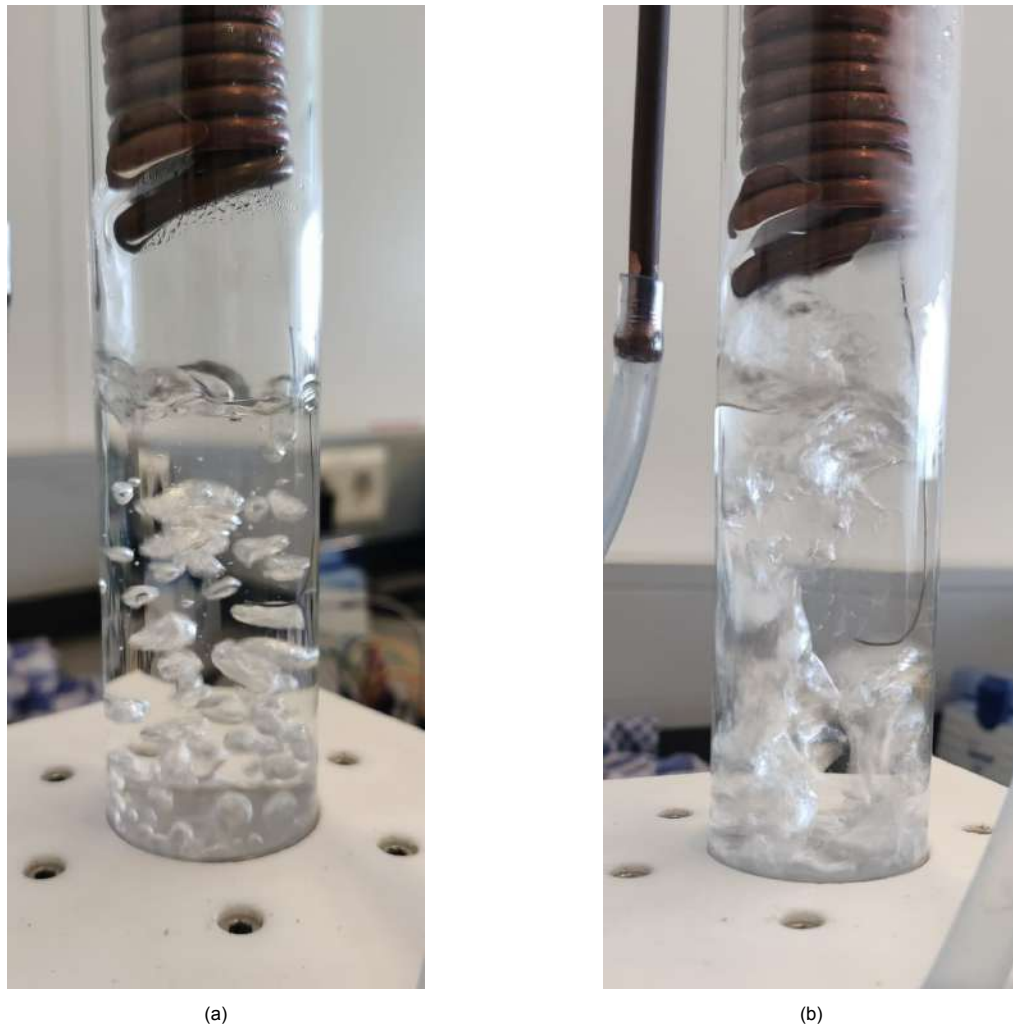
Figure 5.5: Bubble dynamics: (a) boiling incipience and (b) vigorous boiling

5.4. Pool boiling curves comparison

Figure 5.6 shows the pool boiling curves of water on six aluminium samples, which were manufactured using the same material and machining tools. Differences in the Ra among the samples were found to be of the order of $0.2 \ \mu m$. Therefore, the fact that the boiling surfaces are not fully identical might be the reason why the respective boiling curves do not overlap each other exactly. In particular, the maximum average deviation, which is found between the pool boiling curves on sample 3 and 6, is about 38%. Figure 5.7 shows the pool boiling curves of the water-alumina $0.1 \ \% \ wt$ nanofluid. It is apparent that the performance of the nanofluid is not consistent. The boiling tests on samples 1, 3 and 4 led to very similar curves, however the curves related to sample 5 and 2 are shifted to the right by 37% and 62%, respectively. The most extreme case is represented by the boiling run on sample 6, which deviates by more than 100% from sample 1.
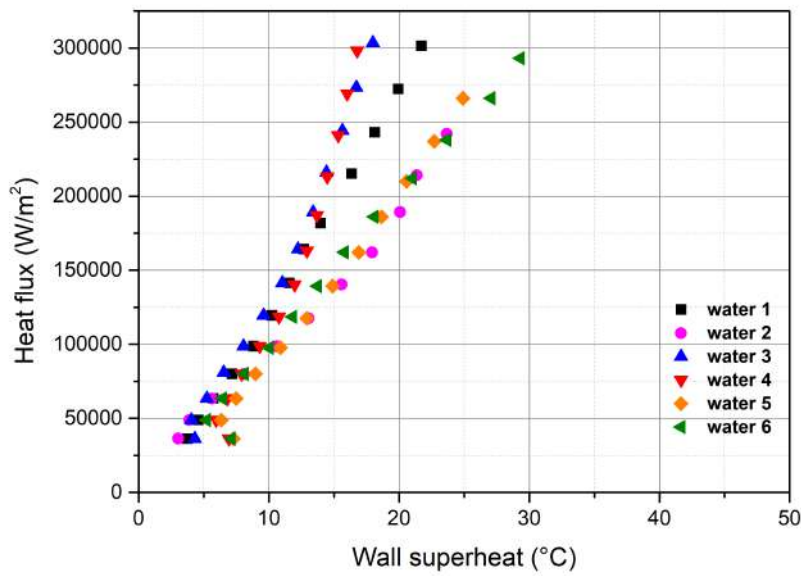
Figure 5.6: Pool boiling curves of water on the tested samples
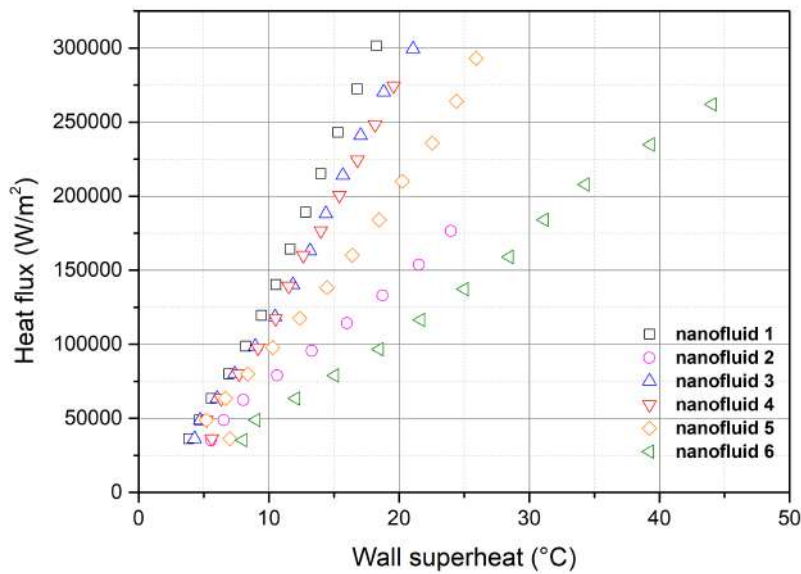
Figure 5.7: Pool boiling curves of water-alumina 0.1 % wt nanofluid on the tested samples

Figure 5.8 summarizes the pool boiling data collected performing the experiments on six different samples (solid symbols are used for water and open symbols for the nanofluid). It should be noted that the curves for samples 1, 3, and 4 show good consistency. A maximum deviation of 19% was found between water and nanofluid on sample 1 at the highest heat flux, where the nanofluid exhibited enhanced performance. Conversely, on samples 3 and 4 the nanofluid had lower boiling heat transfer coefficient than water, by 10% and 21% at the highest heat flux, respectively. Regarding sample 5, the curves of water and the nanofluid are almost matching each other but they are shifted to the right when compared to the other samples. Finally, it is evident that the boiling curves of the nanofluid on samples

2 and 6 are significantly shifted to the right, thus indicating decreased heat transfer performance. These outliers might be attributed to either a misplacement of the thermocouple inside the aluminium sample, thus leading to erroneous readings, or to some differences in the original surface texture of these samples.

Note that Figure 5.8 does not display the error bars for better graphic rendering of the plot; however, the data and the corresponding uncertainties for all the boiling runs are included in Appendix C.
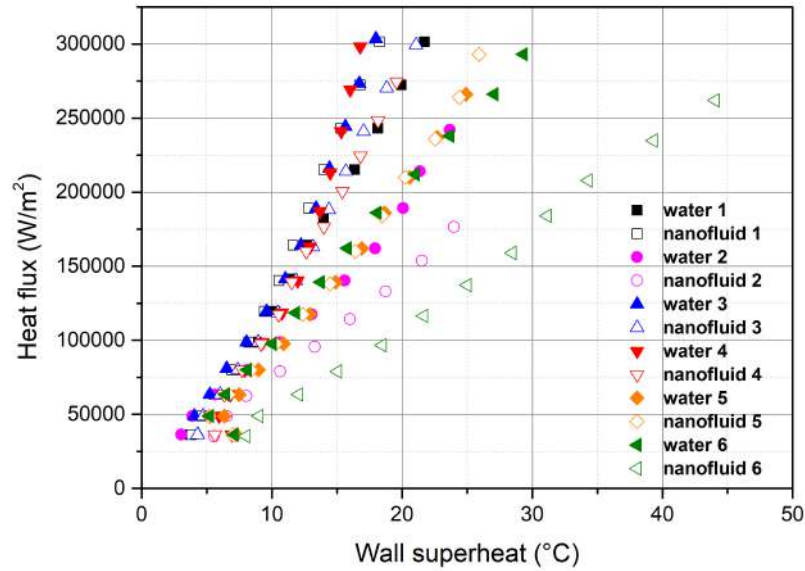
Figure 5.8: Pool boiling curves of water and water-alumina $0.1 \% \, wt$ nanofluid on the tested samples

5.5. Heat losses

As mentioned in Section 4.3.1, the heat losses to the surroundings may be estimated by calculating the difference between the power supplied by the heater, which causes the fluid to boil, and the power removed by the condenser.

First, knowing the cooling water flow rate and the temperature difference across the cold finger at each power step, the condensation power is derived as follows:

$$\dot{Q}_c = \dot{m}_w \, c_{p \, w}(T_{w \, out} - T_{w \, in}) \tag{5.6}$$

The system heat losses during a boiling run are shown in Table 5.1. It should be noted that the heat losses are on average about 30% of the power input, but they vary during the boiling process. The main reasons for that are the limited accuracy in the readings of the temperature sensors (the uncertainty in $T_{w \, out}$ and $T_{w \, in}$ is $\pm 1°C$) and the fact that $\dot{m}_w$ is measured only once at the beginning of the test (in fact, the mass flow rate is not constant during the boiling run as the tap water pressure changes). Nonetheless, the order of magnitude of the heat losses matches with those predicted theoretically. Indeed, the heat lost by the glass tube ($D_t = 40 \, mm$, $L_t = 30 \, cm$) by natural convection and radiation may be calculated as follows:

$$\dot{Q}_{lost} = \pi \, D_t \, L_t \, h_c \, \Delta T \simeq 45 \, W \tag{5.7}$$

where a heat transfer coefficient of $h_c = 15 \, W/(m^2 \, °C)$ may be assumed to take into account the combined effect of natural convection and radiation [85, Ch. 2, p. 69]. Moreover, a temperature difference of $\Delta T = 80 \, °C$ between the glass walls and the ambient air was considered.

Insulating the glass tube would have allowed to reduce heat losses, but it would have made impossible to observe the boiling dynamics.

$\mathbf{P_{heater}}$ $[W]$	$\mathbf{P_{condenser}}$ $[W]$	$\mathbf{P_{lost}}$ $[W]$	$\mathbf{Losses}$ $[\%]$
34	22	12	35
47	23	24	51
61	41	20	33
76	49	27	35
93	74	19	20
112	64	48	43
132	84	48	36
153	105	48	31
177	117	60	34
200	150	50	25
226	182	44	20
252	199	53	21

Table 5.1: Heat losses (the data displayed refer to pool boiling of water on sample 6)

5.6. Surface analysis

This section includes the pictures given by SEM and WLI for the tested samples. Since these images highlight the differences between the base surface (before the boiling process) and the nanoparticles depositions (after boiling on the six samples was performed), they will be used as reference for further discussion in section 5.6.8.

5.6.1. Base surface

The aluminium samples were made with a lathe machine, hence the surface topography resulting from turning is characterized by concentric circles (Figure 5.9a). These features create a micro-roughness pattern (Figure 5.9c).
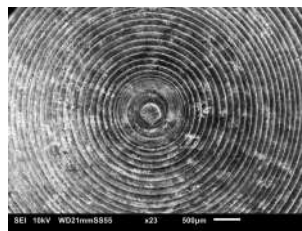
(a)
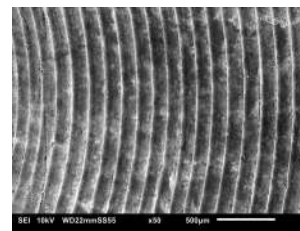
(b)
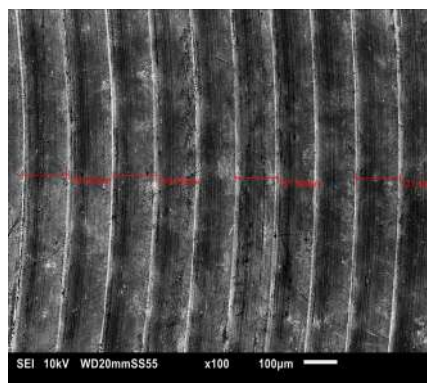
(c)

Figure 5.9: SEM images of the base surface at increasing magnification

The same surface profile was detected by WLI as well, with additional information regarding the height of peaks and valleys, as shown in the 3D maps reconstructed at various locations (Figure 5.10).

(a)

(b)

(c)
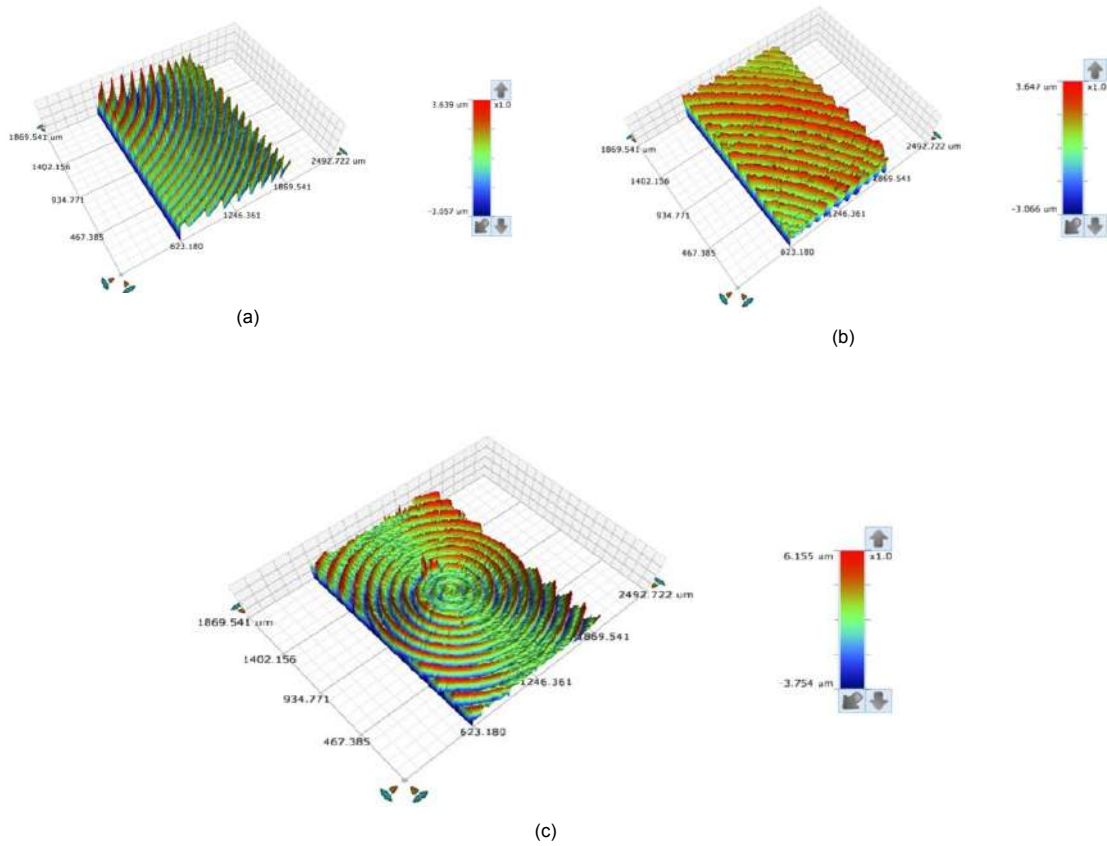
Figure 5.10: WLI images of the base surface at different locations

5.6.2. Sample 1 surface analysis

(a)

(b)
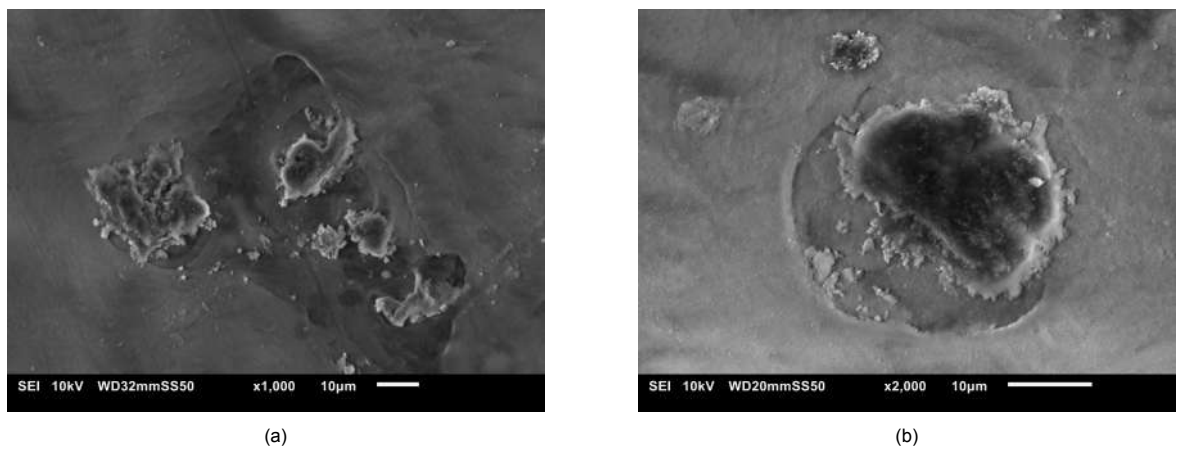
Figure 5.11: SEM images of the nanoparticles deposited on sample 1 at (a) x1000 and (b) x2000 magnification

(a)

(b)

(c)
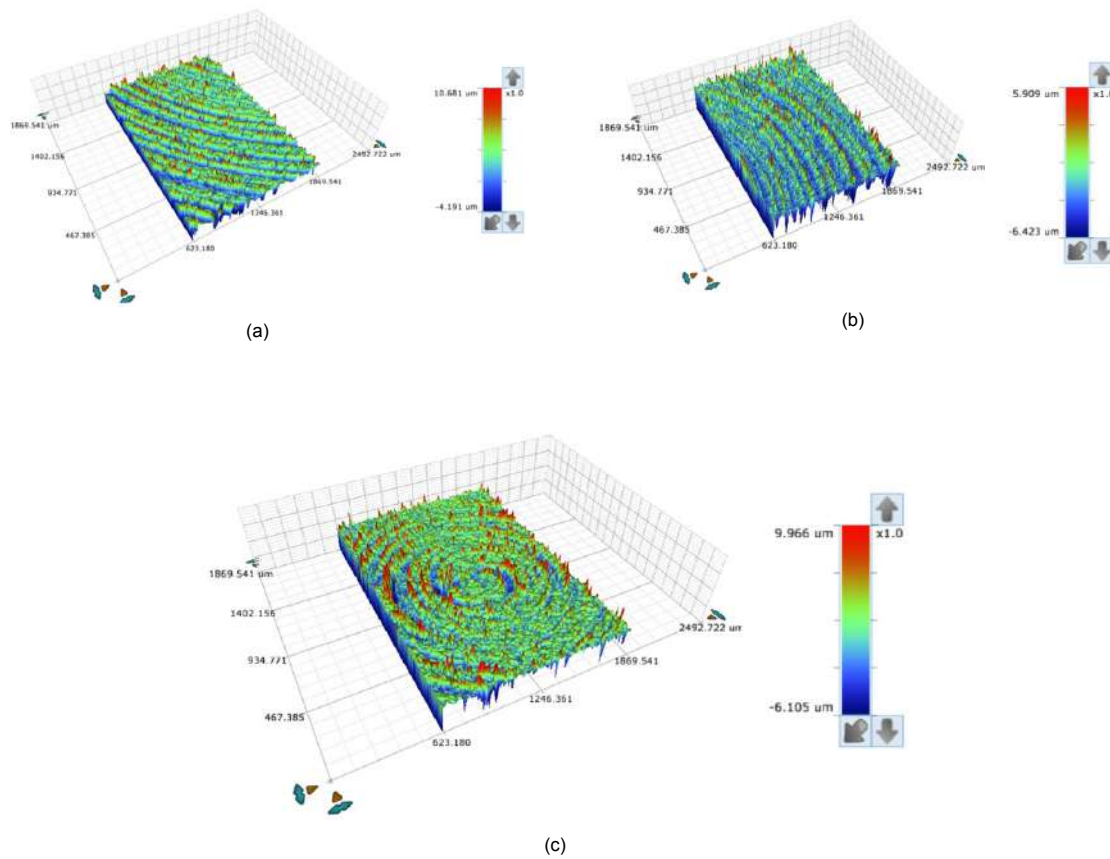
Figure 5.12: WLI images of sample 1 surface at different locations

5.6.3. Sample 2 surface analysis

(a)

(b)
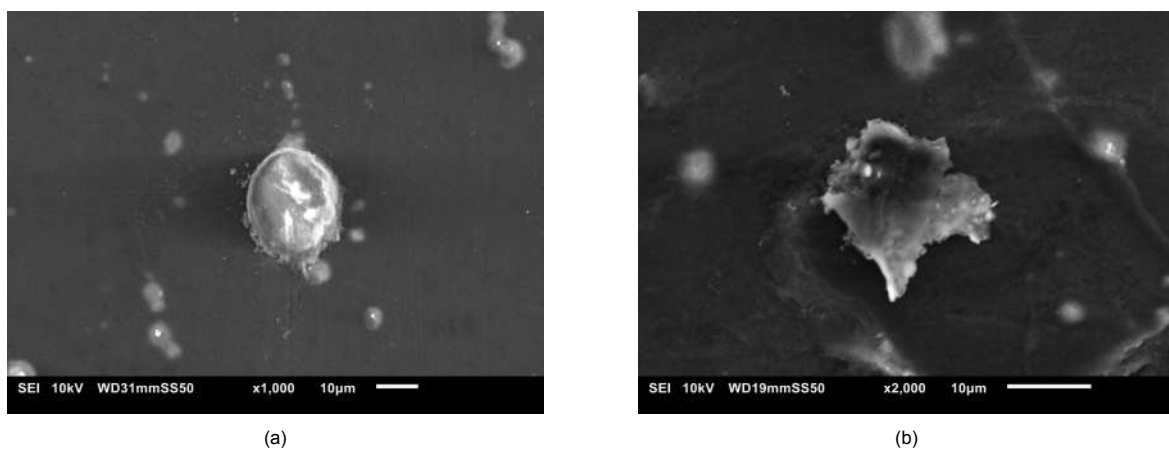
Figure 5.13: SEM images of the nanoparticles deposited on sample 2 at (a) x1000 and (b) x2000 magnification

(a)

(b)

(c)
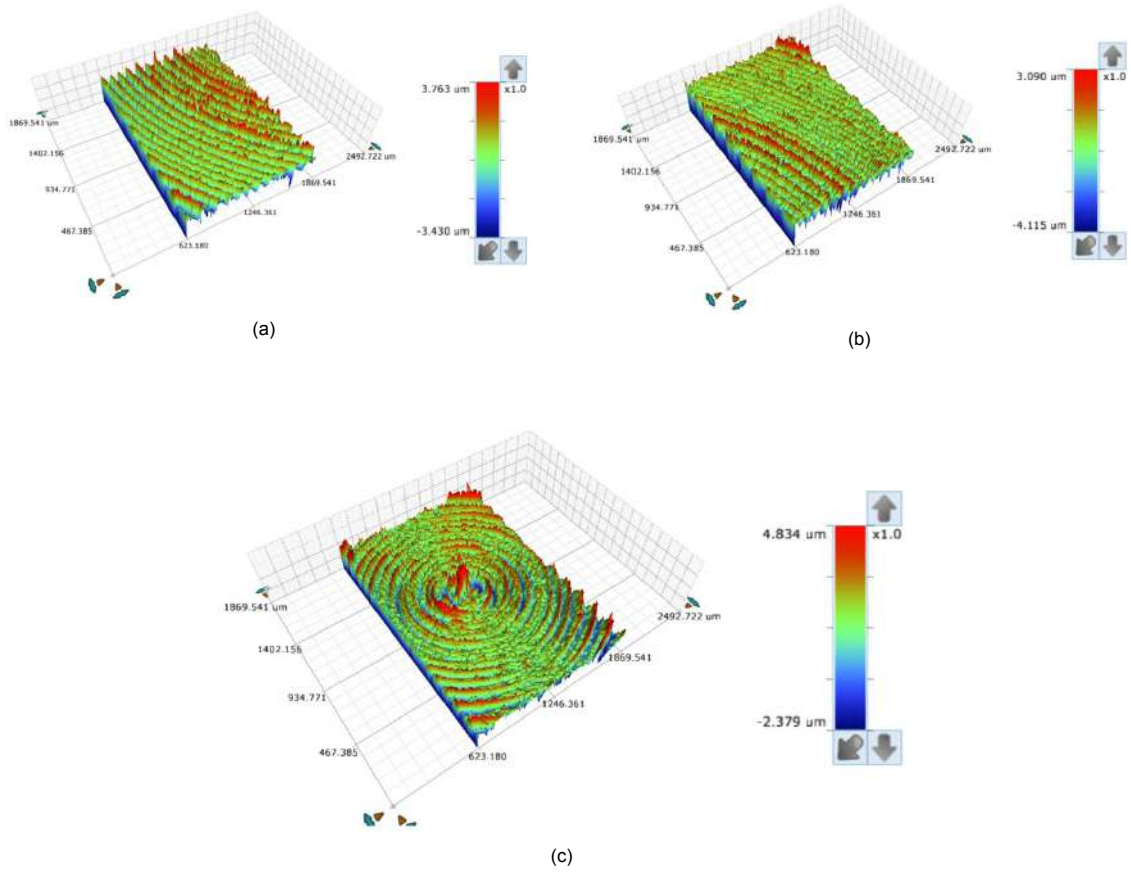
Figure 5.14: WLI images of sample 2 surface at different locations

5.6.4. Sample 3 surface analysis

(a)

(b)
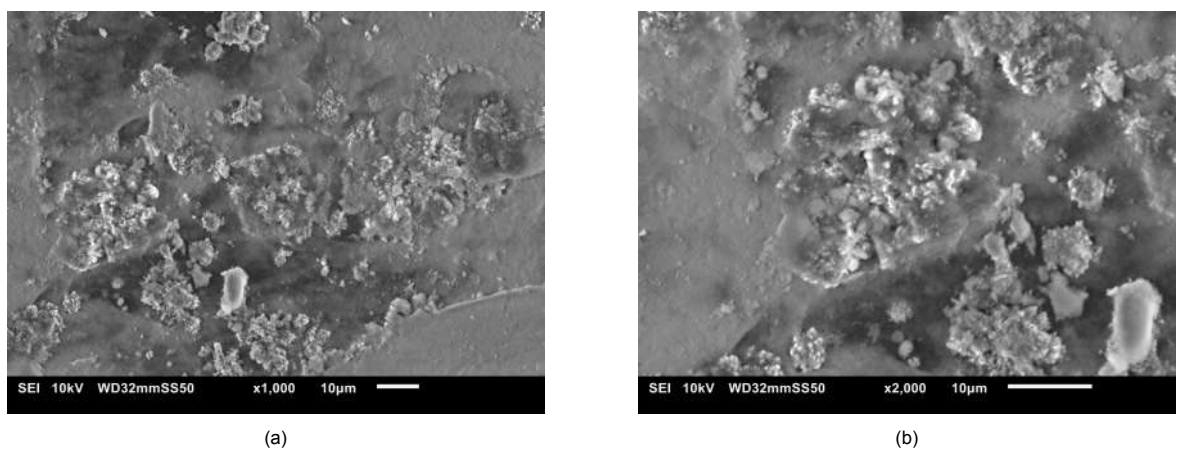
Figure 5.15: SEM images of the nanoparticles deposited on sample 3 at (a) x1000 and (b) x2000 magnification
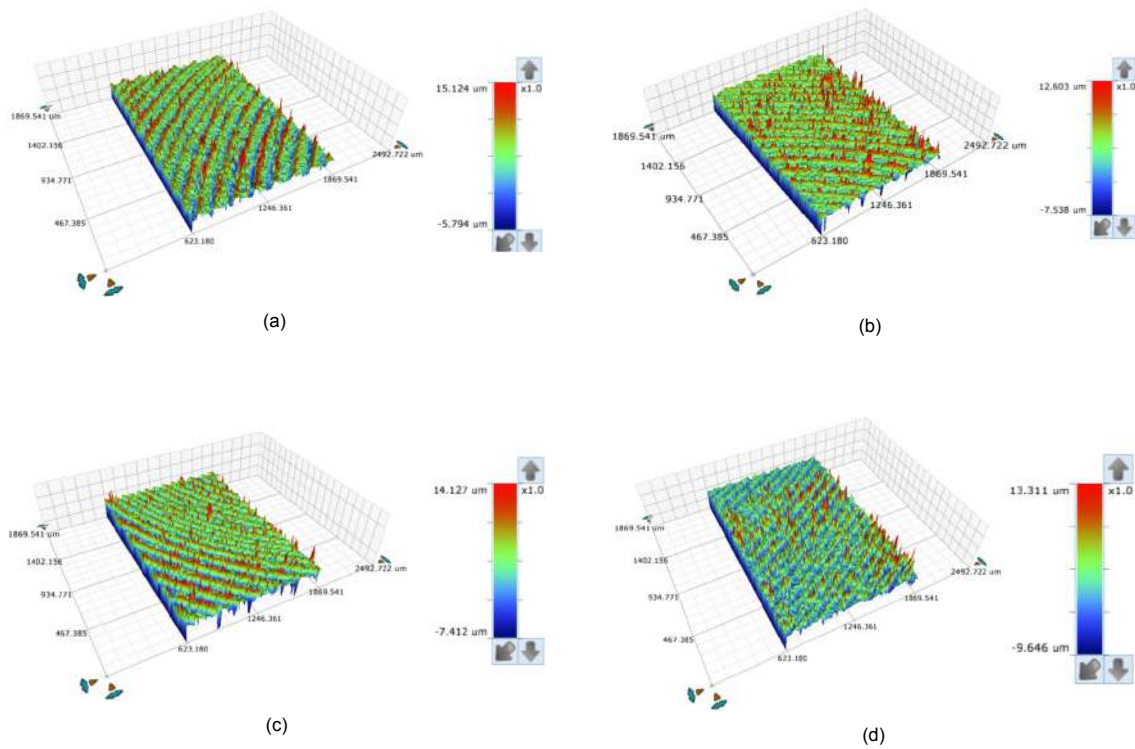
Figure 5.16: WLI images of sample 3 surface at different locations

5.6.5. Sample 4 surface analysis
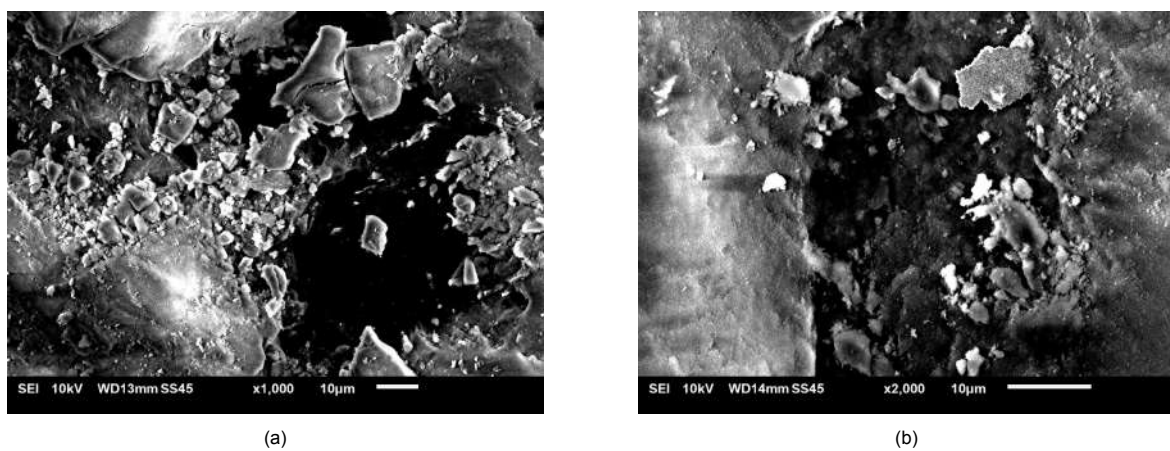
Figure 5.17: SEM images of the nanoparticles deposited on sample 4 at (a) x1000 and (b) x2000 magnification

(a)

(b)

(c)
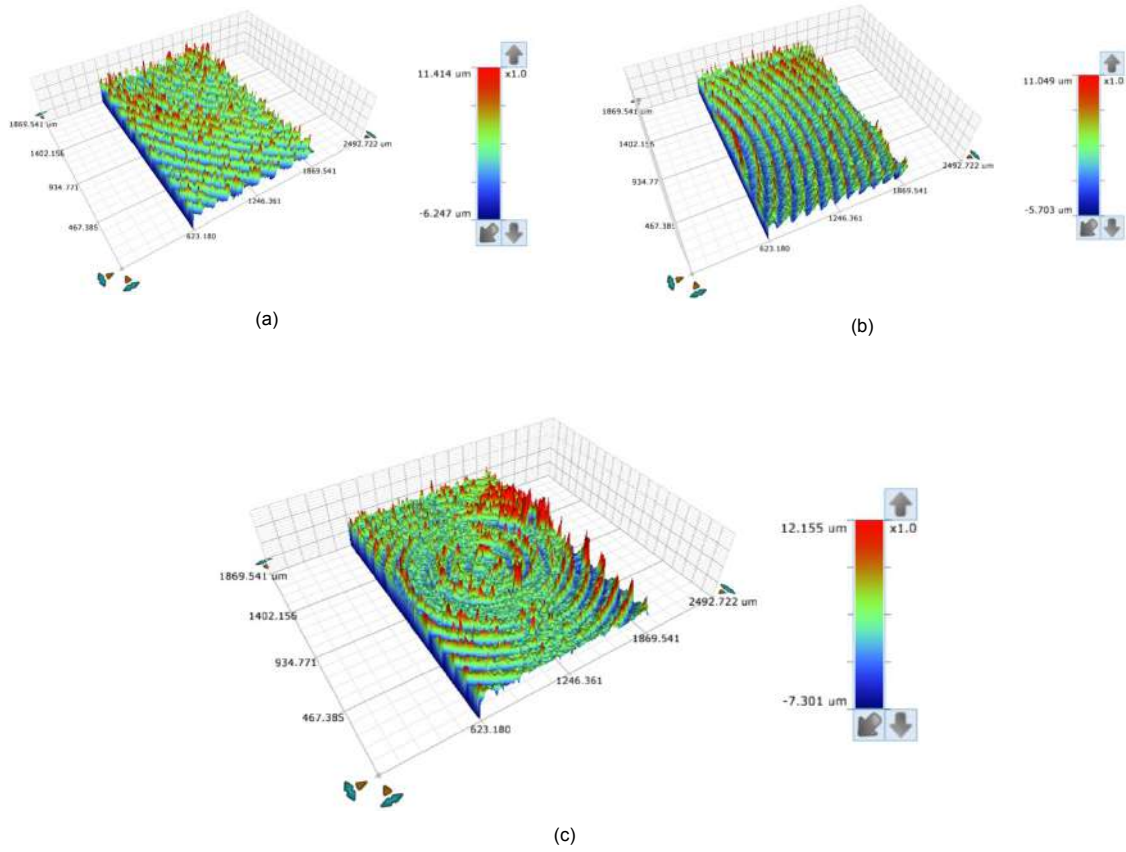
Figure 5.18: WLI images of sample 4 surface at different locations

5.6.6. Sample 5 surface analysis

(a)

(b)
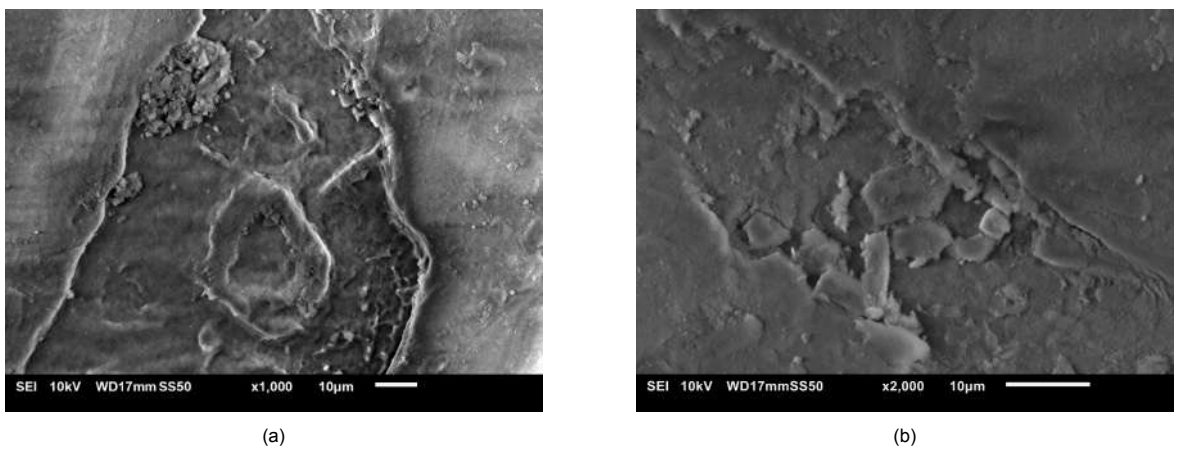
Figure 5.19: SEM images of the nanoparticles deposited on sample 5 at (a) x1000 and (b) x2000 magnification

(a)

(b)

(c)

(d)
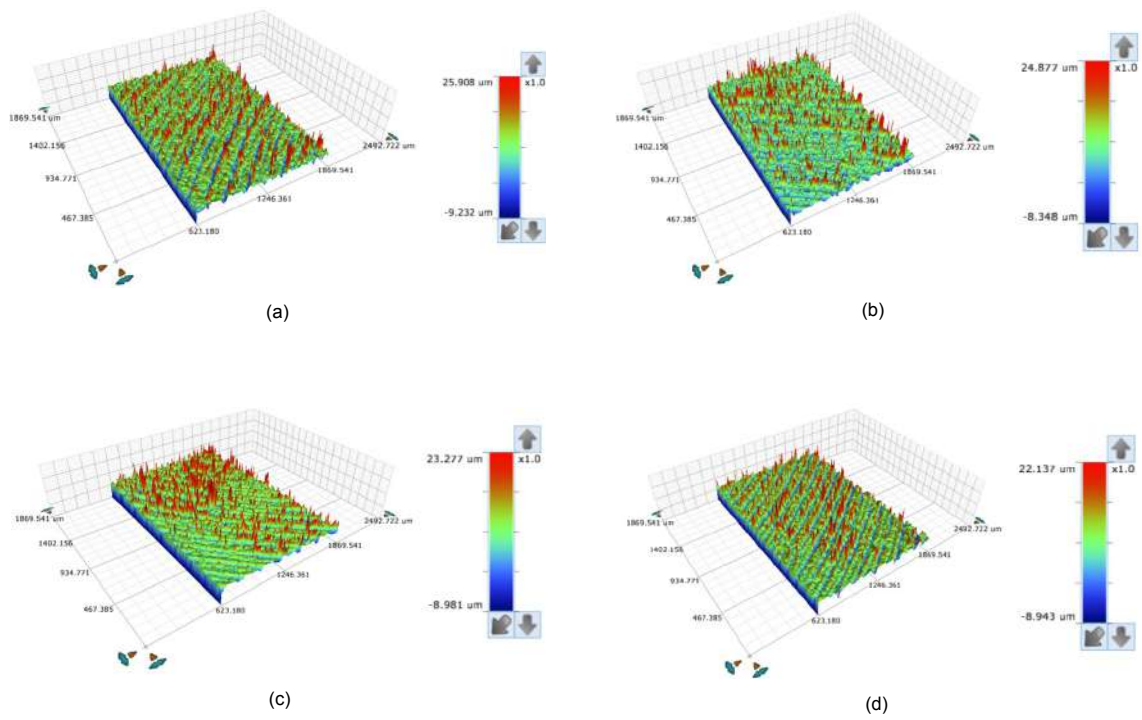
Figure 5.20: WLI images of sample 5 surface at different locations

5.6.7. Sample 6 surface analysis

(a)

(b)
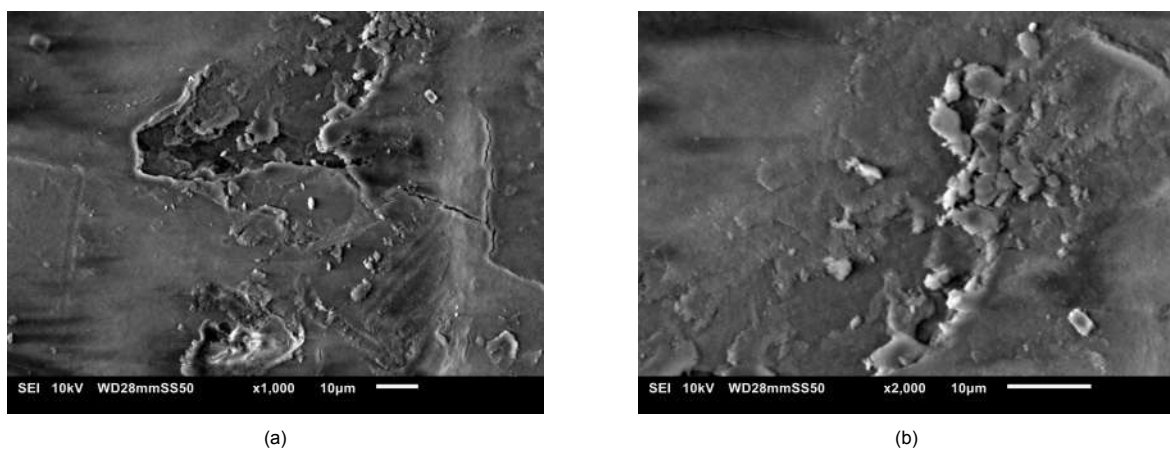
Figure 5.21: SEM images of the nanoparticles deposited on sample 6 at (a) x1000 and (b) x2000 magnification

(a)

(b)

(c)
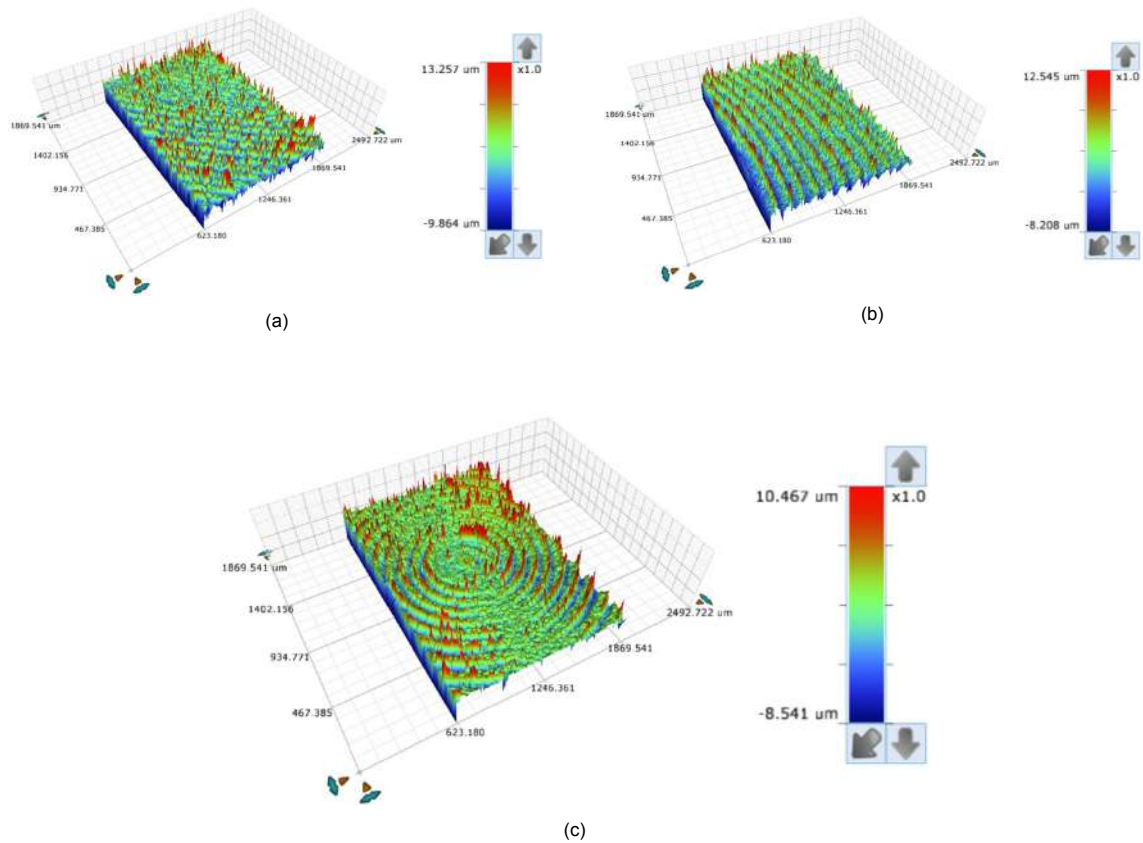
Figure 5.22: WLI images of sample 6 surface at different locations

5.6.8. Roughness parameters overview

This section aims at giving an insight into the fundamental principles of white light interferometry (WLI) with particular focus on the roughness parameters which may be derived.

Regarding surface topography, the scope of this project is to analyse relatively large samples ($\varnothing 35\ mm$) while being able to detect nano-scale features. To this end, the ContourGT-X Bruker 3D Optical Profiler, which applies WLI, was chosen as it meets these fundamental requirements. Instead of a coherent light source as in traditional interferometers, WLI uses a broadband incoherent light-source which emits light of different wavelengths. This implies that interference can occur only within the coherence length (i.e. the largest optical path length difference that two waves can sustain before they can no longer interfere [19]). In fact, in the range of the coherence length all wavelengths have almost the same phase conditions as at the light source so they can interfere [8].

The working principle of a white light interferometer is illustrated in Figure 5.23. The light emitted by the source is divided by a beam splitter into two beams: one is reflected from the reference mirror and the other one from the sample. A reference mirror is positioned inside the objective in such a way that it is in the same focal point as the sample. This configuration allows the beams to recombine at the beam splitter, where interference takes place. Then, the resulting *fringe pattern* consisting of light and dark bands is collected by the CCD camera. The interference pattern gives the light intensity as a function of the spatial coordinates, thus information on the surface height across the surface is extracted and converted into a 3D map. The interferogram mimics the surface topography: if the surface of the sample is flat the fringes are straight stripes, whereas in the case of a rough surface the fringes reproduce the surface texture. Moreover, the number of the fringes and their spacing depends on the relative tilt between the reference mirror and the sample.
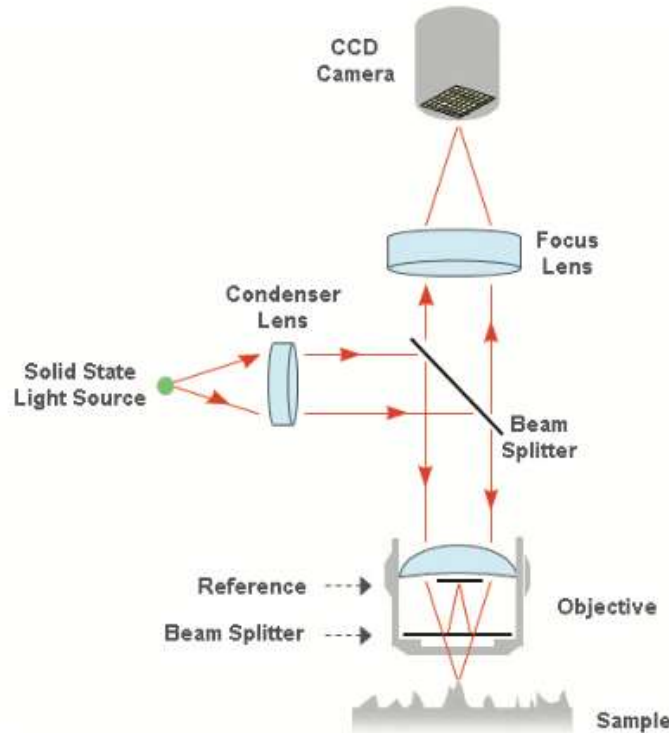
Figure 5.23: WLI working priciple

It must be noted that roughness measurements obtained with white light interferometry always include a filtering step. Indeed, surface texture is the combination of roughness (at micro- and nanoscale), waviness (at macroscopic level) and form. Therefore, roughness can be derived only after that the waviness and the form are removed, as described in the norm ISO 25178-2.

The data collected in the present work were taken in the VSI (Vertical Scanning Interferometry) mode. The maximum scan lenght is $10\ mm$ and the precision is in the nanometer range. Every measurement was configured in such a way to scan over a $1.8 \times 1.8\ mm^2$ area. For each sample, eighteen readings were performed at pre-defined locations; then the software Vision64 was used to visualize the 3D map of the surface and to calculate the roughness parameters.
In particular, the analysis was not limited to the average roughness Ra, but the skewness R_{sk} and the kurtosis R_{ku} were also considered. Indeed, the R_a represents the arithmetic mean of the absolute value of the vertical coordinate $Z(x)$ within the sampling length:

$$R_a = \frac{1}{\ell} \int_0^\ell Z(x)\mathrm{dx} \tag{5.8}$$

Effectively, the parameter R_a measures the deviation of each point on a surface from the mean height. However, as peaks and valleys are treated equally when calculating the average roughness, two surfaces may have the same R_a despite being characterized by two completely different surface textures. Since value of R_a does not reflect the specific features of a surface, it is not suitable to describe a boiling surface. In fact, as outlined in Chapter 2, only cavities of some critical dimensions and shapes can become active nucleation sites. Therefore, in order to gain insight into surface topography, additional parameters must be taken into account. In particular, the skewness R_{sk} measures the symmetry of a height profile about the mean line and the kurtosis R_{ku} quantifies the sharpness of the surface features (Figure 5.24). The skewness and the kurtosis are defined by the following equations, where R_q represents the root mean square height of the surface:

$$R_{sk} = \frac{1}{R_q^{3}} \left[\frac{1}{A} \iint_A Z^3(x,y) \, \mathrm{dxdy} \right] \tag{5.9}$$

$$R_{ku} = \frac{1}{R_q^{4}} \left[\frac{1}{A} \iint_A Z^4(x,y) \, \mathrm{dxdy} \right] \tag{5.10}$$
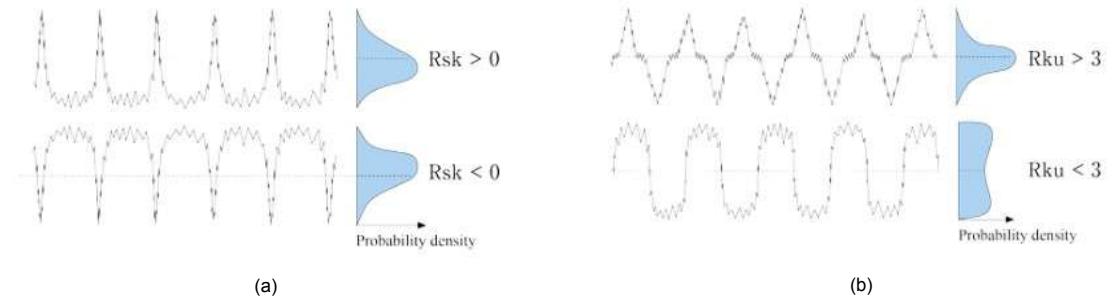
Figure 5.24: Representation of surface skewness and kurtosis

Table 5.2 summarizes the most representative surface parameters of the tested boiling surfaces. It must be noted that, with the exception of the base surface and the nanoparticles deposition on sample 2, all the nanoparticle-deposited surfaces are characterized by a kurtosis value significantly larger than 3. Thus, it can be inferred that the main effect of nanoparticles deposition upon boiling is to create sharper peaks on the surface. This can be seen also in the 3D surface maps given by WLI: while on the base surface (Figure 5.10) and on the nanoparticles deposition on sample 2 (Figure 5.14) the maximum height of the peaks is about $6 \ \mu m$, it is more than doubled on the other nanoparticle-deposited surfaces (Figures 5.12, 5.16, 5.18, 5.20, 5.22).

Regarding the skewness, it should be noted that $R_{sk} \simeq 0$ for the base surface, thus confirming that the samples had originally a symmetric profile. The value of the skewness is very small for the nanoparticles deposition on sample 2 as well, thus suggesting that the nanoparticles altered the initial surface profile only slightly. Since the Ra decreased and R_{ku} increased for this sample, it may be hypothesised that the nanoparticles filled the microcavities on the surface, thereby reducing the average roughness and creating some small size clusters (Figure 5.13). For all the other surfaces, $R_{sk} > 1$ signifies that there are more asperities than valleys on these surfaces. Moreover, the nanoparticles depositions on samples 1, 3, 4, 5, 6 have more than one of order of magnitude higher R_{sk} than the base surface and the deposition on sample 2.

Nonetheless, it remains unclear whether a direct relation between these surface parameters and the boiling heat transfer coefficient exists. Indeed, it can be observed that the boiling curves of the nanofluid on samples 3 and 4 are very close to each other (Figure 5.8), which seems to be consistent with the roughness data showing that the nanoparticles depositions on samples 3 and 4 led to fairly similar roughness parameters. However, the nanoparticles deposition on sample 5 is also characterized by roughness parameters of the same order of magnitude, but the boiling curve of the nanofluid on this sample is significantly shifted to the right. A reason for this might be that $R_{ku} = 16.69$ on sample 5, meaning that there are numerous high peaks (up to $25 \ \mu m$) on the surface, as illustrated in Figure 5.20. Therefore, the presence of long tails close to each other may be responsible for a decrease in the nucleation site density. In fact, the large nanoparticles clusters on the surface might have filled the cavities on the original surface, thus forming smaller nucleation sites which require a higher wall superheat to become active. Thereby, the boiling performance is negatively affected.

The most striking contradiction concerns sample 6. Even though the roughness characteristics of the nanoparticles deposition on sample 6 appear to be similar to those on sample 3, the trend of the corresponding boiling curves is completely different. This anomaly raises the question whether this is, in fact, an outlier. Conducting more experiments on additional samples may help to answer this question by revealing how wide the deviation among the boiling curves is in a larger dataset.

Surface	Ra	R_{ku}	R_{sk}	HTC_{linear}	HTC_{curve}
Base surface	0.915 μm	1.896	0.057	14749 $\frac{W}{m^2\ °C}$	12136 $\frac{W}{m^2\ °C}$
Nanoparticles deposition on sample 1	0.629 μm	8.210	1.304	18591 $\frac{W}{m^2\ °C}$	13363 $\frac{W}{m^2\ °C}$
Nanoparticles deposition on sample 2	0.546 μm	2.869	0.154	7240 $\frac{W}{m^2\ °C}$	7219 $\frac{W}{m^2\ °C}$
Nanoparticles deposition on sample 3	0.891 μm	11.04	1.762	15848 $\frac{W}{m^2\ °C}$	12018 $\frac{W}{m^2\ °C}$
Nanoparticles deposition on sample 4	1.082 μm	6.540	1.314	16059 $\frac{W}{m^2\ °C}$	11503 $\frac{W}{m^2\ °C}$
Nanoparticles deposition on sample 5	1.167 μm	16.69	2.427	11751 $\frac{W}{m^2\ °C}$	9604 $\frac{W}{m^2\ °C}$
Nanoparticles deposition on sample 6	1.003 μm	10.19	1.825	6298 $\frac{W}{m^2\ °C}$	5492 $\frac{W}{m^2\ °C}$

Table 5.2: Summary of surface roughness parameters for the tested surfaces

The last two columns of Table 5.2 display the boiling HTC calculated with two different methods. The former gives the HTC as the slope of the line which best approximates each boiling curve ($R^2 \simeq 0.98$). In the latter case, the HTC is calculated directly from the boiling curve for every wall superheat-heat flux data point and then the arithmetic average is computed. Since the wall superheat-heat flux coordinates of the data points vary across the different runs, the HTC value given by linear approximation is considered for further analysis.

5.7. Regression analysis with RStudio

As a final step, an attempt to understand the correlation between the HTC and the roughness parameters (Ra, R_{ku}, R_{sk}) as well as their relative importance in affecting the HTC was made. To this end, statistical analysis was performed using the software RStudio. In particular, the following objectives were addressed:

- Investigate on the dependency of the HTC on the roughness parameters by performing regression analysis;

- Describe the correlation between the HTC and the Ra, R_{ku}, R_{sk} with the best-fit model;

- Evaluate how strong the correlation is and the most significant parameter(s).

Detailed description of the aforementioned analysis may be found in Appendix E. In summary, a multi-variable linear model, a generalized additive model and a corrected linear model including a quadratic term were developed. The last model yielded the best fit to the experimental data and all the explanatory variable (Ra, R_{ku}, R_{sk}) were found to be statistically significant. This proved that the variance of the response (the HTC) is related to the variations of the roughness parameters, with R_{sk} being the most influential factor.

Nonetheless, it is worth mentioning that the outcome of the present statistical analysis is still at an embryonic stage. Indeed, it was based on a limited dataset and the physical meaning of the results has not been explored yet. Further investigation is required to clarify the reason why there is a stronger non-linear dependency of the HTC on the R_{sk} and to identify the physical mechanism responsible for that.

6

Conclusions and recommendations

6.1. Summary of findings

The objective of this thesis was to investigate on pool boiling heat transfer experimentally by analysing the behaviour of a pure fluid (water) and a water-alumina 0.1% wt nanofluid.

First, the key parameters which play a major role in the boiling process (i.e. surface material and topography, working medium properties, applied heat flux) were identified, then they were translated into specific requirements for the experimental setup. In particular, it was essential to ensure the possibility to control the input heat flux and to record temperature readings for the calculation of the wall superheat. Moreover, the design addressed the need of performing repeated testing on different surfaces and prolonged boiling while preventing loss of the working fluid. Therefore, the boiling setup was developed according to the aforementioned specifications and it was validated for pool boiling of water under atmospheric pressure.

A systematic methodology for the experimental work was adopted, consisting in characterizing every boiling surface with WLI (white light interferometry) and SEM (scanning electron microscopy) before and after the boiling run. Indeed, the experiments were performed on six aluminium samples, obtaining both the water and the nanofluid pool boiling curve for each of them. It was observed that the performance of the nanofluid is greatly inconsistent, as the heat transfer coefficient varies by more than 90% (this is the case when considering the leftmost and the rightmost curves in Figure 5.8). This behaviour might be partially explained by some differences in the texture of the boiling surfaces or in a misplacement of the thermocouples, thus giving erroneous temperature values. However, further experimental activity is required to verify whether the reason for such incongruous results is attributable to the boiling of the nanofluid itself, or to other external parameters (i.e. differences in the surface topography, influence of atmospheric pressure on pool boiling process).

Subsequently, the roughness parameters (average roughness R_a, kurtosis R_{sk}, and skewness R_{sk}) were derived and analysed in order to understand the effect of the nanoparticles deposition on the boiling process. In particular, an attempt to correlate the heat transfer coefficient with the surface characteristics was made, leading to the development of different correlations derived using a multi-variable regression model, a GAM model, and an adjusted linear model including a quadratic term.

The optimal fit to the experimental data was achieved with the last model, as all the predictors (Ra, R_{ku}, R_{sk}) were found to be statistically significant. This confirmed the underlying hypothesis that a correlation between the HTC and the surface characteristics exists. Moreover, the skewness R_{sk} was identified as the most influential factor.

However, the present statistical analysis does not fully justify the inconsistencies in the experimental data and the physical counterpart of the mathematical model requires further investigation.

6.2. Limitations

The limited amount of data collected in the present work is not sufficient to draw firm conclusion regarding the potential of nanofluids as more efficient heat transfer media. This follows from the difficulty in obtaining reliable repetitive results, both in terms of pool boiling curves and surface modification by the nanoparticles. Further experiments are required to elucidate the factors which cause the same nanofluid to lead to inconsistent results, despite the experimental procedure being the same.

Moreover, some inherent features of the present experimental apparatus limited the scope of the analysis. First, substituting the current heater with one able to provide higher power would enable to obtain the boiling curves over a broader range and observe whether a change in the slope occurs in proximity of the CHF. Then, including a pressure sensor in the setup would allow to assess the entity of pressure fluctuations during the boiling process and their impact on the boiling curve.

Regarding the accuracy of the measurements, it must be underlined that the calculation of the boiling surface temperature was extrapolated based only on the reading of one thermocouple. By inserting more temperature sensors in the sample (i.e. from the sides), it would be possible to derive the temperature gradient across the sample more precisely.

6.3. Future work

In order to gain deeper understanding of the boiling process using nanofluids, along with surface characteristics, the bubble dynamics should be investigated. Indeed, high-speed imaging is a powerful tool which would enable to get more insights on the nucleation site distribution, bubble departure diameter and frequency. These additional measurements may contribute to shed light on the differences between the behaviour of nanofluids and pure fluids and to identify other factors which may be at the root of the inconsistent trend among various boiling runs with the same nanofluid.

Moreover, the data collected in the present work have emphasized that there are some unknown factors which produce random variations in the nanoparticles deposition upon boiling of a nanofluid. Being the boiling performance a direct consequence of the surface topography and near-surface hydrodynamics, it is crucial to be in control of these characteristics in order to produce predictable and consistent results. Therefore, an alternative way to take advantage of the enhanced properties of nanoparticles may be to create surface coatings which are more repeatable. This may be achieved by means of various methods, such as electrophoretic and electrochemical deposition, chemical and physical vapour deposition, sputtering, electron beam evaporation [13]. Indeed, by setting the deposition process parameters (i.e. density and thickness of the layer, as well as spacing between surface features) it would be possible to ensure that the surface satisfies precise requirements in terms of heat transfer capability. In particular, recent studies [111] have demonstrated that optimized boiling performance, resulting from the enhancement of both the heat transfer coefficient and critical heat flux, requires a purposely engineered surface morphology. It has been shown that a hierarchically structured surface, consisting of micro- and nanofeatures, enables to define a nucleation site density such that bubble coalescence is minimized while promoting evaporation for HTC improvement. In particular, a surface texture combining microtubes and micropillars with a set pitch is able to keep the vapour bubbles separated after nucleation and to provide a capillary wicking effect. At the same time, nanoblades on top of these microstructures extend the liquid-vapour interface thus augmenting evaporation and enhancing the HTC. With this approach, the drawback of relying on an uncontrolled and unsteady deposition process associated with boiling of a nanofluid is avoided, as superior boiling performance follows from accurate engineering of the surface. Then, particular heat transfer demands may be achieved by tuning the surface morphology with various types of nanoparticles (i.e. different material and shape of the nanoparticles would give modified hydrophilicity of the surface) while using the same working fluid.

Appendices

A
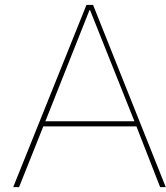
Zetasizer fundamentals

The Zetasizer Nano instrument (Malvern) was used to measure the particle size distribution and Zeta potential. The former is calculated by applying the dynamic light scattering technique (DLS), which measures the Brownian motion of nanoparticles by illuminating them with a laser beam and analysing the resulting intensity fluctuations in the scattered light. When small stationary particles are shined by a laser, they will scatter the light in all directions. If a screen is placed close to the particles, a speckle pattern produced by the scattered light will be observed on the screen (Figure A.1).
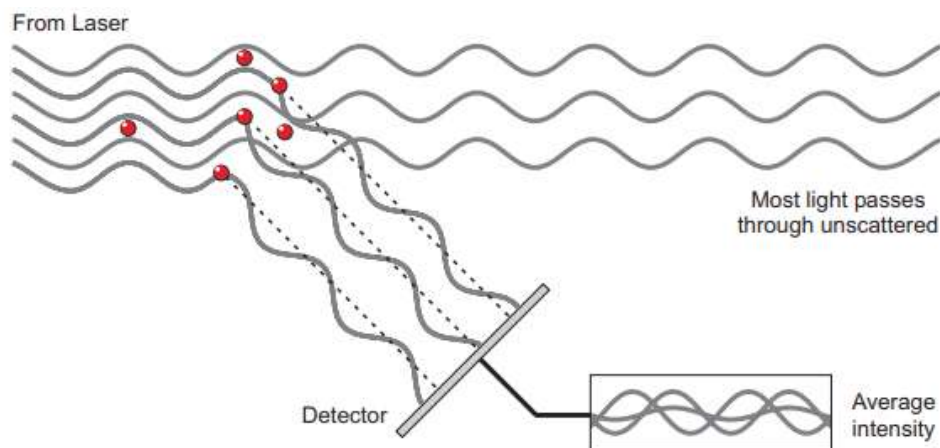
Figure A.1: DLS method

The bright areas on the screen are seen at locations where the light scattered by the particles has the same phase and thus interferes constructively forming a bright patch. Conversely, dark areas correspond to the regions where destructive interference takes place. Considering the case of a nanofluid, nanoparticles are constantly in motion due to the random collision with the molecules of the surrounding liquid (Brownian motion). Therefore, as nanoparticles move, bright and dark areas change in intensity. Then, the Zetasizer derives the size of the nanoparticles from the intensity fluctuations data. This process is performed by a digital correlator, which compares intensity signals at successive time instants. The correlation function is equal to 1 if the signal is compared with itself and it decays with time, eventually reaching 0 value.

A fundamental feature of Brownian motion is that smaller particles move faster than large ones and intensity of the speckle pattern fluctuates accordingly. Hence, the correlation function decays at higher rate for small particles (Figure A.2).
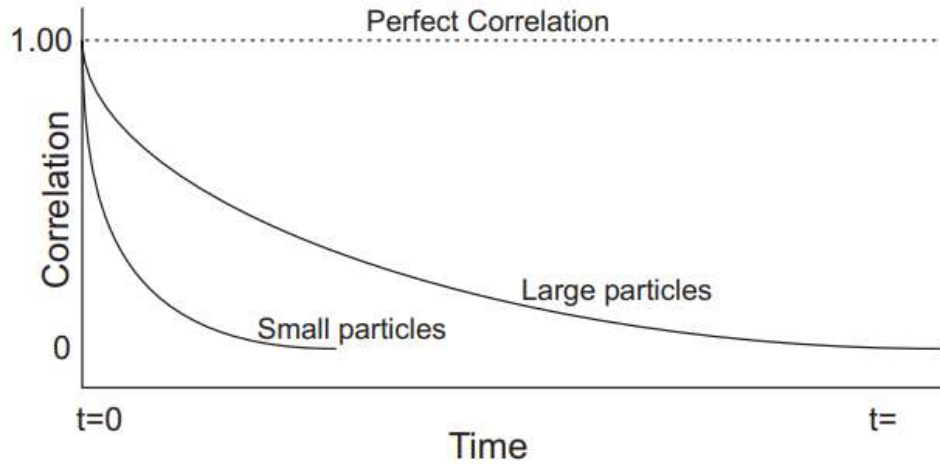
Figure A.2: Correlation function for small and large particles

Then, by means of algorithms, the Zetasizer software extracts the size distribution from the decay rates. Indeed, the correlation function may be modelled as follows:

$$G(\tau) = B + A \sum e^{-2q^2 \mathbb{D}\tau} \tag{A.1}$$

where $G(\tau)$ is the correlation function, B is the baseline at infinite time, A is the amplitude or intercept, τ is the correlator delay time, $\mathbb{D}$ is the translational diffusion coefficient, q is the scattering vector (a function of the dispersant refractive index, laser wavelength and detection angle). The correlation function plot (Figure A.3) shows the meaning of the aforementioned parameters graphically. In particular, $\mathbb{D}$ is obtained by fitting $G(\tau)$ with a suitable algorithm and it is used as an input to calculate the nanoparticles size applying the Stokes-Einstein equation.
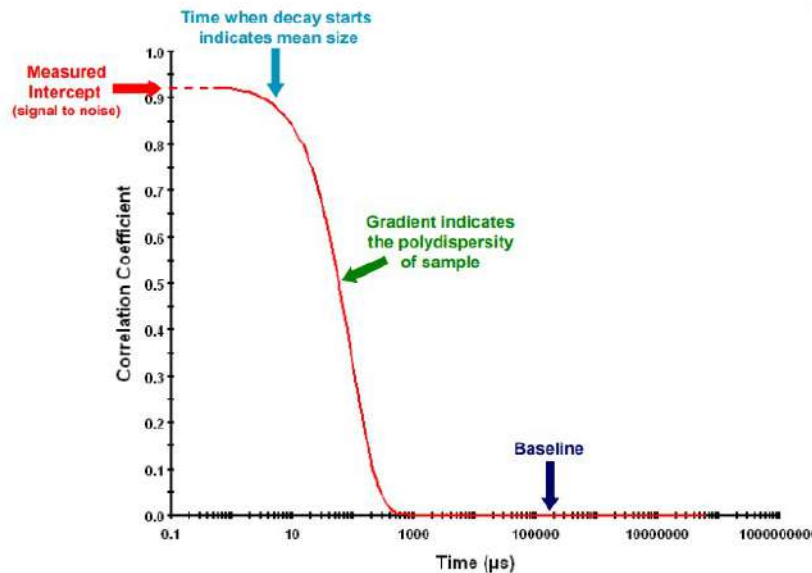
Figure A.3: Correlation function plot [26]

Indeed, $\mathbb{D}$ is the property that quantifies the Brownian motion velocity and its relation to the particle size is expressed by the Stokes-Einstein equation:

$$d(H) = \frac{k_B T}{3\pi\eta\mathbb{D}} \tag{A.2}$$

where $d(H)$ is the hydrodynamic diameter, k_B the Boltzmann's constant, T the absolute temperature and η the dynamic viscosity of the liquid medium. In particular, the hydrodynamic diameter of a particle corresponds to the diameter of a sphere with the same translational diffusion coefficient as the particle. Therefore, the hydrodynamic diameter provides insight into the behaviour of nanoparticles within a fluid [26] and this piece of information, rather than the primary particle size, is an indication of the boiling surface-nanoparticles interactions [127].

Futhermore, it must be noted that the DLS technique does not require the nanoparticles to be spherical, in fact it is applicable to any nanoparticle shape since the hydrodynamic size is defined as an *equivalent* spherical diameter. Hence, when nanosheets or nanorods are analysed, the hydrodynamic volume of these nanoparticles may be approximated as follows:

$$V \sim L^2 \times t \sim D_h^3 \tag{A.3}$$

where L and t are the nanoparticles length and thickness, respectively. Therefore, having measured D_h by means of the DLS, the nanosheet length may be derived using equation A.3. The validity of this approach is confirmed by the experimental work by Lotya et al. [80], who found the correlation between the mean lateral sheet size and the priamry peak diameter obtained by DLS to read as follows:

$$<L> = (0.07 \pm 0.03) D_h^{(1.5 \pm 0.15)} \tag{A.4}$$

The size report generated by the Zetasizer displays the results of the cumulants analysis, which is defined in the International Standards ISO 22412 (2017). This approach gives two values, namely the intensity-weighted mean diameter and the polidyspersity index, which measures the width of the size distribution. The size distribution report generated by the Zetasizer software for the water alumina 0.1% wt nanofluid is as follows:

Size Distribution Report by Intensity
v2.2

Sample Details

Sample Name:	alwtnf0.1 3		
SOP Name:	alwtnf1.sop		
General Notes:			

File Name:	alwtnf1.dts	**Dispersant Name:**	Water
Record Number:	6	**Dispersant RI:**	1,330
Material RI:	1,77	**Viscosity (cP):**	0,8872
Material Absorbtion:	0,100	**Measurement Date and Time:**	woensdag 4 mei 2022 10:39:06

System

Temperature (°C):	25,0	**Duration Used (s):**	60
Count Rate (kcps):	396,9	**Measurement Position (mm):**	3,00
Cell Description:	Disposable micro cuvette (40µl)	**Attenuator:**	6

Results

			Size (d.nm):	% Intensity:	St Dev (d.n...
Z-Average (d.nm):	115,1	**Peak 1:**	140,9	100,0	64,92
Pdl:	0,173	**Peak 2:**	0,000	0,0	0,000
Intercept:	0,921	**Peak 3:**	0,000	0,0	0,000
Result quality :	**Good**				

Malvern Panalytical
www.malvernpanalytical.com

Zetasizer Ver. 8.00.4813
Serial Number : MAL1080878

File name: alwtnf1.dts
Record Number: 6
04 mei 2022 10:40:21
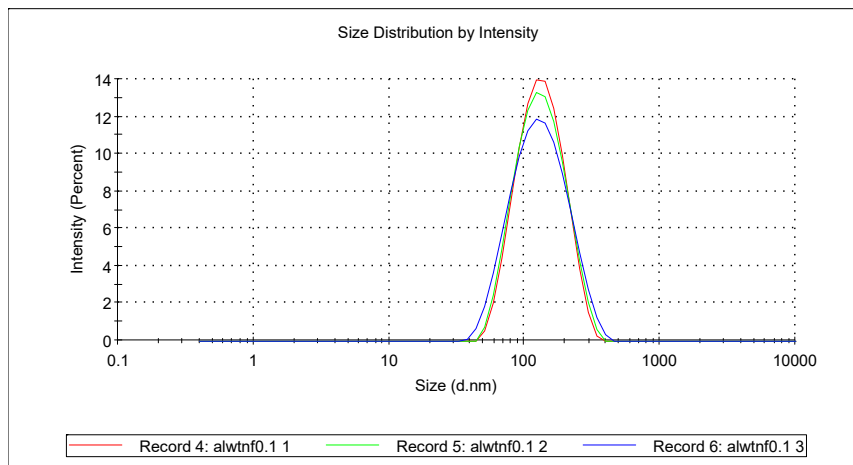
The Zeta potential ζ is the physical quantity that is used to characterize the stability of a suspension. This is of primary importance for nanofluids (Figure A.4), as they exhibit uniform thermophysical properties if and only if stability is ensured.

Stability is undermined by agglomeration, which refers to the formation of clusters of nanoparticles due to attraction forces resulting from their high surface energy [11].
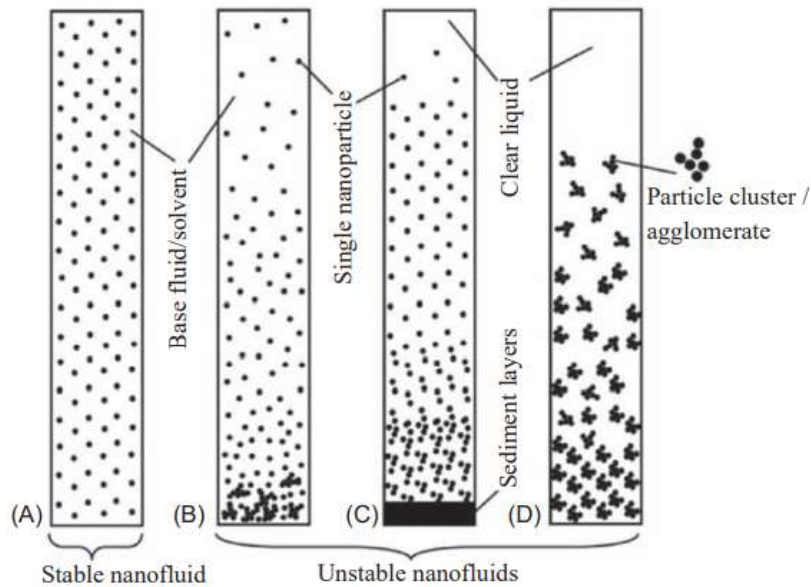
Figure A.4: Stability of nanofluids [47]

Different stability evaluation methods exist, among which the Zeta potential analysis. An electrical double layer is present around every particle in a colloidal suspension. Indeed, the net charge of a single particle (considered to be negatively charged) attracts ions of opposite sign close to the surface. Moreover, the liquid layer surrounding each particle consists of two parts, namely the Stern layer and the diffuse layer (Figure A.5a). The former corresponds to the inner region, where ions are closely attached, while the latter is the outer region, where ions are loosely bound. The potential at the interface between the diffuse layer and the bulk fluid (i.e. the so-called slipping plane), is denoted as the Zeta potential ζ. The magnitude of the Zeta potential gives an indication of the stability of a colloidal system, as illustrated in Figure A.5b. Conventionally, colloids are considered to be stable if $|\zeta| > 30mV$.
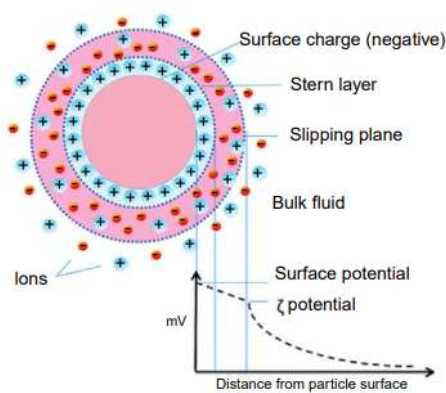
(a) Representation of the ζ potential [77]
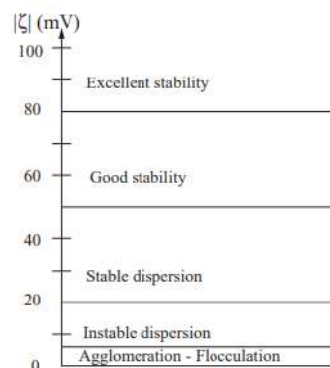
(b) Conditions for nanofluid stability [118]

Figure A.5: ζ potential principles

The Zetasizer Nano is used to perform an electrophoresis experiment, which consists in measuring the velocity of a particle in an electric field applied across an electrolyte. Then, the ζ potential is derived using the Henry's equation:

$$U_E = \frac{2\varepsilon\zeta f(Ka)}{3\eta}$$

(A.5)

where U_E is the electrophoretic mobility, ε is the dielectric constant, η is the viscosity and $f(Ka)$ is the Henry's function. For particles smaller than $200\ \mu m$ dispersed in low dielectric constant media $f(Ka) = 1$ according to the Huckel approximation.

Finally, the full Zeta potential report for the water-alumina $0.1\%\ wt$ nanofluid is as follows:

Zeta Potential Report

v2.3

Sample Details

Sample Name: z water alumina 0.1 1

SOP Name: z water alumina 0.1

General Notes:

File Name: z water alumina 0.1		**Dispersant Name:**	Water
Record Number: 1		**Dispersant RI:**	1,330
Date and Time: dinsdag 10 mei 2022 11:10:28		**Viscosity (cP):**	0,8872
		Dispersant Dielectric Constant:	78,5

System

Temperature (°C):	25,1	**Zeta Runs:**	12
Count Rate (kcps):	192,2	**Measurement Position (mm):**	2,00
Cell Description:	Clear disposable zeta cell	**Attenuator:**	9

Results

			Mean (mV)	Area (%)	St Dev (mV)
Zeta Potential (mV):	46,1	**Peak 1:**	46,1	100,0	8,11
Zeta Deviation (mV):	8,11	**Peak 2:**	0,00	0,0	0,00
Conductivity (mS/cm):	0,0235	**Peak 3:**	0,00	0,0	0,00
Result quality :	**Good**				

Zeta Potential Distribution

Record 1: z water alumina 0.1 1   Record 2: z water alumina 0.1 2
Record 3: z water alumina 0.1 3

Malvern Panalytical
www.malvernpanalytical.com

Zetasizer Ver. 8.00.4813
Serial Number : MAL1080878

File name: z water alumina 0.1
Record Number: 1
10 mei 2022 11:16:20
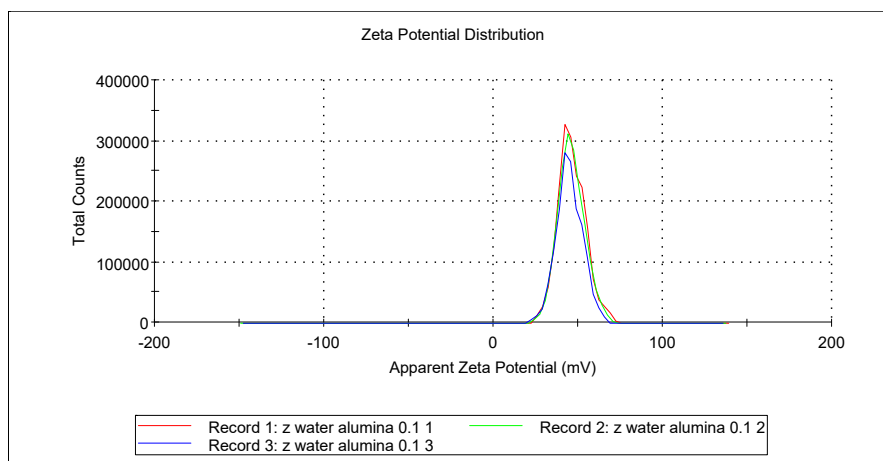
B

List of parts and drawings

Table B.1 summarizes the parts which have been purchased for the making of the pool boiling setup.

Part	Size	Manufacturer
Heating element	$\varnothing 50 \; mm$	BACH Resistor Ceramics GmbH
Borosilicate glass tube	$35 \; mm \; i.d. \; 40 \; mm \; o.d.$	TE Instruments
PTFE sheet	$7 \; mm$ thickness	RS Components
Vermiculite plate	$1 \; cm$ thickness	Pull BV
Silicone O-ring	$\varnothing 32 \times 1.6 \; mm$	Techniparts BV
T-type thermocouples	$\varnothing 1 \; mm$ wires	TC Direct
Bolts	M4	Gamma BV

Table B.1: Purchased parts for the boiling setup

The technical drawings of the following elements are displayed in the next pages:

- Heating element

- Aluminium sample

- Glass tube

- Silicone O-ring

- Teflon insulation

- Vermiculite plate

- Cold finger condenser

Finally, the exploded view of the assembly is shown.

400 ±5

34 ±5

(Ø 1,05)

im Bereich der Loetstelle tritt
Lot nach aussen

(7,2)

(5)

(Ø 50)

Anschlussdraehte durch
Punktschweißen verlaengert

37 ±0,5

0NA00-00

1   4   2   3   5

TOLERANCES: siehe Einzelteil	FINISH:		DEBUR AND BREAK SHARP EDGES		DO NOT SCALE DRAWING	
					MATERIAL: siehe Stueckliste	

REV.	REVISION NO.	DATE	NAME		NAME	DATE
1.0	-	31.03.2014		DESIGNED	R. Mielke	31.03.2014
1.1	R1859	11.03.2021	R. M.	DRAWN	R. Mielke	31.03.2014
				APP'D		

TITLE:
Heizelement-LB

BACH·RC
Bach Resistor Ceramics GmbH

DWG NO.
5E-10000-14-62

A4

WEIGHT: 36.98 g   SCALE: 1:1   SAP NO.   SHEET 1 OF 2

100 mm SCALE 1:1

Ø 35,00 ± 0,1
Ø 50,00 ±0,5

Ø 1,00 ±0,1
Ø 33,30 ±0,1
Ø 35,00 -,01
Ø 50,00 ±0,5

1,25 ±0,1
1,50 ±0,1
1,25 ±0,1

1,5 ±0,05

4,00 ±0,5
8,00 ±0,5

Ø 1,00 ±0,1

UNLESS OTHERWISE SPECIFIED: DIMENSIONS ARE IN MILLIMETERS SURFACE FINISH: TOLERANCES: LINEAR: ANGULAR:			FINISH:		DEBURR AND BREAK SHARP EDGES	DO NOT SCALE DRAWING	REVISION
	NAME	SIGNATURE	DATE			TITLE:	
DRAWN							
CHK'D							
APPV'D							
MFG							
Q.A				MATERIAL:		DWG NO.	

sample round model with close walls

WEIGHT:
SCALE:2:1
SHEET 1 OF 1

$\varnothing 35.00 \pm 0.1$

$\varnothing 40.00 \pm 0.5$

30.00 ± 0.5

	NOME	FIRMA	DATA			TITOLO:	
DISEG.							
VERIF.							
APPR.							
FABB.							
Qual.							

SE NON SPECIFICATO:
QUOTE IN MILLIMETRI
FINITURA SUPERFICIE:
TOLLERANZE:
   LINEARE:
   ANGOLARE:

FINITURA:

INTERRUZIONE
BORDI NETTI

NON SCALARE DISEGNO

REVISIONE

MATERIALE:

N. DISEGNO

glass tube

A4

PESO:

SCALA:1:1

FOGLIO 1 DI 1

4   3   2   1

$\varnothing$ 32.00

R 0.8

	NOME	FIRMA	DATA			TITOLO:		
DISEG.								
VERIF.								
APPR.								
FABB.								
Qual.								

SE NON SPECIFICATO:
QUOTE IN MILLIMETRI
FINITURA SUPERFICIE:
TOLLERANZE:
  LINEARE:
  ANGOLARE:

FINITURA:

INTERRUZIONE
BORDI NETTI

NON SCALARE DISEGNO

REVISIONE

MATERIALE:

PESO:

N. DISEGNO

rubber o ring

A4

SCALA:1:1

FOGLIO 1 DI 1

24,25

32,00

6 X Ø 4,00

Ø 39,00

Ø 50,00

7,00

120,00

7,00

120,00

SE NON SPECIFICATO: QUOTE IN MILLIMETRI FINITURA SUPERFICIE: TOLLERANZE: LINEARE: ANGOLARE:	FINITURA:		INTERRUZIONE BORDI NETTI	NON SCALARE DISEGNO	REVISIONE

	NOME	FIRMA	DATA		TITOLO:
DISEG.					
VERIF.					
APPR.					
FABB.					
Qual.			MATERIALE:		

teflon insulation A3

	N. DISEGNO	
PESO:	SCALA:1:2	FOGLIO 1 DI 1

Ø 50,00
6 X Ø 4,00
6,00
5,00
28,50
120,00
10,00
10,00
120,00

SE NON SPECIFICATO: QUOTE IN MILLIMETRI FINITURA SUPERFICIE: TOLLERANZE: LINEARE: ANGOLARE:	FINITURA:			INTERRUZIONE BORDI NETTI	NON SCALARE DISEGNO		REVISIONE
	NOME	FIRMA	DATA		TITOLO:		
DISEG.							
VERIF.							
APPR.							
FABB.							
Qual.			MATERIALE:		N. DISEGNO	vermiculite plate	A3
			PESO:		SCALA:1:2	FOGLIO 1 DI 1	

$$C$$

Uncertainty analysis

The uncertainty represents an interval about the measured value within which the true value is expected to fall at a given level of probability [30]. Uncertainty propagation refers to the assessment of how uncertainties in the recorded quantities (i.e. the *variables*) affect the uncertainty in the *results*, which are calculated using the measured values. The general form for representing a variable is:

$$X_i = X_i(measured) \pm \delta X_i \quad (P\%) \tag{C.1}$$

where $X_i(measured)$ represents the most probable estimate of the true value of X_i based on the available data and δX_i is the uncertainty interval, which combines the effect of both random and systematic errors in the measurement of a variable, at a given probability level $P\%$.

An experimental result, denoted with R, may be assumed to be calculated from the values of different variables:

$$R = R(X_1, X_2, X_3, ..., X_N) \tag{C.2}$$

In order to to express the uncertainty in the calculated result at the same odds as the uncertainties in the measurements, Kline and McClintock [65] showed that the uncertainty in a computed result may be estimated with good accuracy using a root-sum square combination of the individual effects the variables:

$$\delta R = \left\{ \sum_{i=1}^{N} \left(\frac{\partial R}{\partial X_i} \delta X_i \right)^2 \right\}^{1/2} \tag{C.3}$$

where the partial derivative of R with respect to X_i is referred to as the sensitivity coefficient. Equation C.3 applies provided that every measurement is independent and, if repeated observations of a measurement are made, they would follow a Gaussian distribution. Moreover, if the uncertainty in each measurement is initially given at the same odds, the root-sum square operation would preserve the odds in the result.
Frequently, it is convenient to express the uncertainty in relative terms (i.e. as a fraction of the reading). In particular, whenever a result may be written as a product form:

$$R = X_1{}^a X_2{}^b X_3{}^c ... X_M{}^m \tag{C.4}$$

then the relative uncertainty is given by:

$$\frac{\delta R}{R} = \left[\left(a \frac{\delta X_1}{X_1} \right)^2 + \left(b \frac{\delta X_2}{X_2} \right)^2 + ... + \left(m \frac{\delta X_M}{X_M} \right)^2 \right]^{\frac{1}{2}} \tag{C.5}$$

Therefore, the relative uncertainties in the present studies were calculated as follows:

- Uncertainty in the applied heat flux:

$$q = \frac{VI}{A} = \frac{VI}{\pi \frac{D^2}{4}} \tag{C.6}$$

$$\frac{\delta q}{q} = \left[\left(\frac{\delta V}{V_{max}} \right)^2 + \left(\frac{\delta I}{I_{max}} \right)^2 + \left(\frac{\delta A}{A} \right)^2 \right]^{\frac{1}{2}} \tag{C.7}$$

- Uncertainty in the wall superheat:

$$\Delta T = T_s - T_b \tag{C.8}$$

$$\delta \Delta T = \left[(\delta T_s)^2 + (\delta T_b)^2 \right]^{\frac{1}{2}} \tag{C.9}$$

- Uncertainty in the heat transfer coefficient:

$$h = \frac{q}{\Delta T} \tag{C.10}$$

$$\frac{\delta h}{h} = \left[\left(\frac{\delta q}{q} \right)^2 + \left(\frac{\delta \Delta T}{\Delta T} \right)^2 \right]^{\frac{1}{2}} \tag{C.11}$$

Moreover, in a single-sample uncertainty analysis, there are three levels of uncertainty associated with a result, namely the zeroth-, first-, and Nth-order uncertainty. The zeroth-order uncertainty accounts for the contribution of the measuring equipment to the total uncertainty. The first-order uncertainty predicts the scatter that should be found in the data when performing repeated measurements with the same instruments. The Nth-order uncertainty represents the overall uncertainty as it comprises the effects of both fixed and variable errors. It must be noted that equation C.3 yields the single-sample uncertainty in a result irrespective of whether the zeroth-, first-, or Nth-level interval is being calculated [87].

If systematic errors may assumed to be negligible as a consequence of the calibration of the measuring instruments, then the probable range of random errors is given by $\pm t s_{\bar{x}}$, which is the confidence interval about the mean value of x with coverage factor t at probability level $P\%$. This confidence interval quantifies the random standard uncertainty $s_{\bar{x}}$, which is defined as follows:

$$s_{\bar{x}} = \frac{\sigma}{\sqrt{N}} \tag{C.12}$$

where σ is the standard deviation of the population and N is the sample size. The random standard uncertainty corresponds to a probability level of $P\% = 68\%$. However, final uncertainties are normally reported at $P\% = 95\%$, which is the probability covered by $\pm 2 s_{\bar{x}}$.

C.0.1. Design-stage uncertainty

A first estimate of the minimum uncertainty to be expected prior to any measurement follows from the available information on the instruments [30]. Thus, the uncertainty at the design stage u_d is given by the combination of the zeroth-order uncertainty u_0, which is assigned the value of one-half of the instrument resolution, and the instrument uncertainty u_c as specified by the manufacturer.

$$u_d = \sqrt{u_0{}^2 + u_c{}^2} \tag{C.13}$$

$$u_0 = \frac{1}{2} resolution \tag{C.14}$$

Table C.1 displays u_0, u_c and u_d for the instruments used in the present experimental work.

Variable	Instrument	u_0	u_c	u_d
Surface area [m]	Vernier caliper	$\pm 0.01\ mm$	$\pm 0.1\ mm$	$\pm 0.10\ mm$
Voltage [V]	Display of the power supply	$\pm 0.5\ V$	$\pm 0.2\ V$	$\pm 0.54\ V$
Current [A]	Display of the power supply	$\pm 0.0005\ A$	$\pm 0.03\ A$	$\pm 0.030\ A$
Temperature [$°C$]	Calibrated T-type thermocouple	$\pm 0.05\ °C$	$\pm 1\ °C$	$\pm 1.0\ °C$

Table C.1: Instrument uncertainties

C.0.2. Higher-order uncertainty

As design-stage uncertainty does not include the errors resulting from the experimental procedure (i.e. calibration, data acquisition and data reduction), an advanced-stage uncertainty analysis is required to report experimental results. In particular, the first-order uncertainty accounts for the variability of the variables when repeated measurements are performed under fixed operating conditions. The first-order uncertainty is calculated as follows:

$$u_1 = t\ s_{\bar{x}} \tag{C.15}$$

Finally instruments' characteristics are considered as well, giving the Nth-order uncertainty:

$$u_N = \sqrt{u_c{}^2 + \sum_{i=1}^{N-1} u_i{}^2} \tag{C.16}$$

C.0.3. Pool boiling data and uncertainties

This section includes the pool boiling data for the different samples and the corresponding uncertainties in the measured quantities.

- Sample 1

Wall superheat [$°C$]	u_{DT} [$°C$]	Heat flux [kW/m^2]	u_q [kW/m^2]
3.74	0.67	36.4	3.8
4.57	0.66	48.9	5.1
5.73	0.66	63.4	6.6
7.16	0.66	80.0	8.3
8.82	0.66	98.7	10.3
10.25	0.66	119.5	12.4
11.58	0.66	141.3	14.7
12.69	0.66	164.2	17.1
13.98	0.66	181.9	18.9
16.36	0.66	215.2	22.4
18.14	0.66	243.2	25.3
19.94	0.66	272.3	28.3
21.72	0.66	301.4	31.3

Table C.2: Pool boiling data of water on sample 1

Wall superheat $[°C]$	$\mathbf{u_{DT}}$ $[°C]$	Heat flux $[kW/m^2]$	$\mathbf{u_q}$ $[kW/m^2]$
3.85	0.66	36.4	3.8
4.64	0.66	48.9	5.1
5.58	0.66	63.4	6.6
6.93	0.66	80.0	8.3
8.23	0.66	98.7	10.3
9.43	0.66	119.5	12.4
10.54	0.66	140.3	14.6
11.64	0.66	164.2	17.1
12.83	0.66	189.2	19.7
13.99	0.66	215.2	22.4
15.31	0.66	243.2	25.3
16.78	0.66	272.3	28.3
18.26	0.67	301.4	31.3

Table C.3: Pool boiling data of water-alumina $0.1\% \, wt$ nanofluid on sample 1

- Sample 2

Wall superheat $[°C]$	$\mathbf{u_{DT}}$ $[°C]$	Heat flux $[kW/m^2]$	$\mathbf{u_q}$ $[kW/m^2]$
3.04	0.66	36.4	3.8
3.89	0.66	48.9	5.1
5.63	0.66	63.4	6.6
8.11	0.66	80.0	8.3
10.62	0.66	98.7	10.3
13.05	0.66	117.4	12.2
15.59	0.66	140.3	14.6
17.93	0.66	162.1	16.9
20.08	0.66	189.2	19.7
21.37	0.66	214.1	22.3
23.65	0.66	242.2	25.2

Table C.4: Pool boiling data of water on sample 2

Wall superheat $[°C]$	$\mathbf{u_{DT}}$ $[°C]$	Heat flux $[kW/m^2]$	$\mathbf{u_q}$ $[kW/m^2]$
5.57	0.67	35.3	3.7
6.54	0.67	48.9	5.1
8.04	0.67	62.4	6.5
10.63	0.66	79.0	8.2
13.30	0.66	95.6	9.9
15.99	0.66	114.3	11.9
18.72	0.66	133.0	13.8
21.51	0.67	153.8	16.0
23.99	0.67	176.7	18.4

Table C.5: Pool boiling data of water-alumina $0.1\% \, wt$ nanofluid on sample 2

- Sample 3

Wall superheat [$^\circ C$]	u_{DT} [$^\circ C$]	Heat flux [kW/m^2]	u_q [kW/m^2]
4.30	0.66	36.4	3.8
4.05	0.66	48.9	5.1
5.23	0.66	63.4	6.6
6.53	0.66	81.1	8.4
8.05	0.66	98.7	10.3
9.59	0.66	119.5	12.4
11.02	0.66	141.4	14.7
12.24	0.66	164.2	17.1
13.40	0.66	189.2	19.7
14.43	0.66	216.2	22.5
15.66	0.67	244.3	25.4
16.72	0.66	273.4	28.4
18.00	0.66	303.5	31.6

Table C.6: Pool boiling data of water on sample 3

Wall superheat [$^\circ C$]	u_{DT} [$^\circ C$]	Heat flux [kW/m^2]	u_q [kW/m^2]
4.28	0.67	36.4	3.8
4.72	0.66	48.9	5.1
6.03	0.66	63.4	6.6
7.38	0.66	80.0	8.3
8.95	0.66	98.7	10.3
10.48	0.66	118.5	12.3
11.84	0.66	140.3	14.6
13.16	0.66	163.2	17.0
14.39	0.66	188.1	19.6
15.69	0.66	214.1	22.3
17.05	0.66	241.1	25.1
18.82	0.67	270.2	28.1
21.08	0.67	299.3	31.1

Table C.7: Pool boiling data of water-alumina $0.1\% \; wt$ nanofluid on sample 3

- Sample 4

Wall superheat $[°C]$	$\mathbf{u_{DT}}$ $[°C]$	Heat flux $[kW/m^2]$	$\mathbf{u_q}$ $[kW/m^2]$
6.92	0.67	36.4	3.8
5.95	0.66	48.9	5.1
6.82	0.66	63.4	6.6
7.90	0.66	80.0	8.3
9.30	0.66	98.7	10.3
10.78	0.66	118.5	12.3
11.97	0.66	140.3	14.6
12.93	0.67	163.2	17.0
13.69	0.66	187.1	19.5
14.48	0.67	213.1	22.2
15.32	0.67	241.1	25.1
16.02	0.67	269.2	28.0
16.78	0.67	298.3	31.0

Table C.8: Pool boiling data of water on sample 4

Wall superheat $[°C]$	$\mathbf{u_{DT}}$ $[°C]$	Heat flux $[kW/m^2]$	$\mathbf{u_q}$ $[kW/m^2]$
5.61	0.67	36.4	3.8
5.22	0.67	48.9	5.1
6.32	0.66	63.4	6.6
7.69	0.66	80.0	8.3
9.17	0.66	97.7	10.2
10.52	0.66	117.4	12.2
11.53	0.66	139.3	14.5
12.65	0.66	160.1	16.6
13.99	0.66	176.7	18.4
15.42	0.67	200.6	20.9
16.80	0.67	224.5	23.3
18.15	0.67	248.4	25.8
19.58	0.67	274.4	28.5

Table C.9: Pool boiling data of water-alumina 0.1% wt nanofluid on sample 4

• Sample 5

Wall superheat $[°C]$	$\mathbf{u_{DT}}$ $[°C]$	Heat flux $[kW/m^2]$	$\mathbf{u_q}$ $[kW/m^2]$
7.29	0.67	36.4	3.8
6.35	0.67	48.9	5.1
7.49	0.67	63.4	6.6
8.98	0.66	80.0	8.3
10.89	0.66	97.7	10.2
12.91	0.67	117.4	12.2
14.90	0.67	139.3	14.5
16.91	0.67	162.1	16.9
18.66	0.67	186.0	19.3
20.58	0.67	210.0	21.8
22.70	0.67	237.0	24.6
24.91	0.67	266.1	27.7

Table C.10: Pool boiling data of water on sample 5

Wall superheat $[°C]$	$\mathbf{u_{DT}}$ $[°C]$	Heat flux $[kW/m^2]$	$\mathbf{u_q}$ $[kW/m^2]$
7.00	0.67	36.4	3.8
5.19	0.67	48.9	5.1
6.68	0.66	63.4	6.6
8.38	0.66	80.0	8.3
10.30	0.66	97.7	10.2
12.38	0.66	117.4	12.2
14.47	0.66	138.2	14.4
16.41	0.67	160.1	16.6
18.47	0.67	184.0	19.1
20.26	0.67	210.0	21.8
22.55	0.67	235.9	24.5
24.41	0.67	264.0	27.5
25.91	0.67	293.1	30.5

Table C.11: Pool boiling data of water-alumina 0.1% wt nanofluid on sample 5

- Sample 6

Wall superheat $[°C]$	$\mathbf{u_{DT}}$ $[°C]$	Heat flux $[kW/m^2]$	$\mathbf{u_q}$ $[kW/m^2]$
7.13	0.67	36.4	3.8
5.21	0.66	48.9	5.1
6.44	0.66	63.4	6.6
8.11	0.66	80.0	8.3
10.04	0.66	97.7	10.2
11.83	0.66	118.5	12.3
13.73	0.66	139.3	14.5
15.81	0.66	162.1	16.9
18.11	0.67	186.0	19.3
21.03	0.67	212.0	22.1
23.66	0.67	238.0	24.8
27.06	0.67	266.1	27.7
29.31	0.67	293.1	30.5

Table C.12: Pool boiling data of water on sample 6

Wall superheat $[°C]$	$\mathbf{u_{DT}}$ $[°C]$	Heat flux $[kW/m^2]$	$\mathbf{u_q}$ $[kW/m^2]$
7.99	0.67	36.4	3.8
9.02	0.67	48.9	5.1
12.06	0.66	63.4	6.6
15.05	0.66	79.0	8.2
18.49	0.66	96.7	10.1
21.65	0.66	116.4	12.1
25.01	0.66	137.2	14.3
28.45	0.67	159.0	16.5
31.14	0.67	184.0	19.1
34.30	0.67	207.9	21.6
39.31	0.67	234.9	24.4
44.05	0.67	261.9	27.2

Table C.13: Pool boiling data of water-alumina 0.1% wt nanofluid on sample 6

D
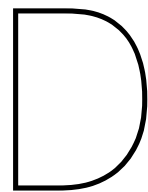
Calibration

The calibration of the thermocouples was performed in a thermostatic water bath (LAUDA ECO RE 415). The calibration curves are shown in Figure D.1, where the first plot refers to the thermocouple used to extrapolate the surface temperature, the second one is the thermocouple placed inside the boiling cell, and the third one is the thermocouple inserted into the the inlet tube of the cold finger. The horizontal and vertical axis indicate the temperature setpoint of the isothermal bath and the temperature reading of the sensor, respectively. Then, linear fitting was applied and the equations of the lines were used as inputs to Arduino to correct for systematic errors in the temperature measurements. Finally, the root-mean-square error in the calibration curves for Thermocouple 1 and 2 was calculated to quantify the systematic uncertainty in the temperature readings after the calibration. Indeed, this is piece of information is needed to assess the overall uncertainty in the data points plotted in the boiling curves and it was found to be as large as $u_s = \pm0.47°C$ (Table D.1).
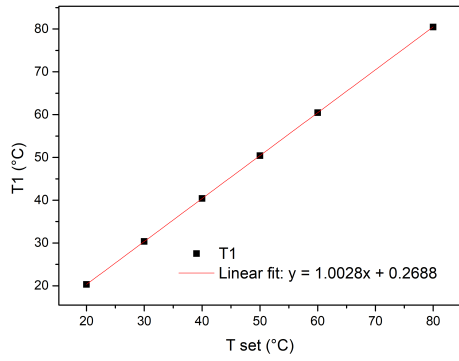
(a) Themocouple 1
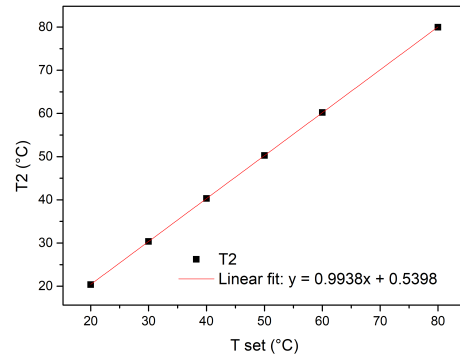
(b) Thermocouple 2
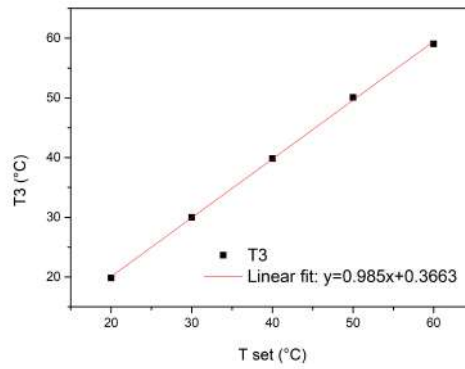
(c) Thermocouple 3

Figure D.1: Calibration curves

T_{set}	T_1	T_2	RMSE 1	RMSE 2
20	20.30	20.37	0.40	0.28
30	30.35	30.36	0.42	0.26
40	40.39	40.30	0.43	0.23
50	50.42	50.27	0.45	0.20
60	60.45	60.22	0.46	0.15
80	80.47	79.98	0.47	0.019

Table D.1: Systematic uncertainty after calibration

E
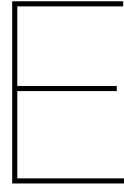
Statistical analysis with RStudio

In order to investigate on the dependency of the HTC on the roughness parameters, regression analysis was performed using the software RStudio.

First, a multi-variable linear model was developed to express the relation between the response variable and explanatory variables (i.e. the HTC and the Ra, R_{ku}, R_{sk}). This model assumes that a linear relation between the response variable (denoted with y) and the predictors (denoted by x_1, x_2, x_3) exists. This may be formulated as follows:

$$y = b_0 + b_1 x_1 + b_2 x_2 + b_3 x_3 + \epsilon \tag{E.1}$$

where $b_0 + b_1 x_1 + b_2 x_2 + b_3 x_3$ is the structural part and ϵ is the error of the model. The error part includes the contributions of all the other factors which may cause a variation in the response variable but are not considered in the model.

The objective of regression analysis is to derive the unknown coefficients in equation E.1 based on the experimental data collected. The values of the response value predicted by the regression equation are called fitted values; the difference between them and the actual values of the dependent variable are defined as residuals. Graphically, they may be interpreted as the vertical distance between each data point in a scatter plot and the regression line given by the model. In order to determine the regression line, the ordinary least squares method is applied, consisting in finding the best fit by minimizing the residual sum of squares, also known as the sum of squared estimate of errors (SSE).
When running a regression analysis with RStudio, the output is summarized in a report which displays numerical values of the coefficients as well as other statistical indicators allowing to assess the accuracy of the model. In particular, the coefficient b_0 is the intercept and b_1, b_2, b_3 are called partial slopes. They provide more insightful information by quantifying how fast the response variable varies because of a unit variation in a predictor. Moreover, for each coefficient the residual standard error s is calculated as follows:

$$s = \sqrt{\frac{SSE}{n-2}} \tag{E.2}$$

where n is the number of data points. Essentially, s indicates how far the actual values of y are from the fitted values given by the model.
Conventionally, the accuracy of a regression model is assessed by means of the coefficient or determination R^2. This is a statistical index defined as the proportion of the variance for the response variable that is predictable by the dependent variables (i.e. to what extent the variance of the predictors is able to explain the variance of the dependent variable):

$$R^2 = \frac{regression\ sum\ of\ squares\ (SSR)}{total\ sum\ of\ squares\ (SST)} = 1 - \frac{SSE}{SST} \tag{E.3}$$

being $SST = SSR + SSE$.

From the definition of R^2 it follows that adding independent variables will always increase the value of R^2, hence an adjusted R^2 is introduced to evaluate the accuracy of different models:

$$R^2_{adjusted} = 1 - \frac{n-1}{n-p-1} \times \frac{SSE}{SST} = 1 - \frac{n-1}{n-p-1}(1 - R^2) \tag{E.4}$$

where p is the number of predictors n the number of observations. Therefore, it should be noted that $R^2_{adjusted}$ is always less or equal to R^2; in particular, $R^2_{adjusted}$ decreases whenever a variable which does not improve the goodness-of-fit is added to the model.

Furthermore, RStudio performs the so-called T test on the model. This is a significance test where two hypotheses are compared: the null hypothesis, stating that there is no relation between a certain independent variable and the response variable, and the alternative hypothesis. The T test yields the t value, defined as the ratio of the coefficient of an independent variable and its standard error:

$$t = \frac{b_i}{s_{b_i}} \tag{E.5}$$

Effectively, the t value is a measure of how many standard deviations a coefficient estimated by linear regression is far away from zero, thus allowing to reject the null hypothesis. Indeed, the larger the coefficient compared to its standard error, the higher the certainty on the fact that it is not zero, thus enabling to conclude that the coefficient is significant.
Then, the p value is derived from the T distribution using the t-statistics. The p value represents the probability that the measured data have occurred under the null hypothesis. Therefore, if the p value is very close to zero, it is unlikely that the null hypothesis is true so it may be inferred that there is a correlation between the response variable and the predictors. Normally, the p value is compared against a significance level ($\alpha = 0.05$): if $p < \alpha$ there is evidence that variations in the dependent variable are due to changes in the predictors, hence they are said to be statistically significant as they are worthwhile to the model.

Figure E.1 shows the detailed report regarding the multi-variable linear model, whose explicit equation is given by:

$$y = 14130 - 1069x_1 - 623x_2 + 3854x_3 \tag{E.6}$$

However, it must be noted that the R^2 is almost zero, thus the $R^2_{adjusted}$ becomes negative, meaning that a linear model fails to explain the relation between the response variable and the predictors. Indeed, the p value (considering the independent variables both individually and jointly) is $\gg 0.05$, leading to the conclusion that the predictors are not statistically significant.

```
Call:
lm(formula = y ~ 1 + x1 + x2 + x3, data = m.data)

Residuals:
        1        2        3        4        5        6
 2558.94  5224.02 -5112.07  2759.55  2097.17   -84.47
        7
-7443.14

Coefficients:
             Estimate Std. Error t value Pr(>|t|)
(Intercept)   14130.0    11744.5   1.203    0.315
x1            -1069.1    14884.0  -0.072    0.947
x2             -623.1     2077.9  -0.300    0.784
x3             3853.7    12593.1   0.306    0.780

Residual standard error: 6516 on 3 degrees of freedom
Multiple R-squared:  0.03058,   Adjusted R-squared:  -0.9388
F-statistic: 0.03154 on 3 and 3 DF,  p-value: 0.991
```

Figure E.1: Summary multi-variable linear model

Being a linear model inadequate, an alternative approach to linear regression is to apply a GAM model (generalized additive model), where the coefficients of the independent variables are replaced with flexible functions, referred to as *splines* or *smooth functions*. GAM models are based on the assumption that the response variable is given by a non-linear combination of the predictors:

$$y = b_0 + s_1 x_1 + s_2 x_2 + s_3 x_3 + \epsilon, \qquad\qquad \text{(E.7)}$$

where s_1, s_2, s_3 denote the splines.

Therefore, the curve representing the model results from the sum of the splines associated with each predictor. Generally, increasing the number of splines would improve the accuracy of the model but it would also increase the wiggliness of the fitting curve. Hence, the optimal number of splines k must be found to prevent overfitting (in this case $k = 3$ for each predictor).

The output of the GAM model (Figure E.2) shows that the $R^2_{adjusted} = 0.91$ and the percentage of deviance explained in the dependent variable is 97%. Moreover, all the p values are < 0.05 meaning that a non-linear combination of the predictors is statistically significant.

However, a GAM model does not give an explicit form of the splines used in the fitting, it only provides indication of the degree of non-linearity of the curve (edf) and of the shape of the splines (Figure E.3). In particular, it must be noted that for the first and the second smooth term $edf = 1$, which is equivalent to a linear relationship, whereas $edf = 2$ for the third predictor. This suggests that the non-linear contribution is due to the third explanatory variable x_3.

This piece of information was used to adjust the linear model, including a quadratic effect of x_3. Therefore, a corrected version of the linear model was obtained:

$$y = -45565 + 42258x_1 + 11349x_2 - 7952x_3 - 27593x_3^2 \qquad\qquad \text{(E.8)}$$

As highlighted in the summary (Figure E.4) the t values and the $R^2_{adjusted}$ have improved appreciably. Indeed, it can be seen that the additional term is the most significant one with a p value of 0.0316 and each predictor adds value to the model as p_{x_1}, p_{x_2}, p_{x_3} are less than 0.05. The fact that the overall p value is 0.1 indicates that, in spite of the independent variables being significant individually, there is not sufficient evidence to conclude that all the coefficients of the predictors would not be equal to zero at the same time. Nonetheless, the goodness of the model is confirmed by the $R^2_{adjusted} = 0.82$.

Moreover, the adjusted model produces smaller residuals than the initial regression model (Figure E.5). The residuals line is almost flat, meaning that the information provided by the predictors is used at its fullest to explain the variability of the response.

```
Formula:
y ~ s(x1, k = 3) + s(x2, k = 3) + s(x3, k = 3)

Parametric coefficients:
            Estimate Std. Error t value Pr(>|t|)
(Intercept)  12933.7      527.5   24.52  0.00159 **
---
Signif. codes:  0 '***' 0.001 '**' 0.01 '*' 0.05 '.' 0.1 ' ' 1

Approximate significance of smooth terms:
         edf Ref.df      F p-value
s(x1) 1.000      1  41.15  0.0235 *
s(x2) 1.000      1  50.34  0.0193 *
s(x3) 1.984      2  31.94  0.0301 *
---
Signif. codes:  0 '***' 0.001 '**' 0.01 '*' 0.05 '.' 0.1 ' ' 1

R-sq.(adj) =  0.911   Deviance explained =    97%
-REML = 30.332  Scale est. = 1.9475e+06  n = 7
```

Figure E.2: Summary of GAM model

(a)

(b)

(c)
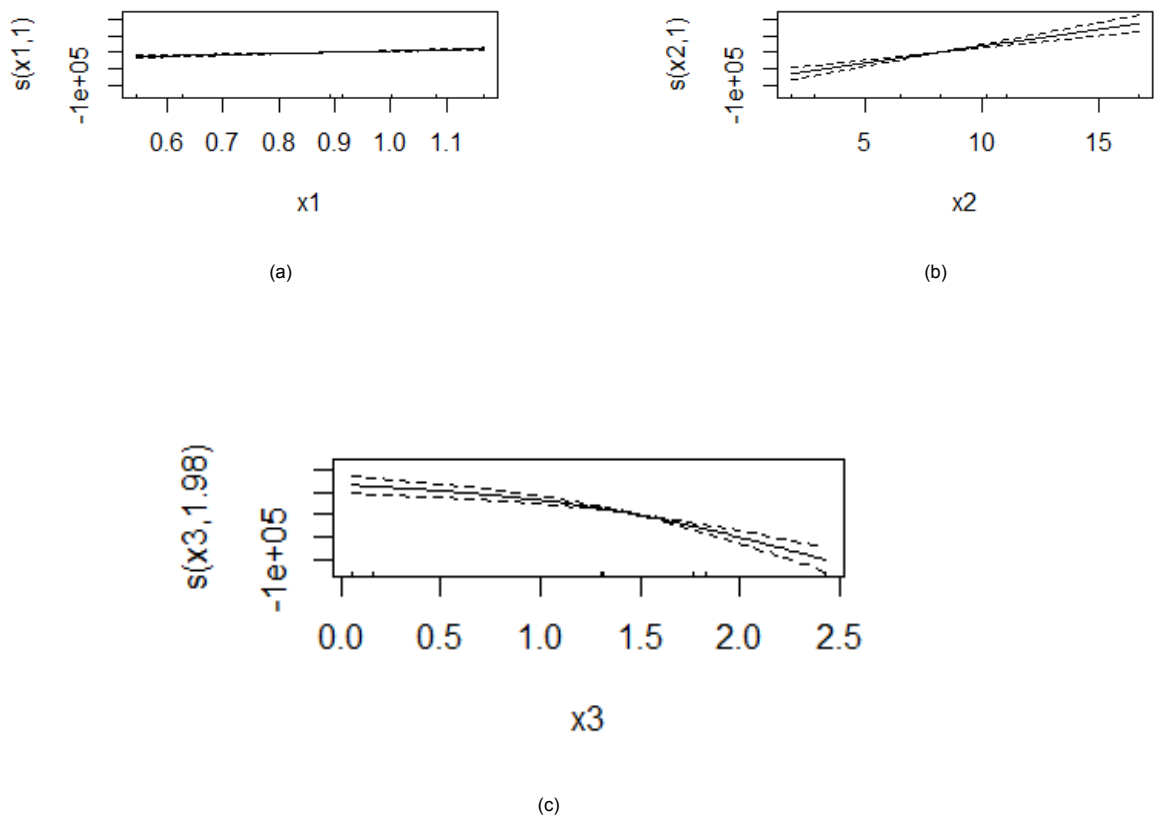
Figure E.3: Shape of the smooth functions in the GAM model

```
Call:
lm(formula = y ~ 1 + x1 + x2 + x3 + I(x3^2), data = m.data)

Residuals:
      1      2       3       4       5      6       7
  673.5 1690.7  -948.6 -1852.5  -229.8  419.2   247.5

Coefficients:
            Estimate Std. Error t value Pr(>|t|)
(Intercept)   -45565      11455  -3.978   0.0578 .
x1             42258       9112   4.638   0.0435 *
x2             11349       2272   4.995   0.0378 *
x3             -7952       4409  -1.803   0.2131
I(x3^2)       -27593       5028  -5.488   0.0316 *
---
Signif. codes:  0 '***' 0.001 '**' 0.01 '*' 0.05 '.' 0.1 ' ' 1

Residual standard error: 1992 on 2 degrees of freedom
Multiple R-squared:  0.9396,     Adjusted R-squared:  0.8189
F-statistic: 7.782 on 4 and 2 DF,  p-value: 0.1171
```

Figure E.4: Summary of corrected multi-variable linear model
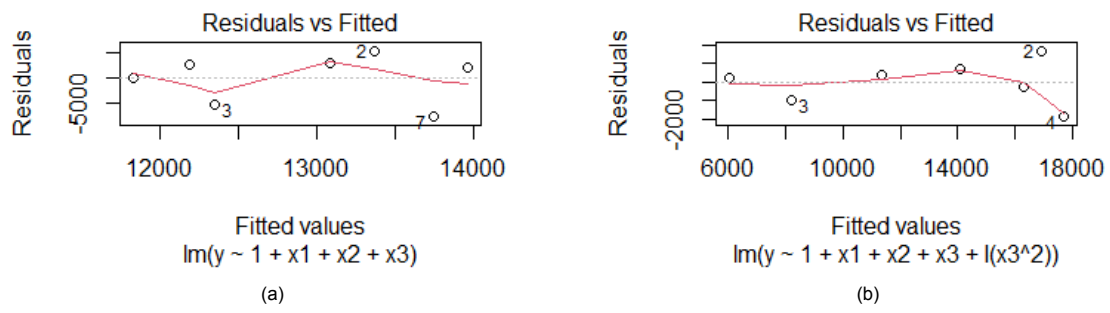
Figure E.5: Comparison between the residuals in the linear model and the corrected version

Bibliography

[1] Ahmed AbdElHady. "EXPERIEMENTAL INVESTIGATION OF POOL BOILING AND BOILING UNDER SUBMERGED IMPINGING JET OF NANOFLUIDS". PhD thesis. 2013.

[2] Mohammad Hossein Ahmadi et al. "A review of thermal conductivity of various nanofluids". In: *Journal of Molecular Liquids* 265 (2018), pp. 181–188.

[3] Amir Akbari et al. "Comparison between Nucleate Pool Boiling Heat Transfer of Graphene Nanoplatelet-and Carbon Nanotube-Based Aqueous Nanofluids". In: *ACS omega* 4.21 (2019), pp. 19183–19192.

[4] Mehdi Bahiraei and Saeed Heshmatian. "Electronics cooling with nanofluids: a critical review". In: *Energy Conversion and Management* 172 (2018), pp. 438–456.

[5] Nanik Bakhru and John H Lienhard. "Boiling from small cylinders". In: *International Journal of Heat and Mass Transfer* 15.11 (1972), pp. 2011–2025.

[6] In Cheol Bang and Soon Heung Chang. "Boiling heat transfer performance and phenomena of Al2O3–water nano-fluids from a plain surface in a pool". In: *International Journal of Heat and Mass Transfer* 48.12 (2005), pp. 2407–2419.

[7] SG Bankoff. "Entrapment of gas in the spreading of a liquid over a rough surface". In: *AIChE journal* 4.1 (1958), pp. 24–26.

[8] W Bauer, M Weber, and S Chanbai. "White Light Interferometry". In: *Encyclopedia of Tribology*. Springer, 2013, pp. 4115–4127.

[9] RJ Benjamin and AR Balakrishnan. "Nucleate pool boiling heat transfer of pure liquids at low to moderate heat fluxes". In: *International Journal of Heat and Mass Transfer* 39.12 (1996), pp. 2495–2504.

[10] RJ Benjamin and AR Balakrishnan. "Nucleation site density in pool boiling of saturated pure liquids: effect of surface microroughness and surface and liquid physical properties". In: *Experimental Thermal and Fluid Science* 15.1 (1997), pp. 32–42.

[11] Bharat Apparao Bhanvase and Divya Barai. *Nanofluids for Heat and Mass Transfer: Fundamentals, Sustainable Manufacturing and Applications*. Academic Press, 2021.

[12] Von DAG Bruggeman. "Berechnung verschiedener physikalischer Konstanten von heterogenen Substanzen. I. Dielektrizitätskonstanten und Leitfähigkeiten der Mischkörper aus isotropen Substanzen". In: *Annalen der physik* 416.7 (1935), pp. 636–664.

[13] Zhen Cao. "Pool boiling on structured surfaces: heat transfer and critical heat flux: experiments and mechanistic modelling". PhD thesis. Lund University, 2019.

[14] Renkun Chen et al. "Nanowires for enhanced boiling heat transfer". In: *Nano letters* 9.2 (2009), pp. 548–553.

[15] S US Choi and Jeffrey A Eastman. *Enhancing thermal conductivity of fluids with nanoparticles*. Tech. rep. Argonne National Lab., IL (United States), 1995.

[16] Robert Cole and WM Rohsenow. "Correlation of bubble departure diameters for boiling of saturated liquids". In: *Chem. Eng. Prog. Symp. Ser*. Vol. 65. 92. 211 213. 1969, pp. 211–213.

[17] John G Collier and John R Thome. *Convective boiling and condensation*. Clarendon Press, 1994.

[18] European Commission. "2030 climate and energy framework". In: (2021 <https://ec.europa.eu/clima/eu-action/climate-strategies-targets/2030-climate-energy-framework$_e ntab − 0 − 0 >$).

[19] Pellegrino Conte et al. "Coherence Length Measurement System Design Description Document ASML/Tao Chen Faculty Advisor: Professor Thomas Brown". In: ().

[20] Sarit K Das, Nandy Putra, and Wilfried Roetzel. "Pool boiling characteristics of nano-fluids". In: *International journal of heat and mass transfer* 46.5 (2003), pp. 851–862.

[21] Daxiang Deng et al. "Pool boiling heat transfer of porous structures with reentrant cavities". In: *International Journal of Heat and Mass Transfer* 99 (2016), pp. 556–568.

[22] VE Denny and AF Mills. "Nonsimilar solutions for laminar film condensation on a vertical surface". In: *International Journal of Heat and Mass Transfer* 12.8 (1969), pp. 965–979.

[23] Navdeep Singh Dhillon, Jacopo Buongiorno, and Kripa K Varanasi. "Critical heat flux maxima during boiling crisis on textured surfaces". In: *Nature communications* 6.1 (2015), pp. 1–12.

[24] TN Dinh, JP Thu, and TG Theofanous. "Burnout in high heat flux boiling: the hydrodynamic and physico-chemical factors". In: *42nd AIAA Aerospace Sciences Meeting and Exhibit*. 2004.

[25] Lian Duan et al. "Pool boiling heat transfer on silicon chips with non-uniform micro-pillars". In: *International Journal of Heat and Mass Transfer* 151 (2020), p. 119456.

[26] "Dynamic Light Scattering : An Introduction in 30 Minutes". In: 2014.

[27] Jeffrey A Eastman et al. "Thermal transport in nanofluids". In: *Annu. Rev. Mater. Res.* 34 (2004), pp. 219–246.

[28] EU. "Advanced Data and power Electrical NEtwork Architectures and Systems". In: (2020 <https://www.adenea-project.eu/>).

[29] EU. "BRAINE project". In: (2019 <https://www.kdt-ju.europa.eu/projects/braine>).

[30] Richard S Figliola and Donald E Beasley. *Theory and design for mechanical measurements*. John Wiley & Sons, 2020.

[31] Richard Francis Gaertner. "Photographic study of nucleate pool boiling on a horizontal surface". In: (1965).

[32] H Ganapathy and V Sajith. "Semi-analytical model for pool boiling of nanofluids". In: *International Journal of Heat and Mass Transfer* 57.1 (2013), pp. 32–47.

[33] Dennis F Gardner, Julian S Evans, and Ivan I Smalyukh. "Towards reconfigurable optical meta-materials: colloidal nanoparticle self-assembly and self-alignment in liquid crystals". In: *Molecular Crystals and Liquid Crystals* 545.1 (2011), pp. 3–1227.

[34] Craig Gerardi et al. "Study of bubble growth in water pool boiling through synchronized, infrared thermometry and high-speed video". In: *International Journal of Heat and Mass Transfer* 53.19-20 (2010), pp. 4185–4192.

[35] Craig Douglas Gerardi. "Investigation of the pool boiling heat transfer enhancement of nano-engineered fluids by means of high-speed infrared thermography". PhD thesis. Massachusetts Institute of Technology, 2009.

[36] S Mostafa Ghiaasiaan. *Two-phase flow, boiling, and condensation: in conventional and miniature systems*. Cambridge University Press, 2007.

[37] Dieter Gorenflo and David Kenning. *Pool boiling in VDI Heat Atlas*. Vol. H2. Springer Berlin Heidelberg, 2009, pp. 757–792.

[38] Dieter Gorenflo, V Knabe, and Volker Bieling. "Bubble Density on Surfaces with Nucleate Boiling-Its Influence on Heat Transfer and Burnout Heat Flux at Elevated Saturation Pressures". In: *International Heat Transfer Conference Digital Library*. Begel House Inc. 1986.

[39] Peter Griffith. "Bubble growth rates in boiling". In: *Transactions of the American Society of Mechanical Engineers* 80.3 (1958), pp. 721–726.

[40] SV Gupta. "Capillary action in narrow and wide tubes—A unified approach". In: *Metrologia* 41.6 (2004), p. 361.

[41] M Hamda and MS Hamed. "Bubble dynamics in pool boiling of nanofluids". In: (2016).

[42] R L☐ Hamilton and OK Crosser. "Thermal conductivity of heterogeneous two-component systems". In: *Industrial & Engineering chemistry fundamentals* 1.3 (1962), pp. 187–191.

[43] Y Haramura and YJIJoH Katto. "A new hydrodynamic model of critical heat flux, applicable widely to both pool and forced convection boiling on submerged bodies in saturated liquids". In: *International Journal of Heat and Mass Transfer* 26.3 (1983), pp. 389–399.

[44] G Harish, V Emlin, and V Sajith. "Effect of surface particle interactions during pool boiling of nanofluids". In: *International Journal of Thermal Sciences* 50.12 (2011), pp. 2318–2327.

[45] AP Hatton and IS Hall. "Photographic study of boiling on prepared surfaces". In: *International Heat Transfer Conference Digital Library*. Begel House Inc. 1966.

[46] Yih-Yun Hsu and Robert W Graham. *An analytical and experimental study of the thermal boundary layer and ebullition cycle in nucleate boiling*. Vol. 594. National Aeronautics and Space Administration, 1961.

[47] Suhaib Umer Ilyas, Rajashekhar Pendyala, and Narahari Marneni. "Stability of nanofluids". In: *Engineering applications of nanotechnology*. Springer, 2017, pp. 1–31.

[48] HJ Ivey. "Relationships between bubble frequency, departure diameter and rise velocity in nucleate boiling". In: *International Journal of Heat and Mass Transfer* 10.8 (1967), pp. 1023–1040.

[49] Arvind Jaikumar and Satish G Kandlikar. "Enhanced pool boiling heat transfer mechanisms for selectively sintered open microchannels". In: *International Journal of Heat and Mass Transfer* 88 (2015), pp. 652–661.

[50] Seok Pil Jang and Stephen US Choi. "Role of Brownian motion in the enhanced thermal conductivity of nanofluids". In: *Applied physics letters* 84.21 (2004), pp. 4316–4318.

[51] Mohammed Saad Kamel and Ferenc Lezsovits. "Enhancement of pool boiling heat transfer performance using dilute cerium oxide/water nanofluid: An experimental investigation". In: *International Communications in Heat and Mass Transfer* 114 (2020), p. 104587.

[52] Nishikawa Kaneyasu et al. "Effect of surface configuration on nucleate boiling heat transfer". In: *International Journal of Heat and Mass Transfer* 27.9 (1984), pp. 1559–1571.

[53] Mehrdad Karimzadehkhouei et al. "The effect of nanoparticle type and nanoparticle mass fraction on heat transfer enhancement in pool boiling". In: *International Journal of Heat and Mass Transfer* 109 (2017), pp. 157–166.

[54] Phillbot Keblinski et al. "Mechanisms of heat flow in suspensions of nano-sized particles (nanofluids)". In: *International journal of heat and mass transfer* 45.4 (2002), pp. 855–863.

[55] Ibrahim Khan, Khalid Saeed, and Idrees Khan. "Nanoparticles: Properties, applications and toxicities". In: *Arabian journal of chemistry* 12.7 (2019), pp. 908–931.

[56] Dong Eok Kim et al. "Pure steam condensation model with laminar film in a vertical tube". In: *International journal of multiphase flow* 37.8 (2011), pp. 941–946.

[57] Dong Eok Kim et al. "Review of boiling heat transfer enhancement on micro/nanostructured surfaces". In: *Experimental Thermal and Fluid Science* 66 (2015), pp. 173–196.

[58] Hyung Dae Kim and Moo Hwan Kim. "Effect of nanoparticle deposition on capillary wicking that influences the critical heat flux in nanofluids". In: *Applied physics letters* 91.1 (2007), p. 014104.

[59] Hyungdae Kim and Dong Eok Kim. "Effects of surface wettability on pool boiling process: Dynamic and thermal behaviors of dry spots and relevant critical heat flux triggering mechanism". In: *International Journal of Heat and Mass Transfer* 180 (2021), p. 121762.

[60] Jinsub Kim et al. "Effect of surface roughness on pool boiling heat transfer at a heated surface having moderate wettability". In: *International Journal of Heat and Mass Transfer* 101 (2016), pp. 992–1002.

[61] Jungho Kim and Rishi Raj. "Gravity and Heater Size Effects on Pool Boiling Heat Transfer". In: 2014.

[62] Seol Ha Kim et al. "Boiling heat transfer and critical heat flux evaluation of the pool boiling on micro structured surface". In: *International Journal of Heat and Mass Transfer* 91 (2015), pp. 1140–1147.

[63] Seol Ha Kim et al. "The role of surface energy in heterogeneous bubble growth on ideal surface". In: *International Journal of Heat and Mass Transfer* 108 (2017), pp. 1901–1909.

[64]   Sung Joong Kim et al. "Surface wettability change during pool boiling of nanofluids and its ef-
        fect on critical heat flux". In: *International Journal of Heat and Mass Transfer* 50.19-20 (2007),
        pp. 4105–4116.

[65]   Stephen J Kline. "Describing uncertainty in single sample experiments". In: *Mech. Engineering*
        75 (1953), pp. 3–8.

[66]   Nikolay Ivanov Kolev and NI Kolev. *Multiphase flow dynamics*. Vol. 1003. Springer, 2005.

[67]   Francis A Kulacki et al. *Handbook of thermal science and engineering*. Springer, 2018.

[68]   Ganesan Udaya Kumar et al. "Modified surfaces using seamless graphene/carbon nanotubes
        based nanostructures for enhancing pool boiling heat transfer". In: *Experimental thermal and
        fluid science* 96 (2018), pp. 493–506.

[69]   Samson Semenovich Kutateladze. *Heat transfer in condensation and boiling*. Vol. 3770. US
        Atomic Energy Commission, Technical Information Service, 1959.

[70]   Sang M Kwark et al. "Pool boiling characteristics of low concentration nanofluids". In: *Interna-
        tional Journal of Heat and Mass Transfer* 53.5-6 (2010), pp. 972–981.

[71]   Chen Li and GP Peterson. "Evaporation/boiling in thin capillary wicks (II)—effects of volumetric
        porosity and mesh size". In: (2006).

[72]   Xiangdong Li, Sherman Chi Pok Cheung, and Jiyuan Tu. "Nucleate boiling of dilute nanofluids–
        Mechanism exploring and modeling". In: *International journal of thermal sciences* 84 (2014),
        pp. 323–334.

[73]   Gangtao Liang and Issam Mudawar. "Pool boiling critical heat flux (CHF)–Part 1: Review of
        mechanisms, models, and correlations". In: *International Journal of Heat and Mass Transfer*
        117 (2018), pp. 1352–1367.

[74]   Shin-Pin Liaw and VK Dhir. "Void fraction measurements during saturated pool boiling of water
        on partially wetted vertical surfaces". In: (1989).

[75]   IV Lienhard and H John. *A heat transfer textbook*. phlogiston press, 2005.

[76]   JH Lienhard and VK Dhir. "Hydrodynamic prediction of peak pool-boiling heat fluxes from finite
        bodies". In: (1973).

[77]   Andreas Liese and Lutz Hilterhaus. "Evaluation of immobilized enzymes for industrial applica-
        tions". In: *Chemical Society Reviews* 42.15 (2013), pp. 6236–6249.

[78]   Zhen-hua Liu and Liang Liao. "Sorption and agglutination phenomenon of nanofluids on a plain
        heating surface during pool boiling". In: *International Journal of Heat and Mass Transfer* 51.9-10
        (2008), pp. 2593–2602.

[79]   Alexis Loiseau et al. "Silver-based plasmonic nanoparticles for and their use in biosensing". In:
        Biosensors 9.2 (2019), p. 78.

[80]   Mustafa Lotya et al. "Measuring the lateral size of liquid-exfoliated nanosheets with dynamic
        light scattering". In: *Nanotechnology* 24.26 (2013), p. 265703.

[81]   James Clerk Maxwell. *A treatise on electricity and magnetism*. Vol. 1. Clarendon press, 1873.

[82]   Williams H McAdams. *Heat transmission*. Tech. rep. 1954.

[83]   BB Mikic, WM Rohsenow, and P Griffith. "On bubble growth rates". In: *International Journal of
        Heat and Mass Transfer* 13.4 (1970), pp. 657–666.

[84]   Denitsa Milanova and Ranganathan Kumar. "Heat transfer behavior of silica nanoparticles in
        pool boiling experiment". In: *Journal of Heat Transfer* 130.4 (2008).

[85]   Anthony F Mills. *Heat transfer*. CRC Press, 1992.

[86]   Shi Ming-Heng, Ji Ma, and Wang Bu-Xuan. "Analysis on hysteresis in nucleate pool boiling heat
        transfer". In: *International journal of heat and mass transfer* 36.18 (1993), pp. 4461–4466.

[87]   Robert J Moffat. "Describing the uncertainties in experimental results". In: *Experimental thermal
        and fluid science* 1.1 (1988), pp. 3–17.

[88]   Ernest J Moniz. *Nanotechnology for the energy challenge*. John Wiley & Sons, 2010.

[89]   Youngsuk Nam et al. "Experimental and numerical study of single bubble dynamics on a hydrophobic surface". In: *Journal of Heat Transfer* 131.12 (2009).

[90]   G Prakash Narayan, KB Anoop, and Sarit K Das. "Mechanism of enhancement/deterioration of boiling heat transfer using stable nanoparticle suspensions over vertical tubes". In: *Journal of Applied Physics* 102.7 (2007), p. 074317.

[91]   Siavouche Nemat-Nasser and Muneo Hori. *Micromechanics: overall properties of heterogeneous materials*. Elsevier, 2013.

[92]   Robert Pastuszko. "Pool boiling heat transfer on micro-fins with wire mesh–Experiments and heat flux prediction". In: *International Journal of Thermal Sciences* 125 (2018), pp. 197–209.

[93]   Fred N Peebles. "Studies on the motion of gas bubbles in liquid". In: *Chem. Eng. Prog.* 49.2 (1953), pp. 88–97.

[94]   Sanja Petrovic, Tony Robinson, and Ross L Judd. "Marangoni heat transfer in subcooled nucleate pool boiling". In: *International Journal of Heat and Mass Transfer* 47.23 (2004), pp. 5115–5128.

[95]   Hai Trieu Phan et al. "Surface coating with nanofluids: the effects on pool boiling heat transfer". In: *Nanoscale and Microscale Thermophysical Engineering* 14.4 (2010), pp. 229–244.

[96]   IL Pioro. "Experimental evaluation of constants for the Rohsenow pool boiling correlation". In: *International Journal of Heat and Mass Transfer* 42.11 (1999), pp. 2003–2013.

[97]   IL Pioro, W Rohsenow, and SS Doerffer. "Nucleate pool-boiling heat transfer. I: review of parametric effects of boiling surface". In: *International Journal of Heat and Mass Transfer* 47.23 (2004), pp. 5033–5044.

[98]   M So Plesset and So A Zwick. "The growth of vapor bubbles in superheated liquids". In: *Journal of applied physics* 25.4 (1954), pp. 493–500.

[99]   František Pochylỳ et al. "Study of the adhesive coefficient effect on the hydraulic losses and cavitation". In: *International Journal of Fluid Machinery and Systems* 3.4 (2010), pp. 386–395.

[100]   Richard P Pohanish and Christopher J McCauley. *Machinery's Handbook Pocket Companion*. Industrial Press Inc., 2000.

[101]   Mieczyslaw E Poniewski. "Peculiarities of boiling heat transfer on capillary-porous coverings". In: *International journal of thermal sciences* 43.5 (2004), pp. 431–442.

[102]   Russell P Rioux, Eric C Nolan, and Calvin H Li. "A systematic study of pool boiling heat transfer on structured porous surfaces: From nanoscale through microscale to macroscale". In: *AIP Advances* 4.11 (2014), p. 117133.

[103]   Warren M Rohsenow. *A method of correlating heat transfer data for surface boiling of liquids*. Tech. rep. Cambridge, Mass.: MIT Division of Industrial Cooporation,[1951], 1951.

[104]   Warren M Rohsenow and Peter Griffith. *Correlation of maximum heat flux data for boiling of saturated liquids*. Tech. rep. Cambridge, Mass.: Massachusetts Institute of Technology, Division of …, 1955.

[105]   Warren Max Rohsenow. "Heat transfer and temperature distribution in laminar-film condensation". In: *Transactions of the American Society of Mechanical Engineers* 78.8 (1956), pp. 1645–1647.

[106]   Pratap Sadasivan et al. "Possible mechanisms of macrolayer formation". In: *International communications in heat and mass transfer* 19.6 (1992), pp. 801–815.

[107]   Sujoy Kumar Saha, Gian Piero Celata, and Satish G Kandlikar. "Thermofluid dynamics of boiling in microchannels". In: *Advances in heat transfer*. Vol. 43. Elsevier, 2011, pp. 77–226.

[108]   MM Sarafraz, T Kiani, and F Hormozi. "Critical heat flux and pool boiling heat transfer analysis of synthesized zirconia aqueous nano-fluids". In: *International Communications in Heat and Mass Transfer* 70 (2016), pp. 75–83.

[109]   G Sateesh, Sarit K Das, and Ar R Balakrishnan. "Analysis of pool boiling heat transfer: effect of bubbles sliding on the heating surface". In: *International Journal of Heat and Mass Transfer* 48.8 (2005), pp. 1543–1553.

[110]   Gihun Son, Vijay K Dhir, and N Ramanujapu. "Dynamics and heat transfer associated with a single bubble during nucleate boiling on a horizontal surface". In: (1999).

[111]   Youngsup Song et al. "Three-Tier Hierarchical Structures for Extreme Pool Boiling Heat Transfer Performance". In: *Advanced Materials* (2022), p. 2200899.

[112]   James M Strack. "A New pool boiling facility for the study of nanofluids". PhD thesis. 2013.

[113]   XZ Sun et al. "Enhanced pool boiling on microstructured surfaces with spatially-controlled mixed wettability". In: *International Journal of Heat and Mass Transfer* 183 (2022), p. 122164.

[114]   TG Theofanous et al. "The boiling crisis phenomenon: Part II: dryout dynamics and burnout". In: *Experimental Thermal and Fluid Science* 26.6-7 (2002), pp. 793–810.

[115]   Theo G Theofanous and True-Nam Dinh. "High heat flux boiling and burnout as microphysical phenomena: mounting evidence and opportunities". In: *Multiphase Science and Technology* 18.3 (2006).

[116]   Long Sun Tong. *Boiling heat transfer and two-phase flow*. Routledge, 2018.

[117]   Saeid Vafaei and Theodorian Borca-Tasciuc. "Role of nanoparticles on nanofluid boiling phenomenon: Nanoparticle deposition". In: *Chemical Engineering Research and Design* 92.5 (2014), pp. 842–856.

[118]   S Vallar et al. "Oxide slurries stability and powders dispersion: optimization with zeta potential and rheological measurements". In: *Journal of the European Ceramic Society* 19.6-7 (1999), pp. 1017–1021.

[119]   HJ Van Ouwerkerk. "Burnout in pool boiling the stability of boiling mechanisms". In: *International Journal of Heat and Mass Transfer* 15.1 (1972), pp. 25–34.

[120]   SJD Van Stralen et al. "Bubble growth rates in pure and binary systems: combined effect of relaxation and evaporation microlayers". In: *International Journal of Heat and Mass Transfer* 18.3 (1975), pp. 453–467.

[121]   Peter Vassallo, Ranganathan Kumar, and Stephen D'Amico. "Pool boiling heat transfer experiments in silica–water nano-fluids". In: *International journal of heat and mass transfer* 47.2 (2004), pp. 407–411.

[122]   M Venkatesan, CS Hirtzel, and Raj Rajagopalan. "The effect of colloidal forces on the self-diffusion coefficients in strongly interacting dispersions". In: *The Journal of chemical physics* 82.12 (1985), pp. 5685–5695.

[123]   CH Wang and VK Dhir. "Effect of surface wettability on active nucleation site density during pool boiling of water on a vertical surface". In: (1993).

[124]   JJ Wang et al. "Heat conduction mechanisms in nanofluids and suspensions". In: *Nano Today* 7.2 (2012), pp. 124–136.

[125]   Xinwei Wang, Xianfan Xu, and Stephen US Choi. "Thermal conductivity of nanoparticle-fluid mixture". In: *Journal of thermophysics and heat transfer* 13.4 (1999), pp. 474–480.

[126]   Dongsheng Wen. "Influence of nanoparticles on boiling heat transfer". In: *Applied thermal engineering* 41 (2012), pp. 2–9.

[127]   Dongsheng Wen et al. "Boiling heat transfer of nanofluids: the effect of heating surface modification". In: *International journal of thermal sciences* 50.4 (2011), pp. 480–485.

[128]   Dongsheng Wen et al. "Review of nanofluids for heat transfer applications". In: *Particuology* 7.2 (2009), pp. 141–150.

[129]   Xue-Fei Yang and Zhen-Hua Liu. "Pool boiling heat transfer of functionalized nanofluid under sub-atmospheric pressures". In: *International Journal of Thermal Sciences* 50.12 (2011), pp. 2402–2412.

[130]   SM You, JH Kim, and KH Kim. "Effect of nanoparticles on critical heat flux of water in pool boiling heat transfer". In: *Applied physics letters* 83.16 (2003), pp. 3374–3376.

[131]   W Yu and SUS Choi. "The role of interfacial layers in the enhanced thermal conductivity of nanofluids: a renovated Maxwell model". In: *Journal of nanoparticle research* 5.1 (2003), pp. 167–171.

[132]   Zhongchao Zhao et al. "Visualization-based nucleate pool boiling heat transfer enhancement on different sizes of square micropillar array surfaces". In: *Experimental Thermal and Fluid Science* 119 (2020), p. 110212.

[133]   Novak Zuber. *Hydrodynamic aspects of boiling heat transfer (thesis)*. 4439. United States Atomic Energy Commission, Technical Information Service, 1959.